Title

Switching Dynamics of Thin Film Ferroelectric Devices- A Massively Parallel Phase Field Study

Author

Ashraf, Khalid

Publication Date

2013

Switching Dynamics of Thin Film Ferroelectric Devices - A Massively Parallel Phase Field Study

by

Md. Khalid Ashraf

A dissertation submitted in partial satisfaction of the
requirements for the degree of
Doctor of Philosophy

in

Engineering - Electrical Engineering and Computer Sciences

in the

Graduate Division

of the

University of California, Berkeley

Committee in charge:

Professor Sayeef Salahuddin, Chair
Professor Jeffrey Bokor
Professor Mark Asta

Fall 2013

Switching Dynamics of Thin Film Ferroelectric Devices - A Massively Parallel Phase Field Study

Abstract

Switching Dynamics of Thin Film Ferroelectric Devices - A Massively Parallel Phase Field Study

by

Md. Khalid Ashraf

Doctor of Philosophy in Engineering - Electrical Engineering and Computer Sciences

University of California, Berkeley

Professor Sayeef Salahuddin, Chair

In this thesis, we investigate the switching dynamics in thin film ferroelectrics. Ferroelectric materials are of inherent interest for low power and multi-functional devices. However, possible device applications of these materials have been limited due to the poorly understood electromagnetic and mechanical response at the nanoscale in arbitrary device structures. The difficulty in understanding switching dynamics mainly arises from the presence of features at multiple length scales and the nonlinearity associated with the strongly coupled states. For example, in a ferroelectric material, the domain walls are of nm size whereas the domain pattern forms at micron scale. The switching is determined by coupled chemical, electrostatic, mechanical and thermal interactions. Thus computational understanding of switching dynamics in thin film ferroelectrics and a direct comparison with experiment poses a significant numerical challenge. We have developed a phase field model that describes the physics of polarization dynamics at the microscopic scale. A number of efficient numerical methods have been applied for achieving massive parallelization of all the calculation steps. Conformally mapped elements, node wise assembly and prevention of dynamic loading minimized the communication between processors and increased the parallelization efficiency. With these improvements, we have reached the experimental scale - a significant step forward compared to the state of the art thin film ferroelectric switching dynamics models. Using this model, we elucidated the switching dynamics on multiple surfaces of the multiferroic material BFO. We also calculated the switching energy of scaled BFO islands. Finally, we studied the interaction of domain wall propagation with misfit dislocations in the thin film. We believe that the model will be useful in understanding the switching dynamics in many different experimental setups incorporating thin film ferroelectrics.

To my family for their unconditional love and support

Contents

List of Figures

List of Tables

Acknowledgments

I would like to thank my advisor Professor Sayeef Salahuddin for providing the opportunity to work in his group. Working with him was always a great learning experience. I would like to thank Professors Jeffrey Bokor, Ramamoorthy Ramesh and Mark Asta for kindly accepting my request to be on my qualifying examination committee. Professors Jeffrey Bokor and Mark Asta have been very patient to read through my thesis and providing valuable advice.

I would like to thank Professor Ramesh for the collaboration on switching in BFO thin films. Throughout this collaboration, I have closely worked with Dr. Morgan Trassin, Dr. John Heron and Dr. Martin Gajek. Towards the later part of this project, I also collaborated with Prof. Mitra Taheri's group at Drexel university. Thanks to Prof. Taheri and her students, Chris and Mike for the thought provoking discussions on domain dynamics.

Due to the interdisciplinary nature of the work, I had the opportunity to interact with a number of researchers outside the EE division. Professor James Demmel provided many useful advice on parallel computation and suggested me to use the numerical library PETSC, when I was starting to develop this model. I have received many useful suggestions from Professor Shaofan Li and his graduate student Hiroyuki Minaki during the early stages of element stiffness calculation. I learnt the wonderful subject of statistical mechanics from the classes offered by Professors Dung-Hai Lee and Joel Moore. These classes were always entertaining and provided materials for many interesting discussions with them.

In the LEED group, I had the fortune of interacting with many talented researchers. The postdoctoral scholars Dr. Youngki Yoon, Dr. Long You, Dr. Asis Sarker, Dr. Weiwei Gao, Dr. Mohammad Esmaeilii and the graduate students Kartik Ganapathi, Asif Islam Khan, Chun Wing Yeung, Debanjan Bhowmik, Samuel Smith, Dominic Labanowski, Varun Mishra have all helped me with research or otherwise. Many graduate students in the device group and at 550 Cory have provided many useful pointers and have been good friends throughout my graduate studies. I would like to thank Nattapol Damrongplasit, Rungrot Kitsomboonloha, Philip Chen, Tim Chen, Byron Ho, Sung Hwan Kim, Eung Seok Park, Nuo Xu, Wook Hyun Kwon, Sapan Agarwal, Brian Lambson, David Carlton, Cheuk Chi Lo, Rehan Kapadia, Toshitake Takahashi, Suchit Bhattarai, Claire Baek, Zhaowi Kang, Aamod Shankar and many more.

I have had the great fortune of knowing many people who have enriched me as a person. My teachers at Barisal Zilla School, Dhaka College, BUET and UCR have all laid down the stepping stones for me reaching, where I am today. Many friends at these places and at Berkeley have given me a full filling experience of life. All my relatives have been an extended family for me. There is no way I can properly express my gratitude towards all these wonderful people.

I have been very fortunate to have an elder brother who takes care of everything so that I don't get to face the difficulties of real life. My sister-in-law and niece are the recent addition to this group of people. Above all, I would like to thank my parents for the love, support and sacrifices they have made for me all these years. All my efforts seems worthy if it makes them happy.

Chapter 1

Introduction

1.1 Motivation

Transistors are the building blocks of the information age. In the last couple of decades, the processing power of the computers have increased enormously thanks to the scaling of the devices following the Moore's law. As transistors have become smaller, more and more of them are crammed into the same area making the processors more capable of performing complex tasks.

In recent years, the trend in computing has taken a major shift with the rise of mobile electronics. It is very likely that in the near future, most of the computing will be performed in the cloud and we will be surrounded by a swarm of sensors that will communicate with the cloud.

[J. Rabaey, ASPDAC'08]

Figure 1.1: Intranet of things. The swarm of sensors connected to a local computing device which in turn is connected to the cloud. Figure courtesy of Prof. Jan Rabaey

These trends necessitates two major capabilities from information processing devices. On the cloud side, we want fast and high capacity storage devices that can store and process huge amount of sensor data very quickly. On the client side, we want low power devices that are suitable for mobile devices. These diverse requirements could be achieved by implementing devices that use electron's spin rather than its charge.

Magnetic devices

Spintronic devices are one of the potential alternatives for charge based CMOS devices. Spin is a significantly low energy state variable compared to charge. Being able to generate, inject, control and manipulate spin in nanoscale device structures is thus of significant scientific and technological interest. Here, we show examples of two of the representative device structures that utilize electron's spin to change the resistivity of the device. These devices are used as the read heads in storage devices.

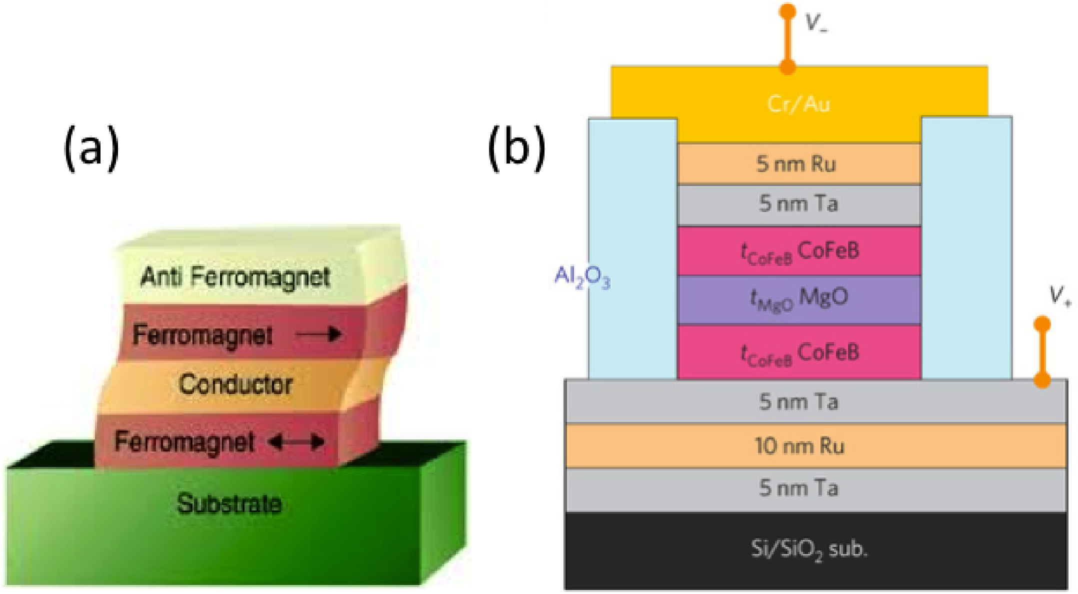

Figure 1.2: (a) Spin valve. b) Magnetic tunnel junction.

Spintronic devices are being developed in the industry as a contender for non volatile memory operation. For example, in late 2012, Everspin introduced the 64 MB DDR3 MRAM chip. Example of an MRAM cell and chip are shown in the figure below. MRAM provides the speed of RAM with the non-volatility of flash devices. Although, this does not have the density of flash yet, but aggressive research is being performed to scale the feature sizes down to around 20 nm. These devices are strong contender as DRAM replacement or alternative mass storage technology.

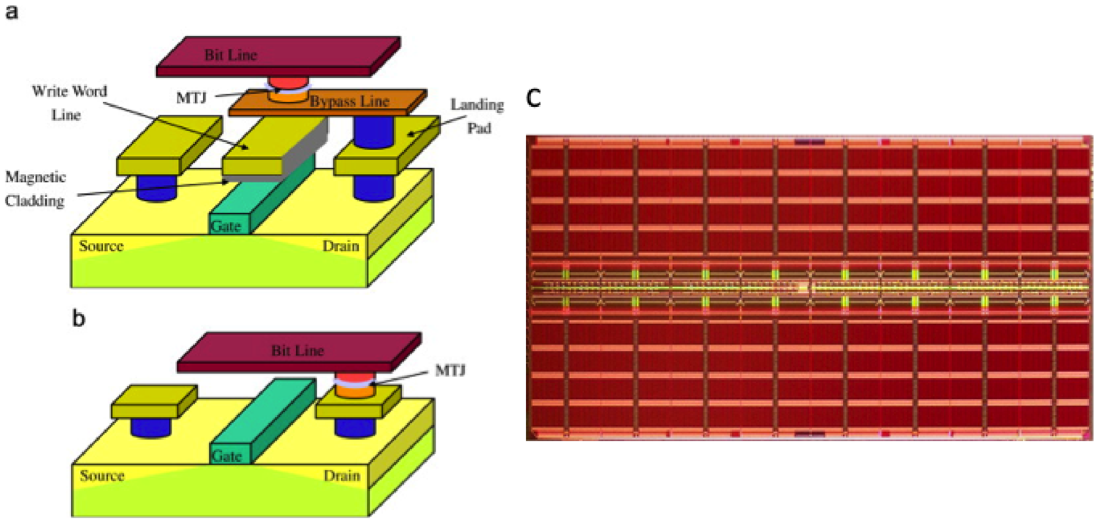

Figure 1.3: (a) MRAM cell (b) Everspin's ST-MRAM chip.

Electric field control of magnetism

Although spintronic devices are inherently low power, their power benefit is not realized due to the high power required to generate the magnetic field for Oersted switching. This problem can be minimized if an electric field induced magnetic switching can be achieved. There are a number of proposed methods for electrical control of magnetism. A detailed account of different paths of electric field control of magnetism can be found in Ref. [18]. We provide a brief introduction of these methods here.

1. Exchange coupling driven:

2. Composite multi-ferroics: Composite multi-ferroics are combinations of ferroelectric, ferro-elastic and/or ferromagnetic materials. Since these materials are lattice coupled in a single system, they could be used to control one order parameter through another [35].

3. Orbital coupling: The orbitals of an AFM could reconstruct and give rise to FM properties in the AFM at the interface of AFM and FM. A prototypical example was found in BFO-LSMO system.

4. Change of carrier concentration: In III-V magnetic semiconductors, the magnetism can be controlled by changing the carrier concentration. This mechanism has been demonstrated in InMnAs, GaMnAs, GeMn etc [48].

5. Surface magneto-crystalline anisotropy: In thin film ferromagnets, the bulk magneto-crystalline anisotropy favors the magnetic moment to be in-plane whereas the surface magneto-crystalline anisotropy drives the magnetic moment to go out of plane. Surface magnetic moment can be controlled by supplying or depleting carriers from the surface, thus magnetism can be controlled by the applied electric field [40]. These types of switching have been shown in magnetic tunnel junctions.

Electric field control of magnetism using Bismuth Ferrite

The target of electric field control of magnetism is to get rid of the conventional inductive switching method and Joule heating incurred in inductive switching. Also electric field based switching is compatible with CMOS circuitry and if achieved, has the potential of tighter control of magnetic bits with low form factor. One approach of electric field control of magnetism that we study is using the multi-ferroic material bismuth ferrite (BFO). BFO is the only known room temperature multi-ferroic material. It is both ferroelectric and anti-ferromagnetic. BFO's Curie temperature is 1103 K and the Neel temperature is 643 K. These order parameters exist and are coupled at room temperature. The figure below shows the unit cell of BFO. There are eight possible directions for the polarization. The weak ferromagnetism induced in BFO is coupled to its polarization directions. Switching of polarization within BFO is expected to switch the magnetization also.

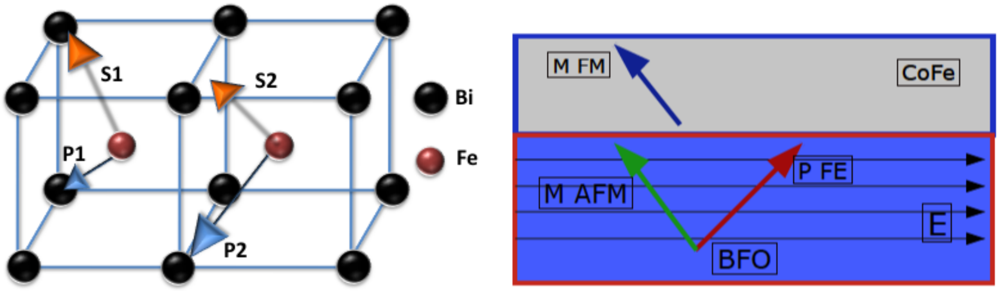

Figure 1.4: (a) The unit cell of BFO containing both polarization, P and week ferromagnetism S. (b) The anti-ferromagnetic BFO can be used to switch a ferromagnet exchange coupled with BFO.

However, BFO is an anti-ferromagnet. In order to get a ferromagnetic switching, the exchange coupling physics is used. A ferromagnet, CoFeB is put on the anti-ferromagnetic BFO. With the application of electric field, the polarization switches. With the polarization, the anti-ferromagnetic order parameter switches. Since, the ferromagnet is exchange coupled with the anti-ferromagnet, it is expected that the ferromagnet will also switch with the application of electric field. Such an experiment was reported in 2008 as shown in the figure below. A horizontal electric field was applied using two buried electrodes in BFO. A magnetic nano dot was placed on the BFO surface. PEEM measurement show that the magnet switches after application of the first electric pulse. It comes back to its previous state after application of the second electric pulse. However, there still remained ambiguity about the actual direction of the magnet after the application of the voltage pulses. Also, no electrical test were performed. Hence, the magnetization dynamics in this system remains to be understood.

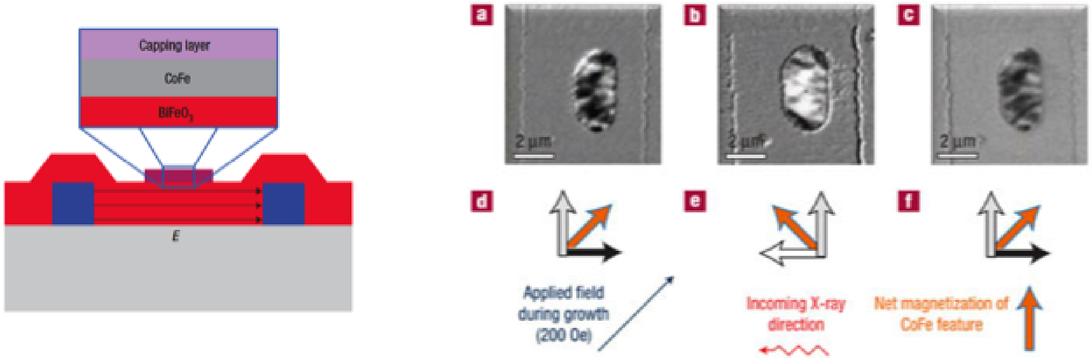

Figure 1.5: Device structure and PEEM image of magnetization reported in Y. H. Chu et al., Nat. Mater, v7, p478 (2008).

In BFO, it has been experimentally observed that there is a one to one correspondence between the ferroelectric and the ferromagnetic orders as shown by the figure below. Since, ferroelectricity is a much higher energy variable compared to magnetism, it turns out that the dynamics of the antiferromagnetic order is completely determined by the ferroelectric dynamics. However, domain switching in thin film ferroelectric with arbitrary electrical and mechanical boundary conditions is a nontrivial process. There remains many unknowns in the domain switching in terms of its physical mechanism and rational device design. Hence, we concentrated on developing a generic simulator that can simulate the switching process in a realistic geometry and elucidate the underlying switching process.

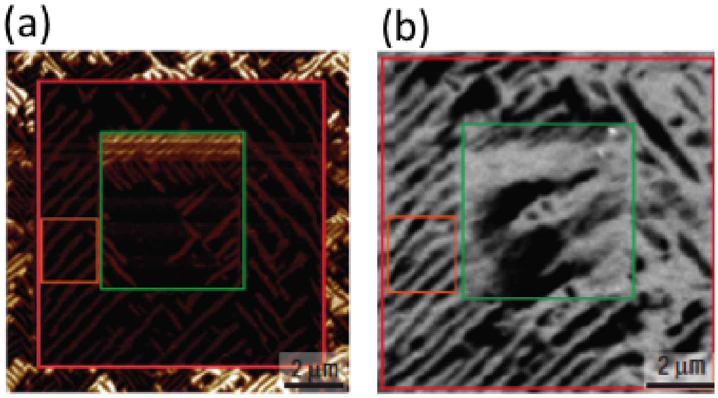

Polarization domain

Magnetization domain

Figure 1.6: (a) PFM image of polarization domain on the (001) surface of BFO (b) PEEM

image of the same area showing the magnetic domain. The figures show a one to one correspondence between the two order parameters. From Y. H. Chu et al., Nat. Mater, v7, p478 (2008)

1.2 Problem addressed

In this thesis, we investigate the problem of nonlinear switching behavior in thin film ferroelectric devices. The electromagnetic response of these materials are not as well understood as traditional semiconductors. Due to the long range correlation, electromagnetic response in these materials show highly nonlinear behavior which in turn gives rise to often unpredictable and qualitatively novel dynamic operation. Also, different order parameters like strain and magnetism gets excited by the application of voltage. A self consistent solution of these order parameters are required to fully understand the dynamics. In this work, we study the switching behavior of bismuth ferrite, a representative strongly correlated material under different boundary conditions. We explain a number of experimental results that were not understood before. In order to study these effects, we developed a phase field model that can take arbitrary electrostatic and mechanical boundary condition at the length scale where experiments are performed with the relevant resolution. We implemented a number of efficient algorithms that allowed us to study the non-linear switching in real devices and make direct comparison- a feat lacking in the current literature.

1.3 Summary of main results

The main results presented in this thesis are summarized here.

1. Estimation of surface magnetic moment density at the AFM-FM interface and their coupling energy.

2. Implementation of a massively parallel phase field code that can simulate 1000X larger structure than the state of the art with arbitrary electrical and mechanical boundary conditions.

3. Explanation of 90 and 180 horizontal switch in BFO.

4. Design principle to prevent domain reconstruction during polarization reversal.

5. Prediction of switching energy in ultra scaled BFO islands.

6. Prediction of switching speed in ultra scaled BFO islands.
7. Prediction of domain dynamics behavior in the presence of misfit dislocations.

Chapter 2

Anti-ferromagnet Surface Moment Density

2.1 Introduction

Understanding the interface coupling properties between the AFM BFO and the FM CoFeB is essential for designing devices using these material combinations. During the switching of a coupled AFM-FM system, the dynamics is determined by the relevant magnetic energy scales. Specifically, we want to know the anisotropy energy of the AFM, the exchange coupling energy between the AFM and the FM and the surface magnetic moment density in the AFM layer. Determination of these relevant energy scales from hysteresis measurements is difficult due to the many unknowns associated with the AFM-FM interface. There are pinned and unpinned spins present on the AFM interface that give rise to exchange bias and exchange enhancement. Detailed modeling of angular hysteresis measurement is required to separate out the contribution of various spin species. In this chapter, we describe our angular hysteresis modeling theory that identifies the contribution of pinned and unpinned spins on the experimentally measured hysteresis and therefore determine all the relevant energy scales.

The hysteresis measurements on exchange coupled BFO-FM heterostructures have shown spin glass (SG) like behavior. The observed properties of the measured MH loops are: i) both exchange bias and coercivity enhancement are observed [6, 5, 34] ii) exchange bias is related to the length of 109° domain wall [34], iii) exchange bias scales as $\sim$1/domain size [33, 5] and iv) the cooling direction determines the anisotropy directions for both exchange bias and coercivity enhancement irrespective of the AFM crystal orientation [23]. However, despite multiple experimental demonstrations, the physical origin of the exchange bias, coercivity enhancement, surface moment density and their magnitudes at the BFO-FM interface are currently unknown.

SG like behavior is a common phenomena in multiferroic materials exchange coupled to FM [5, 44, 24]. One of the major barriers for understanding the physical nature of SG systems is the uncertainty associated with the interface. Exhaustive neutron reflectometry characterization can be performed to estimate the surface AFM density. However, no information about the relevant energy scales can be obtained in this measurement alone. In contrast, magnetic hysteresis measurements are suitable for probing energy parameters but a significant AFM moment density could lead to erroneous estimation of relevant energies. Currently there is no systematic procedure available for determining the effect of AFM moment density on the magnetic energy parameters derived from these experimental measurements. Here, we propose a generic formalism for determining the magnitude of the anisotropies, exchange energies and the surface moment density of a SG system by combining azimuthal hysteresis and a critical angle hysteresis measurement. This scheme allows us to systematically separate out the contribution of individual spin species from their coupled behavior demonstrated in experiments. We emphasize that neglecting the AFM surface moment density in the calculation could significantly underestimate the actual energy contributions in the system. We find a surprisingly high AFM moment at the BFO-FM interface that is corroborated by neutron reflectometry measurement [5].

In a SG system, due to the presence of a symmetry breaking field, the azimuthal hysteresis measurement can show intricate phase properties. Specially, a critical angle is found below 90° where the hysteresis collapses [8]. In this work, we show that the necessary condition for the collapse of the hysteresis at the critical angle is that there can be no phase lag between the FM and the AFM during rotation. The phase lag between the FM and the AFM is determined by three factors, namely, the magnitudes of the interface coupling energy, the AFM unpinned moment anisotropy and surface density. By analyzing the phase lag information, one can narrow the phase space for the relative energy scales and surface moment densities of the AFM. Thus deterministic information about the relevant energies and the moment densities can be obtained from azimuthal hysteresis measurement.

2.2 Structure and Theory

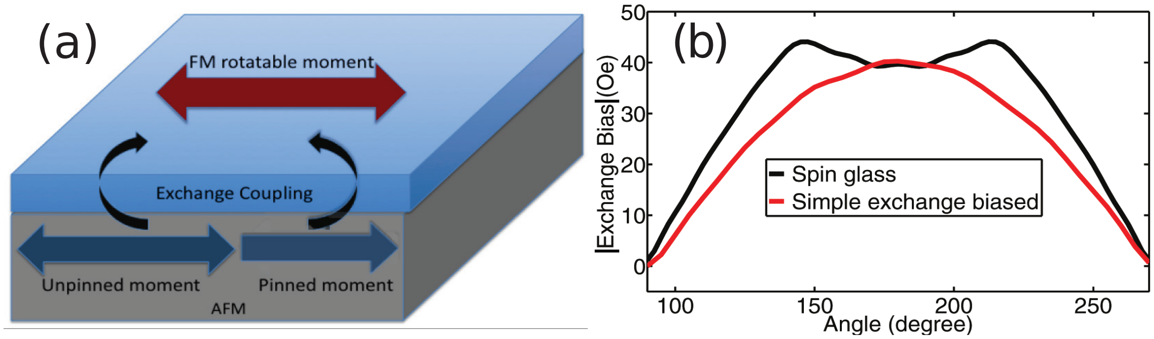

Figure 2.1: (a) Schematic of the exchanged coupled BFO-FM system modeled. The FM is considered as a macrospin moment. The AFM has pinned and unpinned moments. The pinned moment creates an exchange bias and the unpinned moment rotate with the FM and cause coercivity enhancement. (b) Azimuthal exchange bias for SG (black lines) and

simple exchange biased (red lines) system. The simple exchange bias shows usual cosine behavior with angular variation. The SG system shows a peak bias at a critical angle before reducing to zero at 90^0.

The starting point of our formulation is the so-called Miklejohn and Bean (MB) model that has been used with considerable success for describing the magnetization reversal in exchange coupled systems [36]. Here, we have modified the standard MB model by incorporating the AFM moment along with the ferromagnetic system. The simulated system is shown in Fig.2.1(a). Here the thin film FM is taken as a single macrospin whereas the AFM has two macrospin species on the surface, namely the pinned and the unpinned spins. The pinned spin has a high anisotropy compared to the exchange coupling energy. They produce a net shift of the measured MH loop from the FM only loop, giving rise to the effective exchange bias field. The unpinned spins have relatively lower anisotropy energy compared to the coupling energy. They increase the coercive field of the hysteresis loop that is known as coercivity enhancement. In a BFO AFM-FM system, both exchange bias and coercivity enhancement have been observed. Since the FM material used in the experiments are soft magnets, both bias and coercivity enhancement originate due to the different spin species on the BFO surface [5, 34, 23]. This is why incorporation of both spin species is important to capture the physics involved in the measured hysteresis loop. The magnetic energy per unit area of the coupled system is described by the following modified MB model.

$$
\begin{aligned}
E/area \quad &= -M_{FM} \times t_{FM} \times H_{app} \times cos(\theta - \alpha) - J_{ebpinned} \times cos(\alpha) \\
&-K_{FM} \times t_{FM} \times cos(\alpha)^2 - M_{AFM}^{S} \times H_{app} \\
&\times cos(\theta - \beta) - K_{AFMunpinned}^{S} \times cos(\beta)^2 - J_{ebunpinned} \\
&\times cos(\beta - \alpha) \qquad (2.1)
\end{aligned}
$$

Here, K_{FM} and M_{FM} are the FM anisotropy and saturation magnetization respectively. The surface AFM unpinned moment anisotropy and density are $K^{S}{}_{AFMunpinned}$ and $M^{S}{}_{AFM}$ respectively. Finally the interface coupling energy, $J_{ebpinned}$ and $J_{ebunpinned}$ are between the FM moment and the pinned and the unpinned AFM moments respectively. The pinned spins produce an effective field along the pinning direction on the FM. Its effect is included by the second term in eqn. (1). No coupling between the pinned and the unpinned spins are assumed, since any significant coupling between the two species would forbid the observation of spin glass behavior in the experiment. The angles of the FM and the AFM with respect to the pinning direction are α and β respectively. The field, H_{app} is applied at θ angle with respect to the field cooling direction. In all cases considered here, pinning and cooling directions are the same although in general, they could be different. The energy parameters were derived from the experimental data as described in section 2.4. From now on we shall use 'simple exchange biased' (SEB) system to address systems that show only exchange bias. SEB systems may or may not have AFM unpinned moment. Even if they have unpinned spins, their anisotropy is negligible so that no appreciable coercivity enhancement is observed in these systems. By contrast, the SG systems show both exchange bias and coercivity enhancement.

The azimuthal exchange bias of a SG system shows qualitatively different behavior than the SEB system. Fig.2.1(b) shows the azimuthal bias for an SEB (red line) and a SG (black line) system. The azimuthal exchange bias and coercivity enhancement are calculated from the MH loops at different angles with respect to the pinning direction. These M-H loops are calculated for each azimuthal angle by minimizing the per unit are energy given in eq. 1 numerically. The field step was 1 Oe for the hysteresis loop calculation. The angular step was 5° for the azimuthal hysteresis calculation. From the coercive field of the MH loop, the exchange bias and coercivity enhancement are calculated.

In an SEB system, where the anisotropy of the unpinned spins is negligible, the magnitude of the bias varies as a cosine function with increasing angle with respect to the pinning field direction which is defined as the direction where exchange bias is the maximum. In the same system, if the AFM unpinned spins produce significant coercivity enhancement that is comparable to the pinning field, then the shape of the azimuthal bias field deviates from a simple cosine behavior as shown in Fig.2.1(b). Starting from the pinning direction, the exchange bias decreases but then starts increasing and reaches a peak at a critical angle θ_{crit}.

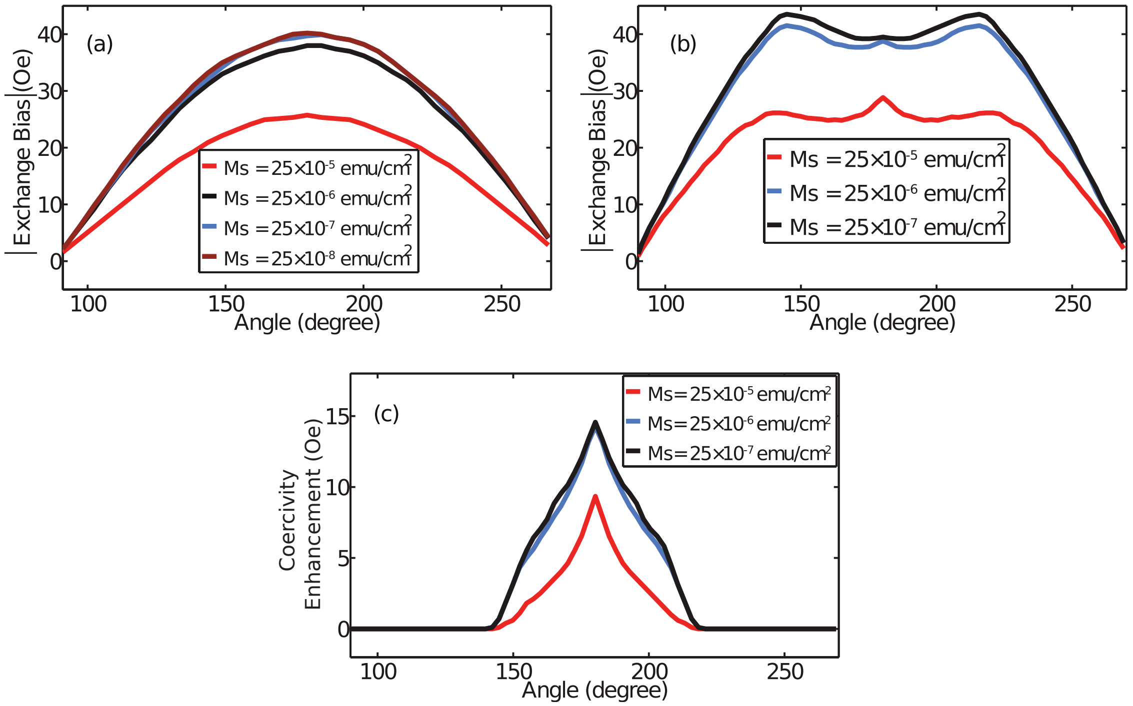

Figure 2.2: Effect of AFM surface magnetic moment density on exchange coupled systems. Exchange bias versus the measuring angle for (a) the SEB system and b) the SG system. In both cases exchange bias decreases with increasing AFM moment density. A change in the shape of the overall behavior specific to the SG system is also observed. (c) Coercive field versus the measuring angle for SG system showing a change from convex to concave dependence with respect to the vertical symmetry axis with increasing AFM moment density.

The magnitude of this angle is determined by the ratio of the anisotropy of the AFM unpinned spin and the pinning field magnitude that is similar to the effect described in Ref. [8]. The critical angle increases with increasing AFM unpinned spin anisotropy and decreases with increasing pinning field magnitude. Note that the system studied in this work is significantly different from the system studied in Ref. [8]. In Ref. [8], a hard magnet exchange biased by an AFM that has only pinned spins on its surface was studied. In this study we have modeled a soft magnet exchange biased by an AFM that has both pinned and unpinned spin on its surface. The presence of unpinned spins with comparable anisotropy, exchange energy and surface moment density makes it difficult to obtain deterministic information about the system. We particularly emphasize on the systematic method of finding a narrow phase space for the relevant energy scales and surface unpinned AFM moment density so that deterministic information can be obtained. In our model when the AFM unpinned moment and the FM moment are strongly coupled, they act as a hard magnet exchange biased by an AFM that has only pinned spin on its surface. Thus the model proposed in Ref. [8] is a limiting case of our model. A similar system was studied in Ref. [17] where the effect of AFM domain wall was included as a unidirectional field acting on the FM. For competing anisotropy and exchange energies, the angular hysteresis in Ref. [17] (Fig 2(b)) is similar to the SG angular hysteresis reported in this work. For very high exchange coupling, the angular hysteresis in Ref. [17] (Fig 2(d)) is similar to the SEB angular hysteresis reported in this work. Thus our results are in conformity with that of Ref. [17]. However, in this work, we have included the AFM unpinned spin in the magnetic energy expression, whose variation has significant impact on the observed hysteresis measurements that can be systematically determined.

2.3 Results and Discussion

For AFM surfaces that show SG like behavior, it is possible to infer from an azimuthal hysteresis measurement if the unpinned spin density is comparable to the FM surface spin density. To illustrate this point, we analyze the effect of exchange coupling energy and the AFM surface moment density on the observed azimuthal hysteresis measurement.

Effect of Antiferromagnet Surface Spin Density on SEB and SG systems

The azimuthal hysteresis of the SEB and SG systems are affected by the AFM surface moment density. The experimentally observed exchange bias in an SEB system reduces with increasing AFM surface moment density. However, for SEB systems, the characteristic cosine behavior of the azimuthal exchange bias do not change with increasing AFM moment density as shown in Figure. 2.2(a). Here the FM surface moment density is 500e^{-6} emu/cm^2. Fig. 2.2(a) shows that the change in the exchange bias drops significantly when the FM is comparable to the AFM. Here, we derive the azimuthal exchange bias of a SEB system analytically. Our starting point is the generic energy expression in equation (2.1). For a SEB system, the anisotropy of the AFM unpinned moment is negligible. Hence, K$_{AFMunpinned}$=0. Also the FMs considered in this study are soft magnets. They have a negligible coercive field compared to the coercivity enhancement and exchange bias in coupled AFM-FM system. We can neglect the FM anisotropy in the energy expression for this system. In this system, the FM and AFM unpinned moment remain completely coupled during the magnetization rotation and the system can be simply represented with a total moment of the FM and the unpinned AFM. This physical assumption allows to use the condition $\alpha=\beta$ in the energy expression. Thus the unit area energy expression and the azimuthal coercive field for this system can be written as

$$\begin{aligned} E/area \quad &= -(M_{FM} \times t_{FM} + M^S_{AFM}) \times H_{app} \times cos(\theta - \alpha) - J_{ebpinned} \times cos(\alpha) \\ &-J_{ebunpinned} \end{aligned}$$

Now, minimizing equation 2 with respect to α, we get,

$$0 = -(M_{FM} \times t_{FM} + M^S_{AFM}) \times H_{app} \times sin(\theta - \alpha) + J_{ebpinned} \times sin(\alpha)$$

At the coercive field, we have θ-α=$\pi/2$[7]. With this condition and writing H_{app}=$H_c(\theta)$, the above equation becomes,

$$|H_c(\theta)| = \frac{J_{ebpinned}}{(M_{FM} \times t_{FM} + M^S_{AFM})} \times cos(\theta) \tag{2.2}$$

The detailed derivation of the above equation and comparison to numerical result is shown in the Appendix. Note that since we have neglected the FM and AFM unpinned moment anisotropies, the azimuthal coercive field expression derived above is the same as the azimuthal exchange bias in the system. Since the characteristics of the azimuthal bias do not change with increasing AFM moment density, in the SEB system, azimuthal exchange bias can not provide definitive information about the AFM surface moment density. Hence there remains uncertainties about the actual energetics of the interface.

Change of the AFM surface moment produces a qualitative change of the azimuthal exchange bias and coercivity enhancement in a SG system as shown in Figure. 2.2(b) and (c) respectively. Here, the AFM surface moment density is varied from $25X10^{-7}$ emu/cm^2 to $25X10^{-5}$ emu/cm^2. As the unpinned moment density becomes comparable to the FM on top of it, the exchange bias along the pinning direction reduces significantly due to the higher effective moment. However, the exchange bias at the critical angle reduces faster than the bias along the pinning direction. Along θ_{crit}, the reduction in Heb is facilitated by the reduction in phase lag between the FM and the AFM due to enhanced Zeeman coupling of the AFM moment to the applied field. With sufficiently high AFM moment density, the maximum exchange bias no longer occurs at the critical angle. Rather the pinning direction exhibits the maximum bias magnitude. Figure. 2.2(c) shows the coercivity enhancement for the same variation of the AFM surface moment density. Similar to the exchange bias, the azimuthal coercive field also changes shape. The convex shape of the coercive field curve with respect to the symmetric vertical axis gradually changes to concave shape as the surface moment density becomes appreciable (i.e. comparable to the FM surface moment density, 500X10^{-6} emu/cm^2 in this case). Also the peak value of the coercive field decreases significantly along all the measuring angles. The critical angle remains the same in all the cases. These characteristic change in the azimuthal hysteresis can be used to obtain definitive information about the surface AFM moment density in a SG system as discussed below.

Phase Lag Between AFM and FM During Magnetization Reversal

The characteristic change of the azimuthal hysteresis of the SG system is a sign of the presence of AFM surface moment. However, it is not possible to use this information to find out quantitative information about the AFM density. In this work, we show that the hysteresis at the critical angle is sensitive to the relative magnitude of surface moment density of the FM and the AFM. One can use this information to deterministically find out if the AFM moment density is indeed comparable to the FM surface moment density.

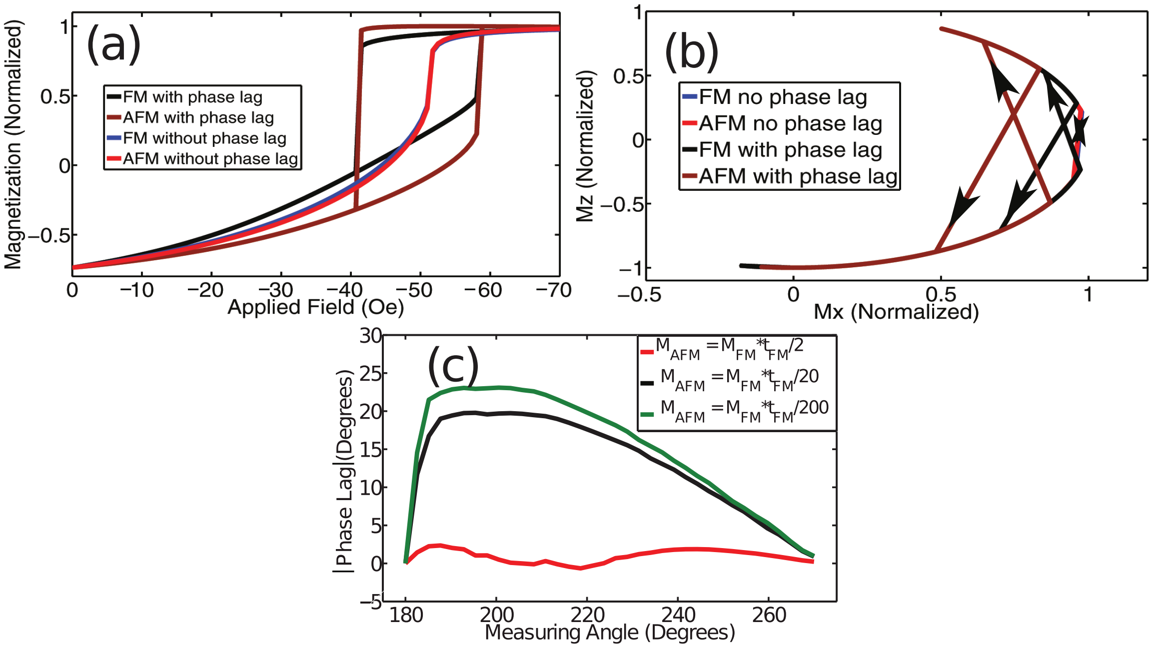

Figure 2.3: (a) Magnetization versus applied field for the SG system at the critical angle where exchange bias maximizes. When the exchange coupling is an order of magnitude larger than the anisotropies ($J_{eb}/K^S{}_{AFMunpinned}$=20), no hysteresis is observed for the FM and the AFM. With comparable exchange coupling ($J_{eb}/K^S{}_{AFMunpinned}$=3), there is significant hysteresis for both FM and the AFM. (b) Normal components of the magnetization during field sweep at the critical angle. For low exchange coupling, both the FM and AFM shows jump and hence cause hysteresis. With high exchange energy, both the FM and AFM rotate coherently. Hence the hysteresis collapse. (c) The phase lag of the AFM with respect to the FM, in the forward branch of the hysteresis loop with varying AFM moment density. Here, $J_{eb}/K^S{}_{AFMunpinned}$=3. The pinning field is opposite to the forward branch.

The presence or absence of hysteresis at the critical angle depends on the phase lag between the FM and the AFM. At the critical angle, if there is no phase lag between the FM and the AFM during rotation, then hysteresis collapses in a MH measurement at this angle. In the case of a strongly coupled SG system that essentially behaves as a hard magnet, at the critical angle, there is no phase lag during magnetization rotation and hence the hysteresis collapses in the MH measurement. Fig.2.3 (a) shows magnetization versus applied field for the SG system at the critical angle where exchange bias maximizes. In this case the coercivity enhancement reduces to zero for both the FM and the AFM (blue and red line respectively). At this angle, the coupled system starts to rotate coherently [8]. However, for a SG system with exchange coupling comparable to the anisotropy, there is still hysteresis present in the magnetic measurement if the AFM lags behind the FM during magnetization reversal. In order to understand this difference, we plot the Mx Vs. the Mz component of the magnetization at the critical angle in Fig.2.3(b) where Mz is the component opposite to the pinning direction. As expected, the strongly coupled magnet shows coherent rotation and hence no hysteresis is observed (Fig.2.3(b)). However, for the weakly coupled system, the AFM lags the FM before switching. After switching the AFM starts to lead the FM. Hence the coupled system do not follow the same path for switching in the forward and the reverse branch. For low exchange coupling, both the FM and AFM shows jump and hence cause hysteresis. Notably the coercivity enhancement is zero since there is no zero crossing of the parallel component of the magnetization in the hysteresis measurement. Thus the hysteresis at the critical angle is a measure of the phase lag between the FM and the AFM. The phase lag Vs. the measuring angle just before switching in the forward branch is shown is Fig.2.3(c) with varying AFM surface moment densities. It is clear that phase lag decreases significantly as the AFM moment is increased particularly when the surface moment densities of the AFM and the FM are comparable.

High Coupling Energy Versus High AFM Surface Moment Density

From the discussion above, it is evident that the hysteresis in a SG system at the critical angle will collapse in two cases. First, if the exchange energy is orders of magnitude higher compared to the AFM anisotropy so that the AFM and the FM moment will be completely coupled at all the measuring angles and no phase lag will be present. The system would essentially behave as a hard magnet exchange biased by an AFM. In the second case, the surface spin density of the AFM could be too high, so that when a field is applied at an angle with respect to the pinning direction, both the FM and the AFM follow the applied field under the Zeeman energy and hence no phase lag occurs between the two. The azimuthal exchange bias and coercivity enhancement for the two cases with same anisotropy energies are shown in Fig.2.4. An analytical relation between the exchange bias and coercivity enhancement along the pinning and θ_{crit} can be given for the strongly coupled case following the astroid diagram in Ref. [8].

$$Heb_{pinning} = Heb_{\theta_{crit}} \times cos(\theta_{crit}) \tag{2.3}$$

$$Hc_{pinning} = Heb_{\theta_{crit}} \times sin(\theta_{crit}) \tag{2.4}$$

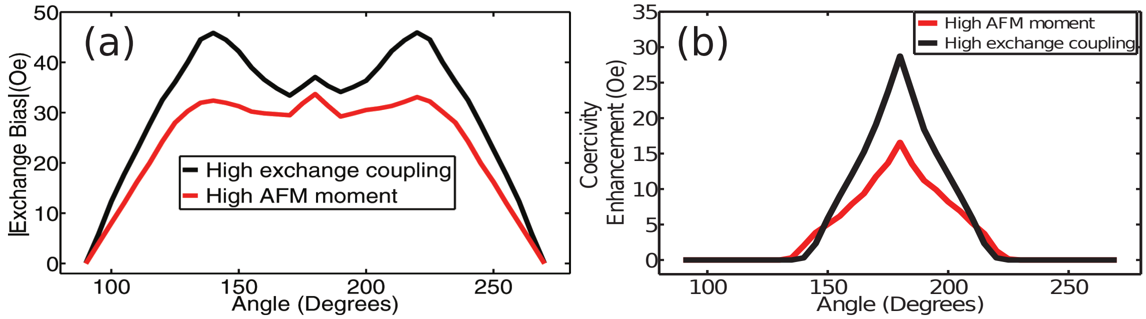

Figure 2.4: (a) Azimuthal exchange bias and (b) Azimuthal coercive field with strong exchange coupling and high AFM moment. The exchange bias at the critical angle is considerably larger than the bias at the pinning direction when the coupling energy is high. In a strongly coupled system, for the same anisotropy, the coercive field along the pinning direction is considerably higher.

For the strongly coupled system, the exchange bias is significantly larger than the bias along the pinning direction. The coercive field along the pinning direction is also considerably higher for the strongly coupled system than the system with high moment density. The decrease of exchange bias and coercivity enhancement along the pinning direction for the high AFM results from the additional moment contribution from the AFM surface. With increasing AFM surface moment, the exchange bias along θ_{crit} reduces faster than that along the pinning direction. In order for the correct determination of the effect of surface AFM moment on the measured hysteresis measurement, these two cases need to be separated. As discussed above, the above two physical situations can be readily separated by applying equation 3 and 4 to the azimuthal hysteresis measurement. For the strongly coupled case, the equations hold, while they do not hold for the low coupling region.

2.4 Comparison to Experiment

We apply our model for analyzing experimental hysteresis measurements where a soft FM was used. Notably, this model is appropriate for describing the azimuthal hysteresis properties of a soft magnet exchange biased by an AFM that has both pinned and unpinned spins on its surface. The system shows SG behavior and the coupling regime is determined to be the low coupling energy regime. We do not study the high coupling region since in this region, the exchange coupled system behaves as a hard magnet biased by an AFM. In that case, the azimuthal hysteresis can be described satisfactorily using the model proposed in Ref. [8].

Table 2.1: Calculated parameters of BFO-FM interface. The same parameters of BFO reproduces the hysteresis properties reported from two different groups using different FM materials.

Material	Parameter	Value
BFO	$K^S{}_{AFMunpinned}$	10×10^{-3} erg/cm^2
	$K_{AFMpinned}$	12.5×10^3 erg/cm^3
	$J_{ebpinned}$	25×10^{-3} erg/cm^2
	$J_{ebunpinned}$	25×10^{-3} erg/cm^2
	$M^S{}_{AFM}$	250×10^{-6} emu/cm^2
FM	K_{FM}	333.3 erg/cm^3 $^{Ref.}$ [6, 5, 23]
		4500 erg/cm^3 $^{Ref.}$ [34]
	M_{FM}	666.67emu/cm$^{3Ref.}$[6, 5, 23]
		1500 emu/cm^3 $^{Ref.}$[34]

The azimuthal hysteresis calculated here are obtained by using energy values relevant to recent experimental measurements of BFO-FM exchange coupled systems. The energy values are primarily estimated form the hysteresis measurement data along the easy axis reported in Ref. [6, 5] assuming negligible $M^S{}_{AFM}$. However, these estimated energy values cannot describe the azimuthal hysteresis and the MH at the critical angle self consistently. In order to reproduce the azimuthal exchange bias and coercivity enhancement and the hysteresis at the critical angle, reported in Ref. [23], a significant AFM moment had to be incorporated following the arguments presented in the preceding section.

For the BFO-FM exchange coupled system, the energy values of interest are described in Eqn. (2.1). The anisotropies K_{FM} and the saturation magnetizations M_{FM} of the FM used by the two experimental groups with which we compare our simulations, are estimated from the measured FM only hysteresis measurements and tabulated in Table I [6, 34]. The magnitude of interfacial coupling energy, $J_{ebpinned}$ between the pinned spins and the FM moment can be calculated from the exchange bias measured for a given FM thickness [36, 5] provided the AFM is thick enough so that the exchange bias field has saturated. For a known t_{FM} and M_{FM}, the interface energy is given by,

$$J_{ebpinned} = Heb \times M_{FM} \times t_{FM} \tag{2.5}$$

With the estimated coupling energy, it is possible to find the pinned spin anisotropy by finding the onset of exchange bias as the AFM thickness is increased. Figure. 2.5(a) shows the Exchange bias Vs. BFO thickness calculation compared to the measured data from Ref. [5]. The AFM BFO thickness is varied from 5nm to 1000 nm. It was assumed that the AFM anisotropy varies linearly with thickness. As the AFM thickness is increased from 5nm, a phase transformation occurs at about 18nm where the exchange bias field starts increasing from 0. At this thickness, the AFM anisotropy energy is equal to the interface coupling energy [36],

$$J_{ebpinned} = K_{AFMpinned} \times t^{cr}_{AFM} \tag{2.6}$$

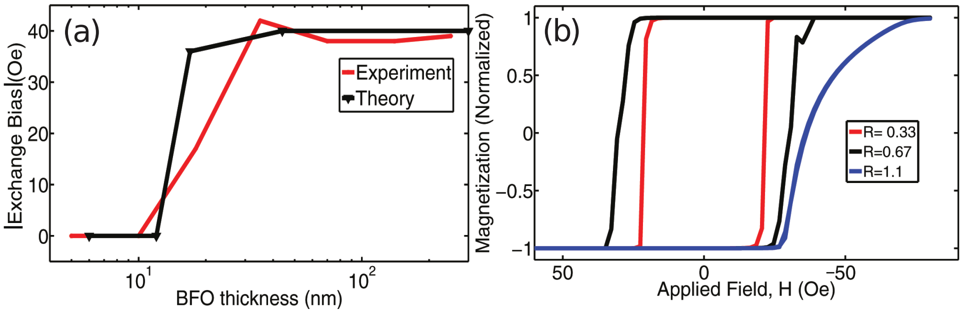

Figure 2.5: a) Exchange bias Vs. AFM thickness calculation for BFO-FM SEB system (black color online). It was assumed that the AFM anisotropy varies linearly with thickness. The anisotropy energy of the pinned moment is estimated by matching with the exchange bias at the critical thickness where the bias ensues. The experimental values are taken from [5]. b) Hysteresis loops as the ratio R=J_{eb}/KAFM is varied. The hysteresis becomes gradually slanted as R increases. The square like hysteresis in the experiment indicate R < 0.5.

From the estimated $J_{ebpinned}$ and the observed t^{cr}_{AFM}, $K_{AFMpinned}$ can be calculated. Having estimated the interface coupling energy, $J_{ebpinned}$ between the FM and the pinned AFM moment, we use the same order of magnitude value for the coupling energy between the FM and the unpinned AFM moments, $J_{ebunpinned}$. For the specific system studied here, these two coupling energies cannot be significantly different. The high coupling regime can be excluded by invoking equations 3 and 4 on the azimuthal hysteresis data. On the other hand, if $J_{ebunpinned}$ is too low, then the system would not show SG behavior. This similar amplitude of $J_{ebpinned}$ and $J_{ebunpinned}$ does not have to hold in general, for other material systems, where the model will be equally applicable. The equivalence of the two energies implies that the areal spread of the two spin components are similar. Considering a magneto-electric coupling between the ferroelectric (FE) and the anti-ferromegnetic (AFM) order parameter in BFO, it is possible that these two species have similar spatial spread. Once the $J_{ebunpinned}$ is estimated, a range for the unpinned spin anisotropy can be obtained by observing the properties of the hysteresis loops along the easy direction. Figure. 2.5(b) shows the hysteresis loops as the ratio R=$J_{ebunpinned}/K^{S}{}_{AFMunpinned}$ is varied. The hysteresis becomes gradually slanted as R increases. The square like hysteresis in the experiment indicate R < 0.5.

For the case of the azimuthal hysteresis of BFO-CoFeB reported in Ref. [23], we find that at the measuring angle of 45° with respect to the pinning direction, there is no hysteresis in the magnetization measurement. The measuring angle is very close to the θ_{crit} (∼40°)

for this device. With the reported Heb ∼38 Oe along the pinning direction, the expected Heb$_{\theta crit}$ from eqn. 2 is ∼50 Oe that is considerably larger than the measured Heb$_{\theta crit}$ ∼40 Oe. Hence we can exclude the strongly coupled case and argue that the coupling energy in the system must be of the same order of magnitude as the AFM anisotropy energy.

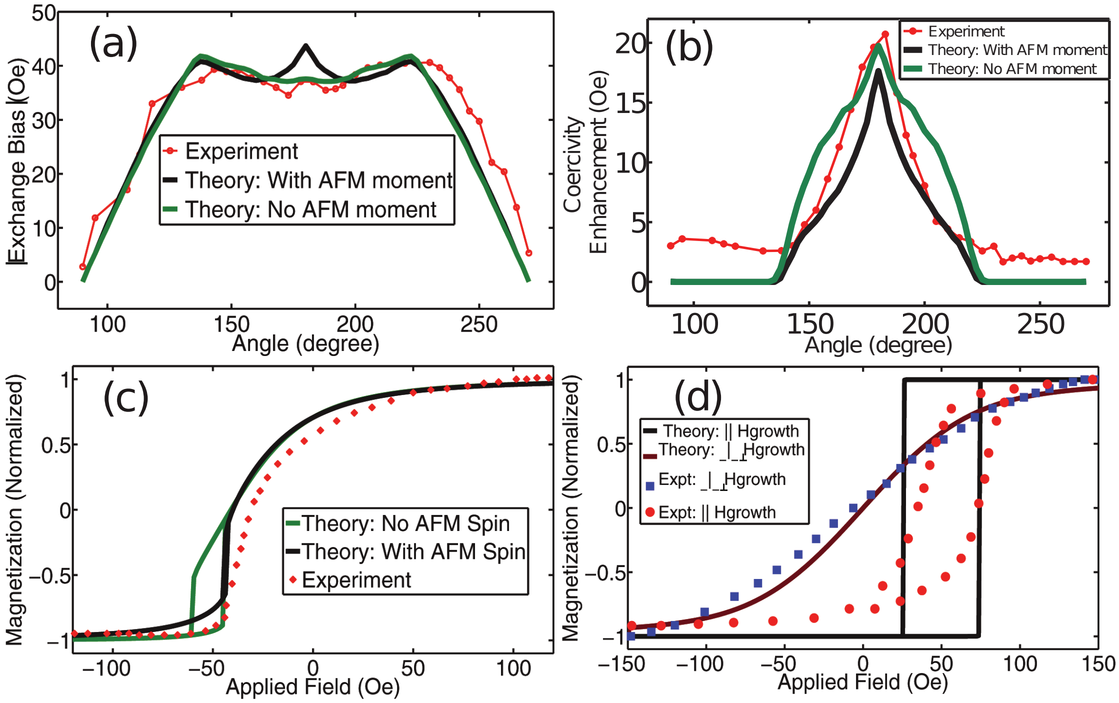

Figure 2.6: Comparison to experiment. The angle dependence of (a) the exchange bias and (b) the coercive field for the device reported in Ref. [23]. (c) The applied field versus the normalized longitudinal magnetization at 45° to the pinning direction. The collapsed hysteresis resembles the high AFM moment density. (d) Hysteresis parallel and perpendicular to the pinning direction for the device reported in Ref. [34] using a different FM material. The excellent agreement with experimental measurement indicates the robustness of the proposed scheme and calculated parameters.

In the low coupling regime, the azimuthal exchange bias can be satisfactorily matched with the experimental data in two ways (Fig. 5(b) of Ref. [23]). The azimuthal exchange bias is shown in Fig. 2.6(a) for the two significantly different values of the surface AFM moment densities. Either there is a low AFM surface moment density with low K$^{S}{}_{AFMunpinned}$ and J$_{ebunpinned}$ or a significant moment density with a relatively higher K$^{S}{}_{AFMunpinned}$ and J$_{ebunpinned}$. For these two cases, the coercive field as a function of measuring angle shows change in shape. The resemblance of the experimental coercive field (brown dotted line) to the high AFM moment configuration (violet solid line) from that of the low AFM moment configuration (blue dotted line) is evident as shown in Fig.2.6(b). A more concrete way of confirming high AFM moment can be looking at a magnetic hysteresis measurement at θ_{crit}.

Fig.2.6(c) shows the calculated hysteresis loop with and without significant AFM surface moment. The red dots are the experimental data points. The hysteresis has collapsed in the case with significant AFM surface moment that matches well with the experimental data. On the other hand, for a low AFM moment, as expected from a bulk theory for BFO, a significant hysteresis will ensue (see the green curve in Fig.2.6(c)). Presence of the high AFM moment at the interface is in agreement with the PNR measurements for this system [5]. It is not possible to describe both the azimuthal hysteresis and the critical angle hysteresis without inclusion of this high AFM moment. Interestingly, the same energy parameters quantitatively reproduce measured hysteresis loops along easy and hard axes for a BFO-CoFe(note the difference in the FM material) reported from a different group [34] (see Fig.2.6(d)), thereby establishing the robustness of these energy values. This shows that, by first comparing the dependence of exchange bias and coercive field as a function of measurement direction and then by calculating the phase lag by probing hysteresis at the critical angle, it is possible to deterministically estimate surface AFM moment of a SG system. This is the central result of this chapter. The energy values estimated for the BFO-FM system is tabulated in Table I. Note that for this specific system, the same value of $J_{ebunpinned}$ and $J_{ebpinned}$ reproduces the both the azimuthal hysteresis and the critical angle MH. For the specific system studied in this work, it is not possible for these two energies to be significantly different. Also, the two parameters $K^{S}{}_{AFMunpinned}$ and $M^{S}{}_{AFM}$ are surface quantities rather than volume quantities. This is because, the effective thickness of the AFM over which the unpinned spin species should be defined is unknown. The reported experimental angular hysteresis data of the BFO-FM system suggest that there is a high unpinned AFM surface moment density at the interface independent of the thickness of this particular spin species. This result is unexpected as BFO is a G-type anti-ferromagnet. Here, we provide an estimation of the surface density of the unpinned moment and emphasize that a detailed study of the origin of this moment and effective thickness requires future study.

2.5 Conclusion

In summary, with thin film FM hysteresis measurement, it is possible to systematically find out the AFM surface moment and the coupling between the FM and the AFM moment in a SG system. Note that in the specific example of BFO-FM system, we found the exchange coupling to be the same for both the pinned and the unpinned moments with the FM. This is not a priori knowledge since the physical origin of exchange bias and coercivity enhancement in these perovskite interfaces are still a matter of ongoing debate [14, 32]. This finding, combined with the experimental observation that the exchange bias and coercivity enhancement do not depend on the crystal orientation of BFO [23] suggests that the physical nature of coupling for the pinned and the unpinned spin to the FM are similar. In any case, azimuthal hysteresis measurement is a relatively straight forward experimental way of finding out if the measured magnetic properties are affected by the AFM surface moment density in a SG system. The estimated AFM moment density at the BFO-CoFeB is considerably higher than that would be expected from the compensated (001)surface of a G type AFM [15]. The calculated AFM surface moment density is consistent with the PNR measurement for the BFO-CoFeB system that predicts a value of 30 μemu/cm^2 within 2 nm of BFO at the interface [5]. Reproduction of the hysteresis reported form a different group using different FM material [34] demonstrates the robustness of the calculated energy values. A measurement of hysteresis at the critical angle for this structure will provide further insight into the AFM moment density for this system. The surprisingly large AFM surface moment density indicates significant modulation of the surface from that would be otherwise expected from a bulk theory and needs to be studied carefully for achieving deterministic electric field driven magnetic switching in these systems.

2.6 Appendix

Here, we derive the equation 2 in the manuscript starting from the generic energy expression in equation 1. For a SEB system, the anisotropy of the AFM unpinned moment are negligible. Hence, K$_{AFMunpinned}$=0. The magnets studied here are soft magnets that have negligible anisotropy. Hence, we neglect the FM anisotropy as well in the calculation and put K$_{FM}$=0. Starting from the generic energy expression in eq. 1, for SEB system, the energy expression becomes,

$$\begin{aligned} E/area &= -M_{FM} \times t_{FM} \times H_{app} \times cos(\theta-\alpha) - J_{ebpinned} \times cos(\alpha) \\ &\quad -M^S_{AFM} \times H_{app} \times cos(\theta-\beta) - J_{ebunpinned} \times cos(\beta-\alpha) \end{aligned} \tag{2.7}$$

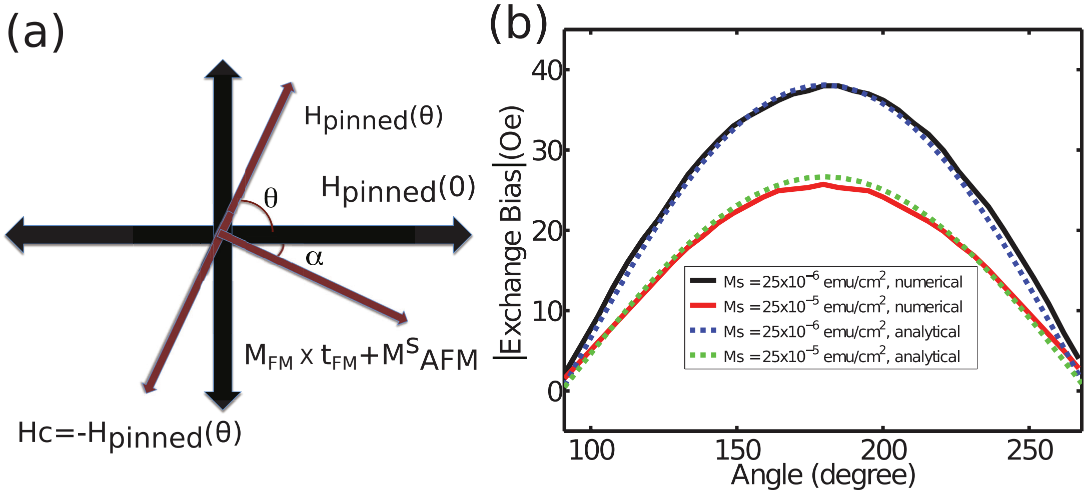

Figure 2.7: (a) Direction of the magnetic moments and the fields with respect to the pinning direction. For a SEB system, K$^S{}_{AFMunpinned}$=0. Since, we studied a soft FM in this work, K$_{FM}$=0. Since, both unpinned AFM moment and FM have negligible coercivity, they will remain exchange coupled during the magnetization rotation. The total surface moment density of the rotating moment is (M$_{FM}$*t$_{FM}$+M$^S{}_{AFM}$). (b) Comparison of the

numerical and the analytical exchange bias for two different densities of the surface AFM unpinned moments. The numerical calculation was performed by minimizing eq. 1. On the other hand, the analytical values were calculated using eq. 2. The parameters used in this comparison are M$_{FM}$=666.67 emu/cm^3, t$_{FM}$=7.5 nm, M$^S{}_{AFM}$ was varied between 25X10^{-6} and 25X10^{-5} emu/cm^2, J$_{ebpinned}$=20X10^{-3} erg/cm^2, J$_{ebunpinned}$=20X10^{-3} erg/cm^2, K$_{FM}$=0 and K$^S{}_{AFMunpinned}$=0.

Since the FM and AFM unpinned moment have negligible anisotropy but significant exchange coupling, they remain completely coupled in an SEB system during magnetization reversal. Hence in the above equation, we can use α=β. The correctness of this assumption will be later justified by comparing with numerical results that minimizes the generic energy expression where this assumption is not included. The orientation of the magnetic moment and applied field with respect to the pinning direction is shown in Fig 2.7(a). The energy expression in this case becomes

$$\begin{aligned} E/area \quad &= -(M_{FM} \times t_{FM} + M^S_{AFM}) \times H_{app} \times cos(\theta - \alpha) - J_{ebpinned} \times cos(\alpha) \\ &-J_{ebunpinned} \end{aligned} \tag{2.8}$$

Now, minimizing equation 2 with respect to α, we get,

$$\begin{aligned} \frac{\delta E}{\delta \alpha} &= -(M_{FM} \times t_{FM} + M^S_{AFM}) \times H_{app} \times sin(\theta - \alpha) + J_{ebpinned} \times sin(\alpha) \\ => 0 &= -(M_{FM} \times t_{FM} + M^S_{AFM}) \times H_{app} \times sin(\theta - \alpha) + J_{ebpinned} \times sin(\alpha) \end{aligned} \tag{2.9}$$

At the coercive field, θ-α=$\pi/2$ [11] Hence, equation 3 becomes,

$$=> 0 = -(M_{FM} \times t_{FM} + M^S_{AFM}) \times H_{app} + J_{ebpinned} \times sin(\theta - \pi/2) \tag{2.10}$$

Hence, the azimuthal dependence of the coercive field can be written as

$$=> |H_c(\theta)| = \frac{J_{ebpinned}}{(M_{FM} \times t_{FM} + M^S_{AFM})} \times cos(\theta) \tag{2.11}$$

Note that since we have neglected the FM and AFM unpinned moment anisotropies, the azimuthal coercive field expression derived above is the same as the azimuthal exchange bias in the system.

Using the analytical equation derived above, we plot the angular exchange bias of a SEB system as shown in Fig. 2.7(b). We also compare the analytical values with that of the numerical calculations presented in Fig. 2.2(a). The parameters used in this comparison are M$_{FM}$=666.67 emu/cm^3, t$_{FM}$=7.5 nm, M$^S{}_{AFM}$ was varied between 25X10^{-6} and 25X10^{-5} emu/cm^2, J$_{ebpinned}$=20X10^{-3} erg/cm^2, J$_{ebunpinned}$=20X10^{-3} erg/cm^2, K$_{FM}$=0 and K$^S{}_{AFMunpinned}$=0. From the comparison, we find that the analytical results and the numerical results are in excellent agreement. Note that the J$_{ebunpinned}$ parameter was only used in the numerical calculation. For the analytical calculation, it was assumed that the FM and AFM unpinned moment remain completely coupled during magnetization rotation. The agreement between the numerical and analytical results justifies this assumption.

Chapter 3

Phase Field Method

3.1 Introduction

The magnetic switching dynamics in a multi-ferroic device is determined by the ferroelectric switching dynamics. Although simple models can be constructed for switching dynamics of ferroelectrics, in device structures, many surface and domain wall driven physical effects arise that cannot be understood from the standalone ferroelectric itself. Electrostatic and mechanical boundary conditions in multi-domain ferroelectrics completely change the switching behavior. Thus it is necessary to build a model that can capture the switching dynamics in arbitrary device structures with different boundary conditions. The goal is to understand the ferroelectric domain switching observed in real experiments and estimate the switching speed and energy in these devices.

Understanding switching dynamics in multi-domain ferroelectric films influenced by arbitrary electrostatic and mechanical boundary condition remains to be a significant challenge. The origin of the difficulty lies in the coupling of multiple order parameters in these materials and the spatial asymmetry introduced by the domain walls. The necessity of being self consistent between various competing energies coming from chemical, electrostatic and elastic origin makes the temporal evolution of polarization a numerically stiff problem. Also ferroelectric domain walls are typically of the order of nm size whereas the whole pattern forms over micron sizes. This disparate length scales associated with ferroelectric domain walls and domains themselves necessitates a large degree of freedom to be simulated in order to achieve physically reasonable results. Under experimental conditions, the non-linear switching behavior makes it very difficult to design and characterize devices. Faced by these obstacles, it remains a significant challenge to make direct comparison of a simulation result with an experimental observation and also pursue rational device design using computational simulation. In this chapter, we describe a phase field model that calculates the local contribution of various thermodynamic energy contributions as a functional of a field, the polarization density field in this case. The spatial inhomogeneity is included automatically, since the simulation domain is divided into nano meter scale grids. A phase field model is especially suitable for problems involving moving boundaries where the polarization and the domain wall dynamics are calculated within the same theoretical methodology. In the following section, we describe the physical equations associated with phase field model and explain how it describes the phase transition and domain dynamics in ferroelectric systems.

3.2 Multi-domain Ferroelectric Switching

The macroscopic behavior of a ferroelectric switching and phase transition can be described at the mean field level using the Landau-Ginzberg theory. In this formalism, the non-linear energy of the ferroelectric is parametrized using the Landau coefficients. The required parameters for a given ferroelectric material is found by symmetry analysis of the parent crystal. Due to symmetry restriction, generally up to 4th or 6th order terms in the free energy expansion are required. Higher terms are suppressed due to renormalization of the polarization field at the macroscopic level. The figure below shows a typical switching of a monodomain bulk ferroelectric material under applied electric field. The coercive field and the saturation polarization are determined by the Landau coefficients for specific materials.

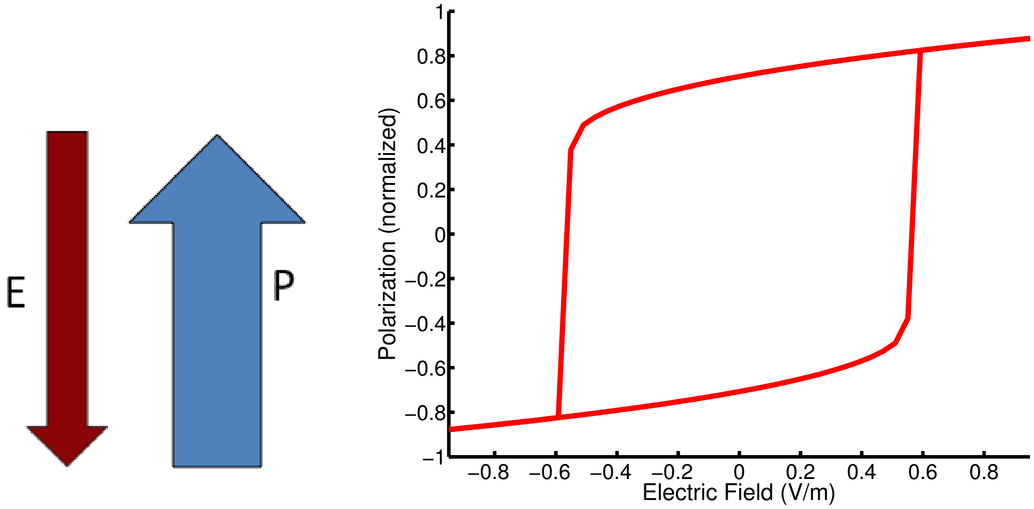

Figure 3.1: (a) Schematic of a polarization that is switching under the application of an electric field. (b) A typical hysteresis loop calculated for a monodomain ferroelectric using the Landau-Khalatnikov equation.

In real materials, there are always multiple ferroelectric domains present. Ferroelectrics break into domains in order to minimize the electrostatic energy. Electrostatic compatibility is achieved if the adjacent polarizations are anti-aligned. However, domain wall energy originating from strain want to align the adjacent polarizations. There is a competition between these two forces. Electrostatic energy increases with increasing thickness of a given domain. At a critical thickness of the polarization domain, the electrostatic energy becomes larger than the domain wall energy. In this case, the ferroelectric breaks into domains. The mechanism of domain wall formation is shown below.

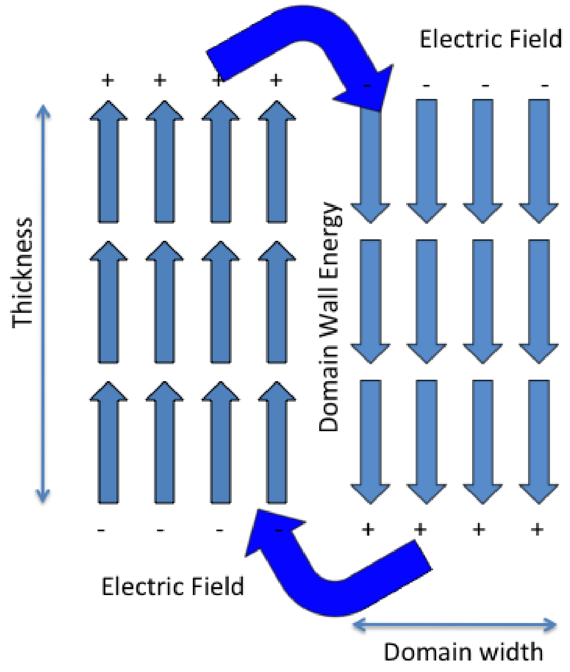

Figure 3.2: Physics of domain formation in a ferroelectric material. The domains are mainly formed from the electrostatic interaction incurred by the uncompensated charges on the surface.

In a multi-domain ferroelectric, the switching is initiated at the existing domain walls or defect locations. A multi-domain model is thus required to understand the realistic switching mechanism. Phase field method is particularly suited to study the dynamics in multi-domain ferroelectric materials. However, both short range and long range electrostatic, elastic, chemical and thermal effects and their coupling is needed to be incorporated to understand a given physical condition. We describe the thermodynamic theory of coupled electromechanical systems and the phase field description of ferroelectric materials.

3.3 Thermodynamic description of electromechanical systems

The thermodynamic equilibrium equation for a coupled electro-mechanical system is given by:

$$dW = TdS + \sigma_{ij} d\epsilon_{ij} + E_i dD_i \tag{3.1}$$

Here, T is temperature, S is entropy, σ_{ij} is the stress tensor and ϵ_{ij} is the strain tensor. In a ferro-electric material, the relevant order parameters are polarization P_i and strain ϵ_{ij}. Hence it is convenient to use the Helmholtz free energy:

$$dF = \sigma_{ij} d\epsilon_{ij} + E_i dP_i \tag{3.2}$$

Using the Helmholtz free energy of the system, it is possible to describe the polarization dynamics and phase transition when the external thermodynamic conditions are tuned.

3.4 Phase field description of ferroelectric systems

A phase field model describes the thermodynamic free energy of a system in terms of a continuous field variable. All the participating energies of the system are described as a function of this order parameter. For example, for ferroelectrics, the polarization is a suitable order parameter for describing the thermodynamic energy of the system. A continuum approximation for describing the spatiotemporal variation of the polarization facilitates describing the low energy dynamics of the system. Phase field model has been applied to understand ferroelectric domain switching [11, 37, 41, 51, 1, 47], strain effects [45, 43, 30, 27, 28, 12, 42, 31, 29] and random defect effects [38, 39]. We describe the various aspects of the theory only briefly here. For a comprehensive review of the theory, see the review by L. Q. Chen et al [9].

The relevant contributors to the thermodynamic energy of the ferroelectric system are the bulk energy, electrostatic energy, elastic energy and the domain wall energy.

Bulk Energy

The energy gained due to the phase transition from the paraelectric to the ferroelectric phase in a homogeneous unstrained ferroelectric is called the bulk energy and parameterized using the Landau coefficients. The bulk energy is given by

$$\begin{aligned} F_{bulk} = \alpha_1(P_x^2 + P_y^2 + P_z^2) + \alpha_{11}(P_x^4 + P_y^4 + P_z^4) \\ +\alpha_{12}(P_x^2 P_y^2 + P_y^2 P_z^2 + P_z^2 P_x^2) \end{aligned} \tag{3.3}$$

Here, P$_i$ are the polarization along the three (001) directions of the BFO crystal. The α's are the relevant Landau coefficients for different ferroelectrics. Note also that henceforth we will use i to denote crystallographic directions and I to denote the lab coordinate axis along which we will set up our numerical grid. Space directions are denoted by x for crystal directions and X for grid directions.

The bulk energy is useful for a mean field description of the ferroelectric. Ignoring the effect of domain walls and long range interaction, the bulk energy describes the paraelectric to ferroelectric phase transition as temperature is varied. The dependence of the polarization on the temperature can be calculated by minimizing the bulk energy with respect to polarization at varying temperatures. The expansion coefficient α relates the bulk energy with temperature through the relation,

$$\alpha_1 = \frac{\theta}{T - T_C} \tag{3.4}$$

Domain Wall Energy

In finite ferroelectrics, electrostatic compatibility is obtained by breaking the film into ferroelectric domains. The variation of order parameter at the domain wall causes an energy cost that originates due to both strain and dipole-dipole interaction. This additional price in energy is incorporated by the gradient of the polarization at the domain wall. The energy and the thermodynamic forces due to the domain walls are given by

$$\begin{aligned} F_{grad} = & G_{11}(P^{'}_{X,X} + P^{'}_{X,Y} + P^{'}_{X,Z} + P^{'}_{Y,X} \\ & + P^{'}_{Y,Y} + P^{'}_{Y,Z} + P^{'}_{Z,X} + P^{'}_{Z,Y} + P^{'}_{Z,Z}) \end{aligned} \tag{3.5}$$

$$\frac{\delta F_{grad}}{\delta P_i} = G_{11}\nabla^2 P_i \tag{3.6}$$

Here, $P^{'}_{I,I}$ are the gradient of polarization along the grid directions. G_{11} is the domain wall energy coefficient when the grid and crystal directions coincide. We only consider the first order term here. P_I is the projection of the polarization along the grid direction I.

Electrostatic Energy

In the phase field description, the inhomogeneous long range electrostatic interaction is taken into account by solving the 3D poisson equation with appropriate boundary condition. The electrostatic energy and field are given by

$$F_{elec} = -\vec{E} \cdot \vec{P} \tag{3.7}$$

$$-\frac{\delta F_{elec}}{\delta \vec{P}_I} = \vec{E}_I \tag{3.8}$$

Here, E_I are the effective electric field along the grid directions. This field incorporates contributions due to inhomogeneous polarization. The contribution of the applied field is added to the electrostatic potential assuming a linear dielectric. The depolarization field is calculated separately by summing over all the local contributions to the global polarization.

Mechanical Energy

The substrate constraint and domain variations within the ferroelectric film causes both homogeneous and inhomogeneous strain in the film. The effect of the elastic compatibility on the domain morphology is calculated by solving the stress-strain relation with thin film boundary condition. The elastic energy density is given by [9]

$$\begin{aligned} F_{elas} &= -\frac{1}{2} c_{ijkl} e_{ij} e_{kl} \\ &= c_{ijkl}(\epsilon_{ij} - \epsilon^0_{ij})(\epsilon_{kl} - \epsilon^0_{kl}) \end{aligned} \tag{3.9}$$

Here, c$_{ijkl}$ is the elastic modulus, ϵ_{ij} is the total strain and ϵ^0_{ij} is the eigen strain and e_{ij} is the elastic strain.

Specially for thin film ferroelectrics, strain is shown to have a significant effect on the phase stability and domain morphology. Various domain variations can be stabilized by a combination of substrate strain and temperature.

Time-dependent Ginzberg-Landau equation

Once the above thermodynamic energy contributions are included in the total energy expression, the thermodynamic driving force is calculated as the derivative of the total energy of the system with respect to the polarization. The subsequent temporal evolution of the polarization in 3 dimensions is calculated by using the time dependent Ginzberg- Landau equation.

$$\begin{aligned} \frac{\delta \vec{P}}{\delta t} &= -\frac{\delta F}{\delta \vec{P}} + \zeta_i(\vec{r}, t) \\ &= -\frac{\delta F_{bulk} + \delta F_{wall} + \delta F_{elec} + \delta F_{elas}}{\delta \vec{P}} + \zeta_i(\vec{r}, t) \end{aligned} \tag{3.10}$$

Here, $\zeta_i(\vec{r}$,t) is the random force due to thermal fluctuation that has a zero mean and a gaussian variance.

The bulk energy and the domain wall energy are local interactions and hence are candidate for direct parallelization over the distributed processors. The nonlocal interactions on the other hand are difficult to parallelize. The non-local interaction in ferroelectrics arise due to the inhomogeneous electrostatic and elastic field. The computation of these interactions will be described in the Numerical Implementation section.

3.5 Conclusion

In summary, the phase field model is a suitable theoretical formalism for describing dynamics in multi-phase systems. All the thermodynamic energy contributions are included as a functional of the polarization in a ferroelectric. By determining the expansion coefficients and the coupling constants between various order parameters, it is possible to self consistently calculate the polarization and domain wall switching dynamics.

Chapter 4

Massively Parallel Phase Field Simulator

4.1 Introduction

Calculating the multiple component field in a non-periodic structure with arbitrary boundary conditions poses a significant numerical challenge. Massive parallelization is required to be able to provide the memory requirement. Also temporal acceleration is required so that the results can be obtained in reasonable time. In the following section, we describe numerical implementation of the physical equations and performance.

4.2 The Numerical Problem

Real ferroelectric thin films are multi-domain that is they have multiple orientation of polarization domain within the same material. The equilibrium condition for these materials are found by electrostatic and mechanical compatibility among the domains. The numerical difficulty in simulating a thin film ferroelectric device stems from the multiple length scales involved in the problem. Presence of domain walls and electrodes and substrate make the problem non periodic. This means that a micron size film needs to be simulated in order to make direct comparison with experiments. The switching of the domain pattern under an applied field occurs at the micron scale. On the other hand, ferroelectric domain walls are $\sim$1 nm thick. This means that the minimum grid size also have to be $\sim$nm length and the full grid need to span micron scale. Since for a thin film, the height direction can be of 100s of nanometers, a back of the envelop calculation gives an approximate grid size of $1000 \times 1000 \times 100$ that is 10^8 grid points are required to simulate a typical device structure incorporating a multi domain ferroelectric device.

Memory requirement

There are two stiffness matrices associated with the electrostatic and strain calculation. The electrostatic stiffness matrix has the same number of rows as the grid size. Also this matrix is fixed for the entire duration of the simulation that is this matrix is assembled only once. However, the strain stiffness matrix is 6 (3 when excluding shear strain) times the number of grid points. In a finite element grid, with 3D linear brick element, there are 162 (81 when excluding shear strain) elements in each row. With double precision numbers, for a typical grid size of 10^8 mentioned above, this amounts to a $10^8 \times 8 \times 162 = 129{\cdot}6$ GB. This requirement is only for the strain matrix and this matrix needs to be calculated and assembled at every time step. This is way out of the reach of memory available in modern GPUs (typically 6GB). Although it may have been possible to combine GPU banks to aggregate the above memory, but parallel computation on GPU banks is immature and there aren't stable CUDA libraries available for seamless parallelization of a complex scientific software. Hence, we chose to use distributed CPUs for our computational platform and use PETSC as the numerical library to do the parallel processing of all the calculation steps. PETSC provides very flexible interfaces for fixed finite difference calculation. We have extended it to perform finite element on moving grid calculation as well. The main difficulty of combining a finite difference and finite element calculation is the communication required between the two grids. Extreme care is required in designing every step of the implementation to minimize this communication. Reducing the communication and preventing dynamical loading, we have achieved linear scaling of all the calculation steps on thousands of processors.

Temporal requirement

The size of spatial grid size also limits the size of temporal step size. For example using an forward Euler method, the time step size for the Allen-Cahn equation is limited by the relation,

$$\Delta t \sim (\Delta x)^2 \tag{4.1}$$

And for the Cahn-Hillard equation, the temporal step is limited by the relation,

$$\Delta t \sim (\Delta x)^4 \tag{4.2}$$

These requirements stem from the order of the laplacian operator in these equations. Thus a nm scale spatial step in the grid severely limit the normalized time step size. In a typical domain dynamics simulation under applied electric field often $\sim$ 5000 time steps need to be simulated. A single time step in a typical simulation takes about 30 s on an average (a micron size device running on 250 processors). The actual time differ depending on the details of the field variation occurring in a given problem during time evolution. Considering the average time for this problem, the total time for 5000 time steps would be 42 hours. This is a prohibitively long time for investigating switching physics in different device geometries and pursue rational device design. If we can scale the simulation to 5000 processors, then the simulation time goes down by a factor of 20 and bringing the total running time to 2 hours. This amount of scaling allows for quick turn around time for each simulation so that rational device design could be performed using this model. In this thesis, we report the first achievement of linear scaling of the phase field model with inhomogeneous strain to thousands of processors so that the method could be used for materials and device design in direct comparison with experiments.

4.3 Numerical Framework: PETSC

We use the parallel numerical solver PETSC [4] for solving the large systems in parallel. PETSC uses its linear solver KSP, nonlinear solver SNES and the time stepper TS for the respective problem types. Using the built-in function in these numerical libraries, we are solving for the dynamics of each spatial position under the given thermodynamic force. The nonlocal interactions with appropriate boundary conditions as well as the local energies are calculated at each time step. The linear solver KSP is used for solving for the Laplace solution. The time stepper accelerates the thermodynamic variable at each time step. It can also be used as a pseudo time stepper for achieving steady state solutions within shorter computation times. Below we describe various components of the PETSC module.

a. Vectors: The vector is one of the simplest PETSc objects. Vectors are used to store discrete PDE solutions, right-hand sides for linear systems, etc. PETSc has two basic vector types: sequential and parallel (MPI based). To create a parallel vector one can either specify the number of components that will be stored on each process or let PETSc decide. There are significant amount of PETSC defined functions that can be used to initialize, store and manipulate Vectors in sequential or parallel fashion in PETSC.

b. Matrices: PETSc provides a variety of matrix implementations. It supports dense storage and compressed sparse row storage (both sequential and parallel versions), as well as several specialized formats. The use of PETSc matrices involves the following actions: create a particular type of matrix, insert values into it, process the matrix, use the matrix for various computations, and finally destroy the matrix. The application code does not need to know about the particular storage formats of the matrices. The matrices could be either sparse or dense. The variations could be Aij, Blocked Aij, Symmetric blocked Aij etc.

c. Data and Grid: PETSc provides a variety of data structures for managing data and grid management. These are Index Sets, Distributed Arrays, Meshes and Application Orderings etc. Index Sets (IS) objects are used to index into vectors and matrices and to setup vector scatters. Distributed arrays (DAs), which are used in conjunction with PETSc vectors, are intended for use with logically regular rectangular grids when communication of nonlocal data is needed before certain local computations can occur. The unstructured computational mesh (Mesh) component provides an interface for mesh generation, partitioning, refinement, and manipulation. AO (Application Orderings) are objects that manage mappings between different global orderings.

d. Linear Solver, KSP: The main linear solver of PETSC is called KSP that is a short form of Krylov Subspace Method. KSP is intended for solving Ax=b problem. The steps of a KSP operation are as follows: create a KSP object, set the A and preconditioner matrix, initialize the RHS vector, call solver function and destroy the object. During successive linear solves, one could use any of the following 3 flags: same_nonzero_pattern, different_nonzero_pattern, same_preconditioer depending on the problem type at hand.

i) Krylov Methods: We have tested a number of preconditioners in PETSC for our simulation purpose. They are Richardson, Chebychev, Conjugate Gradient, BiConjugate Gradient, Generalized Minimal Residual, BiCGSTAB, Conjugate Gradient Squared, Transpose-Free Quasi-Minimal Residual, Conjugate Residual, Least Squares Method etc. We combined the linear solvers and the preconditioners that are available in the PETSC installation on Hopper.

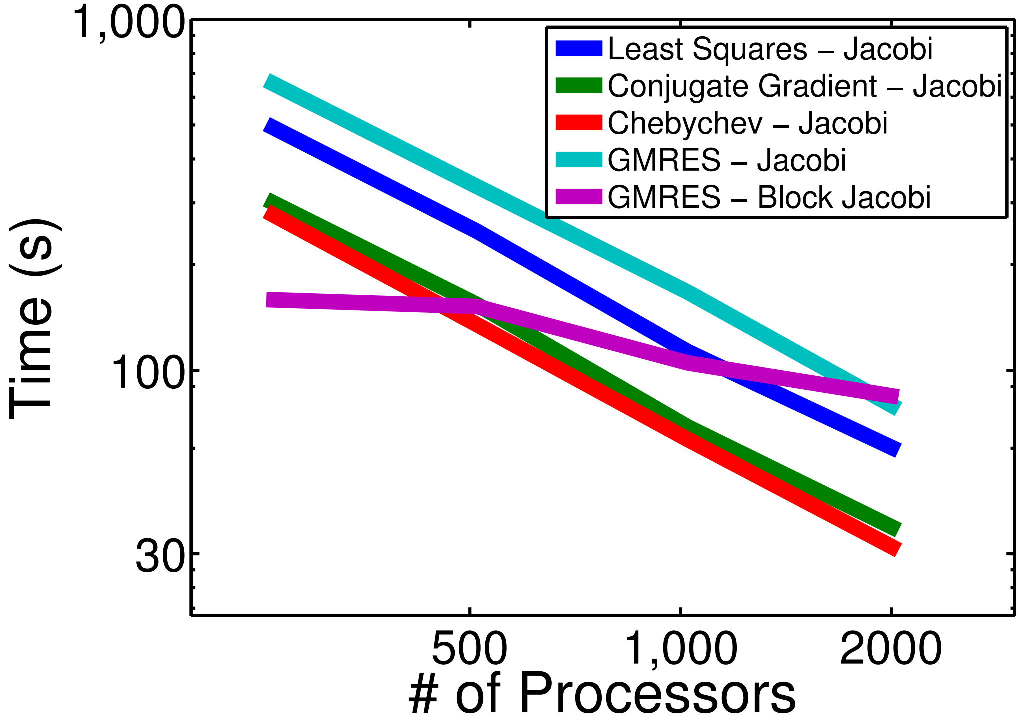

Figure 4.1: Performance of the linear solver, KSP using various solvers and preconditioners. All the simulations presented here are run on the NERSC super-computer Hopper. PETSC is designed to solve large systems, hence, we particularly concentrate on the scaling properties of large systems with close to billion degrees of freedom.

The SNES library of PETSc provides a powerful suite of data structure neutral numerical routines for solving nonlinear problems. Built on top of the linear solvers and data structures, SNES enables the user to easily customize the nonlinear solvers according to the application at hand. Also, the SNES interface is identical for the uniprocess and parallel cases. For our time-dependent Landau-Ginzberg equation, we can calculate steady-state properties, by minimizing the resultant equation. We have used the default finite difference Jacobian supplied by PETSC. The required time for solving the equation as a function of number of processors are shown in the figure above. PETSC provides options for either line search or trust region algorithms for non-linear solver SNES. The PETSC installation on hopper provided options for line search algorithm only. We find that the cubic and the quadratic search gave the ideal scaling performance. The basic search algorithm showed chaotic behavior. The first criterion for achieving better performance with the non-linear solver is to achieve the best possible performance with the linear solver. From the scaling study of the linear solver, we found that for the particular boundary condition, the combination of the Chebychev linear solver with Jacobi preconditioner provided the best performance. Hence we used this solver for the linear solve that runs in the background of the non-linear solver. PETSC provides built-in functions that can be used to access and set the linear solvers and the preconditions used by the data structures that are used by the non-linear interface. In brief, using a Line Search algorithm with either cubic or quadratic search algorithm with Chebychev solver and Jacobi preconditioner provided the best scaling result for our specific problem.

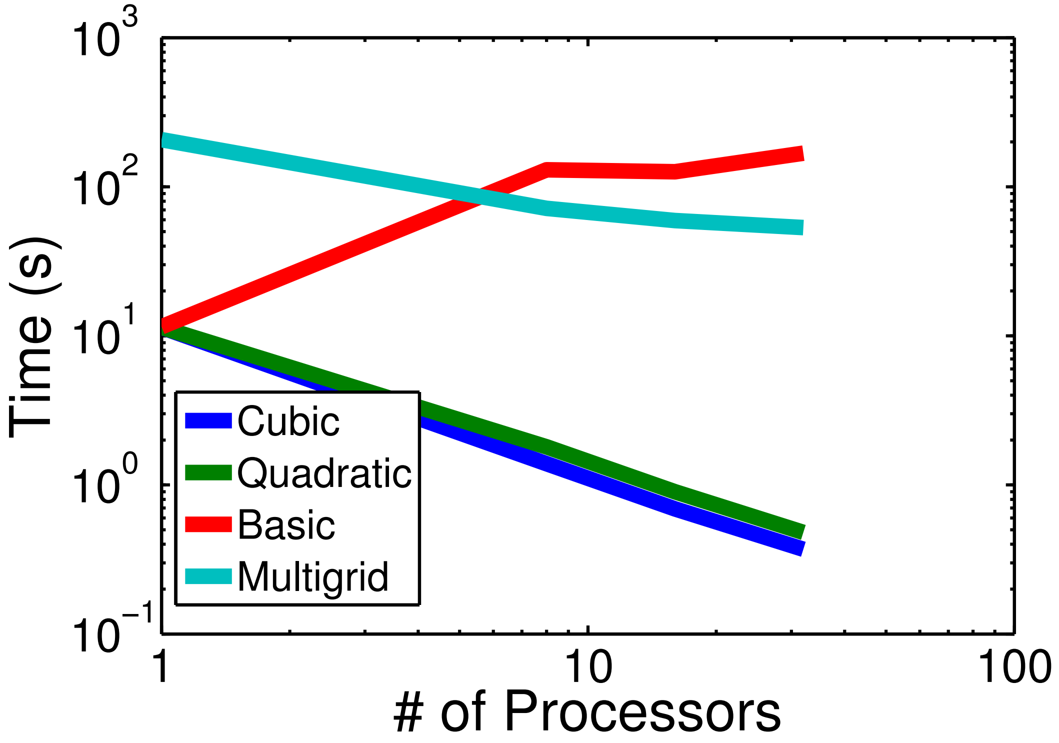

Figure 4.2: Performance of the non-linear solver using the Line Search method. 3 search methods: cubic, quadratic and basic are used.

f. Multigrid: PETSC has a high-level interface for multigrid on a single structured grid using the PETSC DA object to decompose the grid across the processors. The main steps of setting up the DMMG solver are: Create a DMMG object, assign a distributed array (DA) object with the DMMG object, assign the linear solver context (the associated A matrices and the preconditioner matrices will be automatically created according to the DA object), initialize the RHS vector and call the solver function. It is also possible to use multi-grid for non-linear solutions as well using SNES in a similar fashion. Here, we show the scaling properties of the linear solve using the DMMG solver. We used two different RHS for the performance evaluation. In one case we initialized the RHS with a constant value and in the other case with a random value. Since PETSC uses the iterative linear solver making use of the Krylov method, the solution time for random RHS is significantly higher than the constant RHS. From the profiling information we find that the number of PC Apply step increases significantly for random RHS. However, the scaling of both the random and the constant RHS showed perfect scaling.

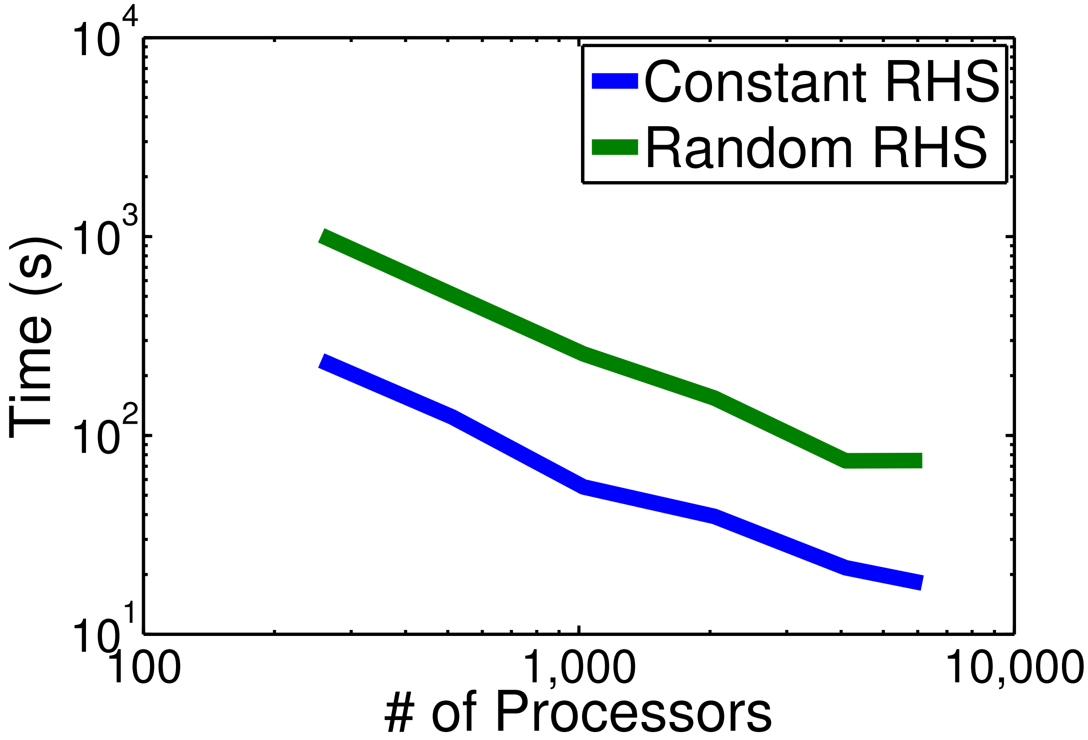

Figure 4.3: Performance of the DMMG linear solver. Two different RHS are used for the same size grid, one constant and the other random. The random RHS takes significantly higher time for convergence.

In the DMMG solver, it is possible to specify the number of levels between the coarse and the finest grid. As an illustration purpose, we show the results for single and three level multi-grids for linear solves. We find that while the single level multigrid showed perfect scaling, the three level multi-grid showed chaotic behavior.

Table 4.1: Profile of a PETSC KSP simulation.

	Max/Min	Avg	Total
Time (sec)	1.828e+01	1.00024	1.828e+01
Objects	1.080e+02	1.00000	1.080e+02
Flops	1.05233e9	2.052e+09	1.260e+13
Flops/sec	1.05236e8	1.122e+08	6.896e+11
Memory	1.052e+07	1.05993	6.259e+10
MPI Messages	2.00000 e7	1.563e+04	9.601e+07
MPI Message Lengths	7.258e+07	3.981e+03	3.822e+11
MPI Reductions	1.723e+04	1.00000	

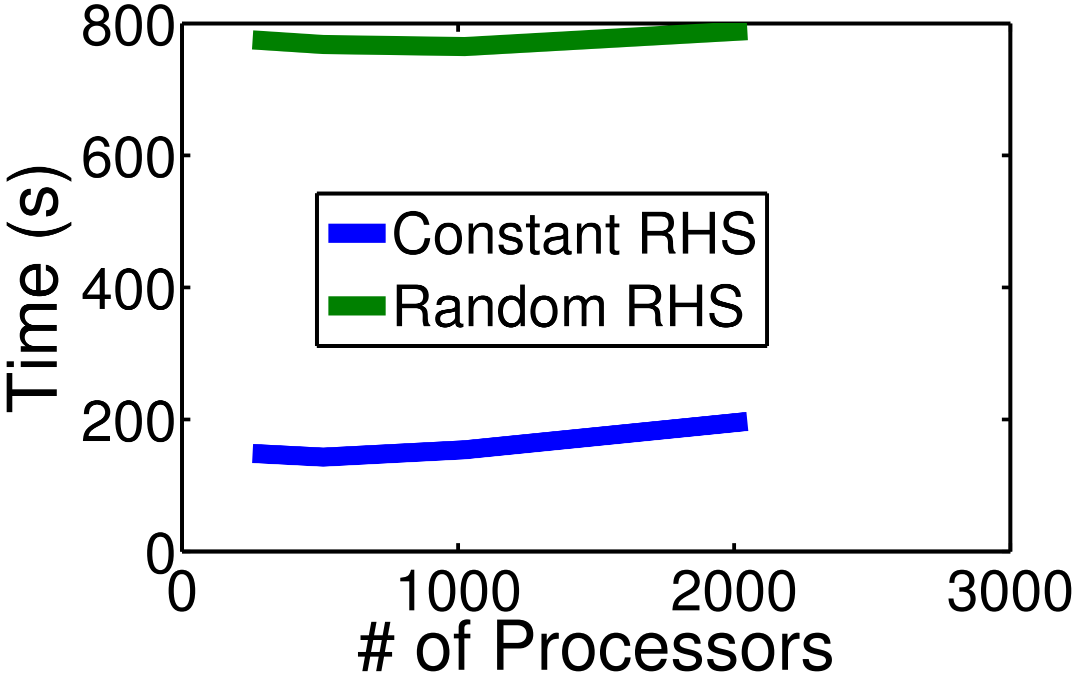

Figure 4.4: Scaling properties of the linear solver using the multigrid interface of PETSc with three levels between coarse and finest grid.

We also tested the DMMG interface of PETSc for minimizing the RHS of the phase field equation. Here, we have used three levels of refinement between the coarsest and finest grid. Cubic line search was used for minimzing the equation. In this case, the DMMG interface of the non-linear solver scales perfectly with increasing number of processors.

g. Profiling: A representative performance profiling information is shown below.

The profiler provides information at multiple levels. The profile shown above provides top level performance information. However, one can also get performance and message passing information at different levels of the code execution. For example in an inhomogeneous laplacian solution using the DMMG interface will provide information about the performance of the code at the linear solve, non-linear solve and also during different grid refinements. Thus one can easily find out where performance is dropping and take appropriate measures to enhance performance.

4.4 Numerical Implementation

We have implemented a time domain phase field model contrary to that described in[10]. In general, the semi-implicit fourier-spectral method allows one to take significantly longer time steps compared to a Forward-Euler method [10]. However, we employed a velocity verlet method that allowed us to take time steps significantly longer than the Forward-Euler method and reproduce the results predicted by the semi-implicit method [10]. Our specific motivation for pursuing a time domain implementation is to take advantage of modern distributed computing architectures. We will show below that problem sizes of N=10^9 can be modeled very efficiently with a time domain implementation exploiting the parallelization achieved at every computation steps. This is a significant step forward in terms of numerical capability compared to the state of the art phase-field modeling. Also, a time domain approach allows for easy and intuitive incorporation of electrostatic and mechanical boundary conditions and therefore predictive simulation of dynamic behavior can be performed. In our model, the simulation grid consists of FEM and FD grid for elastic and electrostatic calculations respectively. Below we describe the various aspects of the numerical implementation.

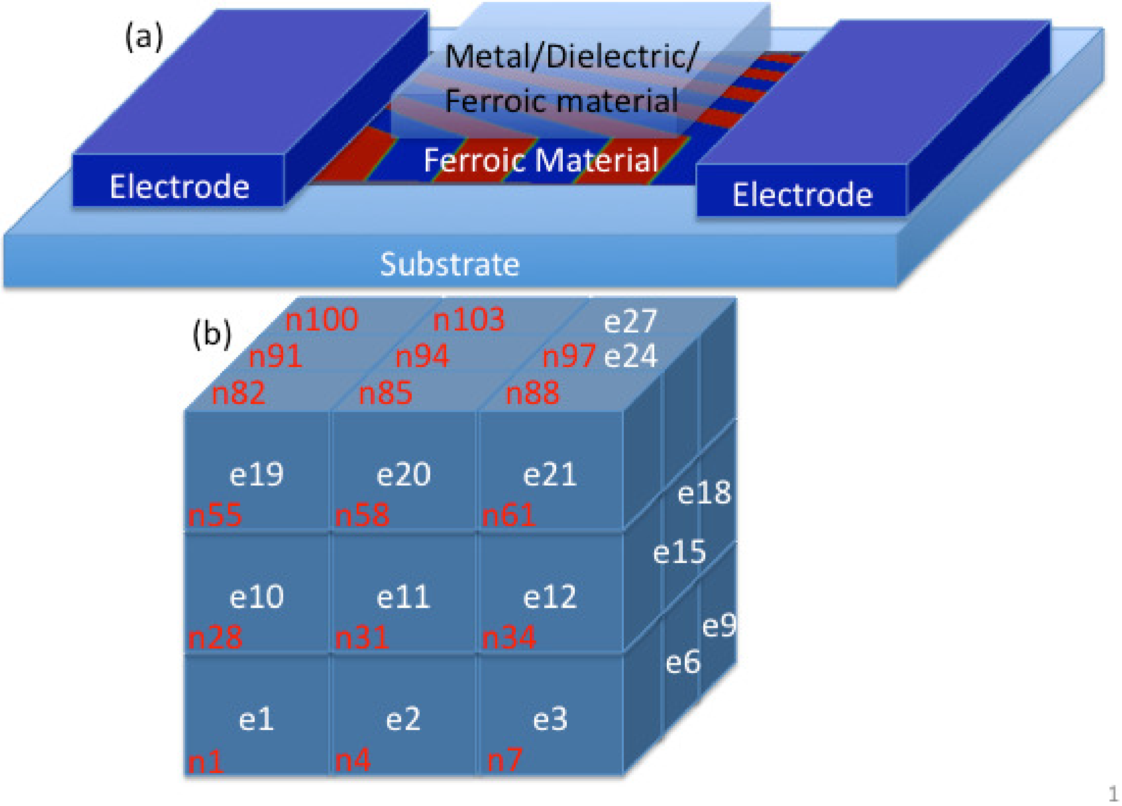

Figure 4.5: (a) Schematic of a representative device structure that is used as a test case for the developed method. Here, a thin film of ferroelectric material is grown on a substrate. Two electrodes are placed in order to apply an in-plane electric field. The electrostatic boundary condition on the material can be changed by using different materials on the ferroic thin film. The substrate strain can be varied by changing the substrate material with different lattice vectors. (b) The implemented numerical grid that contains both finite difference and finite element grids. The elements are a small block of linear brick element. The nodes of the block coincide with the FD grid. Both FEM and the FD grids are numbered in natural ordering.

Grid

We used a mixed grid for implementing the electrostatic and elastic interactions. The elastic interaction calculation is done on a FEM grid and the electrostatic calculation is performed on a FD grid. The relationship between the FEM element and FD node numbering are shown in Fig. 4.5(b). Initially, polarizations are defined on a 3D FD grid. The bulk energy and domain wall energy are calculated on this grid. The nonlocal electrostatic field is calculated by solving the Poisson equation on the FD grid. The matrix was parallelized for a 3D FD stencil, so that maximum of the connected grid points are on the same processor. This way of parallelizing the FD stiffness matrix provides very fast matrix assembly performance and is implemented in the DA data structure of PETSC[3]. The spontaneous strain at every node is calculated from the polarizations [see equation 16, to be discussed later]. The body force due to the spontaneous strain is assigned at the nodes of the FEM grid element nodes. A finite element grid with linear brick element is then used to solve for the stress-strain relationship. Once the total strain is calculated by solving the stress-strain relation with FEM, it is assigned in a reverse manner to the respective FD node points. The change in free energy is calculated due to the strain and hence the thermodynamic force due to the elastic energy. A natural coordinate numbering was employed for the FEM calculation. For a 3D brick element, each body node has 8 elements connected to it and hence has a total of 26 element nearest neighbor nodes. Due to a significantly increased nearest neighbor in the FEM grid, compared to the FD grid, we parallelized the stiffness matrix in the natural coordinate numbering order. Special care was taken for minimizing nonlocal assignments to the stiffness matrix when assembling, as will be described in the FEM calculation section. Thus parallelizing the two grids in two different manners facilitates maximum efficiency for the respective problems.

The overall simulator in block diagram form is shown below. In this process, we calculate the thermodynamic force on the polarization due to different local and non-local interactions. The local interactions are the bulk force and the domain wall force. The non-local interactions are dipole-dipole and strain driven interactions. The initial grid defined is a finite difference grid on which the local interactions are directly calculated. This is an embarrassingly parallel problem meaning the calculations in all the independent processors are completely independent and hence can be readily parallelized to arbitrary number of processors. The electrostatic problem is also solved on a finite difference grid. PETSC provides a library for automatic parallelization of finite difference grids that is well optimized. Hence using the PETSC library it is possible to easily parallelize the electrostatic problem as well, although this is not an embarrassingly parallel problem. The difficulty arises when calculating the strain interaction. The finite difference formulation of non-linear strain problems are significantly difficult and limited in applicability when it comes to arbitrary boundary conditions. On the other hand finite element is well suited for nonlinear strain calculation with arbitrary boundary condition, but the parallelization of finite element is significantly difficult due to the increased nearest neighbor connectivity of a 3D element and the communication that is required between the finite difference and the finite element grids. In the following, we will describe a number of mathematical and algorithmic designs to accelerate this process and achieve linear scaling at thousands of processors.

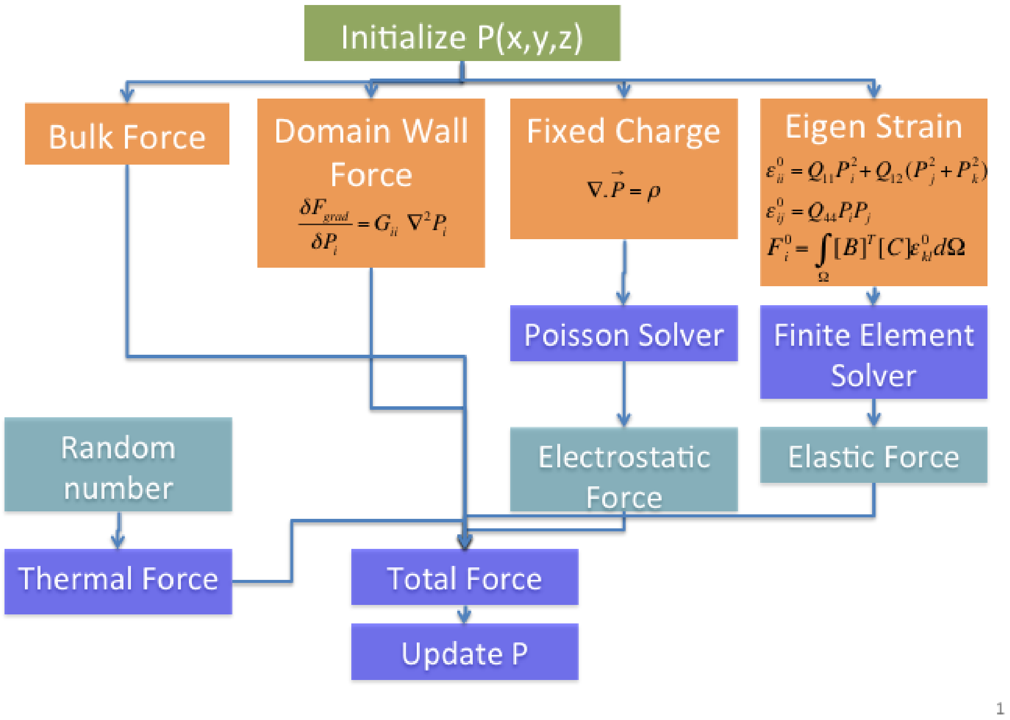

Figure 4.6: (a) The block diagram of the phase field simulator.

Bulk force

A polarization distribution is initialized at each point of the grid. The bulk energy at each point on the grid is given by the Landau equation:

$$\begin{aligned} E_{bulk} &= \alpha_1(P_x^2 + P_y^2 + P_z^2) + \alpha_{11}(P_x^4 + P_y^4 + P_z^4) \\ &+\alpha_{12}(P_x^2 P_y^2 + P_y^2 P_z^2 + P_z^2 P_x^2) \end{aligned} \tag{4.3}$$

The corresponding force on each point is calculated by taking the derivative with respect to the polarization. For example, the three components of the force from the above energy profile is

$$\begin{aligned} Fx_{bulk} &= 2\alpha_1 P_x + 4\alpha_{11} P_x^3 + 2\alpha_{12} P_x (P_y^2 + P_z^2) \\ Fy_{bulk} &= 2\alpha_1 P_y + 4\alpha_{11} P_y^3 + 2\alpha_{12} P_y (P_x^2 + P_z^2) \\ Fz_{bulk} &= 2\alpha_1 P_z + 4\alpha_{11} P_z^3 + 2\alpha_{12} P_z (P_x^2 + P_y^2) \end{aligned} \tag{4.4}$$

Numerically we define three global vectors corresponding to polarizations on a finite difference DA, P$_i$ and three global vectors corresponding to bulk force Fi$_b ulk$. These vectors can be parallelized in normal ordering or finite difference DA grid. The two methods of parallelization differ by the nearest neighbor of the 3D grid. Although, the natural ordering is intuitive and useful for the calculation of the bulk force, the DA ordering is useful for finite difference calculation. The partitioner for FD calculation rearranges the grid numbering in a way so that the grid point connections at the processor to processor boundaries are minimized. We chose to use the DA ordering for convenience with the domain wall and electrostatics calculation later. The two types of ordering are illustrated by the following figure.

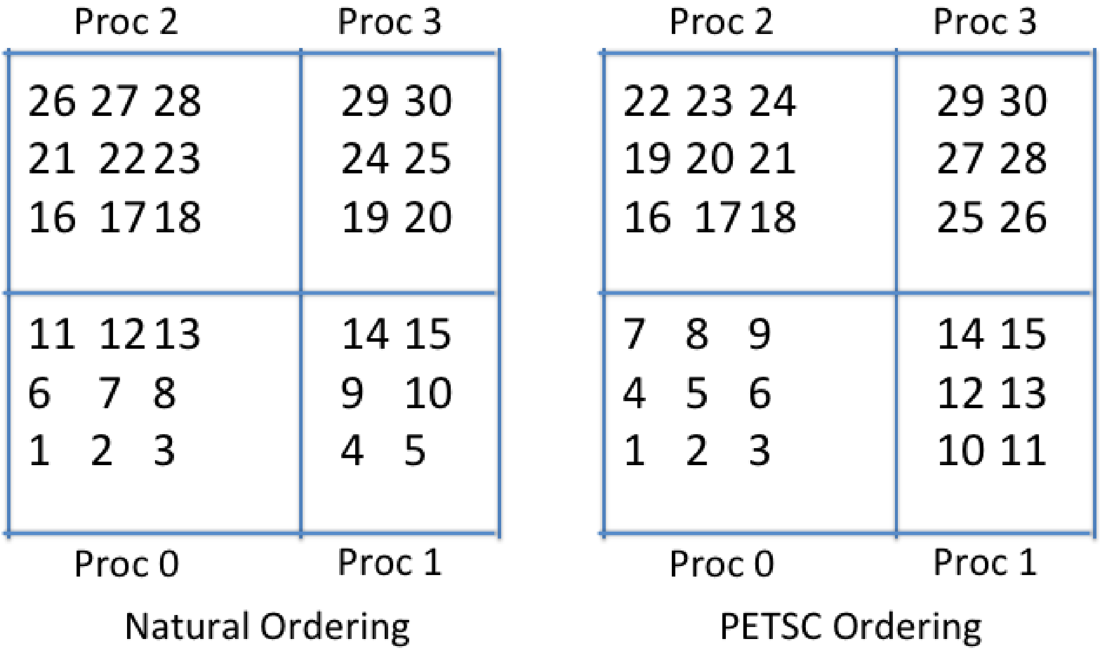

Figure 4.7: Two grid partition schemes used in PETSC.

Judicial grid ordering for avoiding communication is a major tool for achieving performance in solving complex numerical problems. The running time of an algorithm is the sum of time for floating point operation, time for moving words and the latency of message passing. The required time of each of these operations increase from floating point operation to message passing in large distributed systems. The necessary way to achieve parallel performance in massively parallel problems is to reduce communication between all memory hierarchy levels.

Since, the choice of data structures for a particular problem is of prime importance, we provide example codes in order to explain the flow of our software. In order to use a DA grid, we first create the grid using the PETSC function,

```
DACreate3d(PETSC_COMM_WORLD,DA_YPERIODIC,
          DA_STENCIL_BOX,appctx.l,appctx.m,appctx.n,PETSC_DECIDE,
             PETSC_DECIDE,PETSC_DECIDE,1,1,PETSC_NULL,
```

```
                  PETSC_NULL,PETSC_NULL,&appctx.da);
```

Then we create the global vectors associated with this grid using the function,

```
DACreateGlobalVector(appctx.da,&Px);
```

The main principle for achieving parallel performance with PETSC is that we cannot use any serial assignment in the vectors and the matrices. All the assignments must be parallel and local to individual processor. In order to assign values in parallel to the global vector Px, we first find out the nodes of the grid owned by the current processor and run a loop through the local grid points to assign values to the vector.

The global size and local node numbers are obtained by,

```
 DAGetInfo(appctx->da,0,&mx,&my,&mz,0,0,0,0,0,0,0);
 DAGetCorners(appctx->da,&xs,&ys,&zs,&xm,&ym,&zm);
```

Here, mx, my, mz are the global grid size. xs, ys, zs are the local starting point of the global grid number. xm, ym, zm are the end of the global node numbers owned by the local processor. Information about the start and end point of the global node numbers owned by the local processor allows for easy traversal of the grid using for loops.

The vectors can only store data. They cannot be used to assign values locally. In order to assign value to the global vector, we have to extract local arrays from the global vector. This is done in multiple steps. First a local vector is created associated with the DA. Then a global to local scatter is performed. Finally, the data from the local vector is copied to an array. The data can now be modified in the local array. The following code accomplishes this task.

```
 DAGetLocalVector(appctx->da,&Px_local);
 DAGlobalToLocalBegin(appctx->da,Px,INSERT_VALUES,Px_local);
 DAGlobalToLocalEnd(appctx->da,Px,INSERT_VALUES,Px_local);
 DAVecGetArray(appctx->da,Px_local,&Px_localptr);
```

Similar global to local mapping and array extraction is performed for other components. The local grid is now traversed to initialize the polarization values.

```
 for (k=zs; k<zs+zm; k++) {
  for (j=ys; j<ys+ym; j++) {
  for (i=xs; i<xs+xm; i++) {
if (the criterion for initialization){
    Px_localptr[k][j][i] = Px_init;
//similarly for other components}
}}}
```

The values assigned in the local arrays are now stored back to the global vector using,

```
 DAVecRestoreArray(appctx->da,Px,&Px_localptr);
//similarly for other components
```

A random value can also be assigned to initialize the polarizations by first creating a random number generator object, setting the interval within which the numbers should be generated and assigning this value to the polarizations. After the assignment, the object should be destroyed.

```
PetscRandomCreate(PETSC_COMM_WORLD,&pRandom);
    PetscRandomSetFromOptions(pRandom);
    PetscRandomSetType(pRandom,PETSCRAND);
    PetscRandomSetInterval(pRandom,.1e-0,1e-0);
    VecSetRandom(Px,pRandom);
    //similarly for y and z components
    PetscRandomDestroy(pRandom);
```

Once the polarizations are assigned, the corresponding bulk forces can be calculated in parallel in a similar way to the assignment of the polarization using the expression,

$$Fx_{bulk}[i] = -2\alpha_1 P_x[i] - 4\alpha_{11}P_x^3[i] - 2\alpha_{12}P_x[i](P_y[i]^2 + P_z[i]^2) \tag{4.5}$$

One specific example is shown here.

```
Fxbulk[k][j][i]
              = -2*appctx->a1S*Px_localptr[k][j][i]
                 -4*appctx->a11S*pow(Px_localptr[k][j][i],3)
                -2*1*appctx->a12S*Px_localptr[k][j][i]
               *(pow(Py_localptr[k][j][i],2)
               +pow(Pz_localptr[k][j][i],2));
//similarly for other components
```

Domain Wall Force

The domain wall energy is calculated by the gradient of the polarization on the nearest neighbor grid points.

$$\begin{aligned} E_{grad} =& G_{11}(P^{'}_{X,X} + P^{'}_{X,Y} + P^{'}_{X,Z} + P^{'}_{Y,X} \\ &+ P^{'}_{Y,Y} + P^{'}_{Y,Z} + P^{'}_{Z,X} + P^{'}_{Z,Y} + P^{'}_{Z,Z}) \end{aligned} \tag{4.6}$$

Here, $P^{'}_{I,I}$ are the gradient of polarization along the grid directions. G_{11} is the domain wall energy coefficient when the grid and crystal directions coincide. P_I is the projection of the polarization along the grid direction I.

The domain wall force component along a specific direction is calculated by taking the derivative of the domain wall energy with respect to the polarization along that direction.

$$Fx_{wall} = -\frac{\delta E_{grad}}{\delta P_x} = -G_{11}\nabla^2 P_x \tag{4.7}$$

The code snippet implementing the domain wall force is shown here. Note here that although we need to access nearest neighbor points for domain wall energy calculation and these neighbor points could reside in other processors, the boundary points are ghosted in PETSC. This means that the boundary points can be accessed locally in the DA structure and the finite difference stencil appears as local for all the grid points.

```
 Fx_wall[k][j][i]= - (appctx->G11*(
Px_lptr[k][j][i-1]-2*Px_lptr[k][j][i]+Px_lptr[k][j][i+1]+
Px_lptr[k][j-1][i]-2*Px_lptr[k][j][i]+Px_lptr[k][j+1][i]+
Px_lptr[k-1][j][i]-2*Px_lptr[k][j][i]+Px_lptr[k+1][j][i]));
```

Electrostatic Force

Electric field due to the inhomogeneous polarization and the applied field incorporating the appropriate boundary condition is calculated on the FD grid. The charge density resulting from the inhomogeneous polarization are calculated using

$$\rho = \nabla \cdot P \tag{4.8}$$

The parallel version of the charge calculation is performed by first extracting a local copy of the charge array and then calculating the component charges as

```
Cx=-(Px_localptr[k][j][i+1]-Px_localptr[k][j][i]);
Cy=-(Py_localptr[k][j+1][i]-Py_localptr[k][j][i]);
Cz=-(Pz_localptr[k+1][j][i]-Pz_localptr[k][j][i]);
 Cu_localptr[k][j][i]=((Cx+Cy+Cz)*appctx->Ps/appctx->eps_p));
```

Here, Ps is the saturation polarization of the ferroelectric. Once the total charge is calculated, the array is restored into the global charge vector.

The poisson equation is given by

$$\nabla \cdot \epsilon \nabla \phi = \rho \tag{4.9}$$

Here, ϵ is the dielectric constant, ϕ is the potential ρ is the charge density. The poisson equation is discretized with a 7 point stencil on a finite difference grid. The discretized version looks like

$$\begin{aligned}\epsilon(i,j,k)\times \quad & \tfrac{\phi(i+1,j,k)+\phi(i-1,j,k)-2\phi(i,j,k)}{h_x^2} + \tfrac{\phi(i,j+1,k)+\phi(i,j-1,k)-2\phi(i,j,k)}{h_y^2} \\ & + \tfrac{\phi(i,j,k+1)+\phi(i,j,k-1)-2\phi(i,j,k)}{h_z^2} = \rho(i,j,k)\end{aligned} \tag{4.10}$$

Stiffness Matrix and the boundary conditions

Some of the useful boundary conditions are periodic, Dirichlet, Neumann and inhomogeneous material interface. The applied field is incorporated by assigning a predefined voltage where the electrodes are placed. Different boundary conditions can be easily applied when assembling the laplacian operator in 3D. The floating boundary or the Neumann boundary condition is applied on open surfaces by setting the normal component of the electric field to zero.

For finite difference stiffness matrix construction, PETSC provides a MatStencil data structure that helps in assembling the matrix in parallel. The primary advantage is that PETSC saves the 7 stencil nearest neighbor grid points as ghost points in order to avoid nonlocal assignment. For example, in the body of a homogeneous material, the boundary condition is set as,

```
v[0] = -eps;col[0].i = i; col[0].j = j; col[0].k = k-1;
v[1] = -eps;col[1].i = i; col[1].j = j-1; col[1].k = k;
v[2] = -eps;col[2].i = i-1; col[2].j = j; col[2].k = k;
v[3] = 2.0*eps*3;col[3].i = row.i; col[3].j = row.j;
        col[3].k = row.k;
v[4] = -eps;col[4].i = i+1; col[4].j = j; col[4].k = k;
v[5] = -eps;col[5].i = i; col[5].j = j+1; col[5].k = k;
v[6] = -eps;col[6].i = i; col[6].j = j; col[6].k = k+1;
ierr = MatSetValuesStencil(B,1,&row,7,col,v,INSERT_VALUES);
```

Here, eps is the relative dielectric constant. Another advantage of using the PETSC provided interface is that, we do not need to keep track of the global indices of the nearest neighbor, they are internally handled by the PETSC routine.

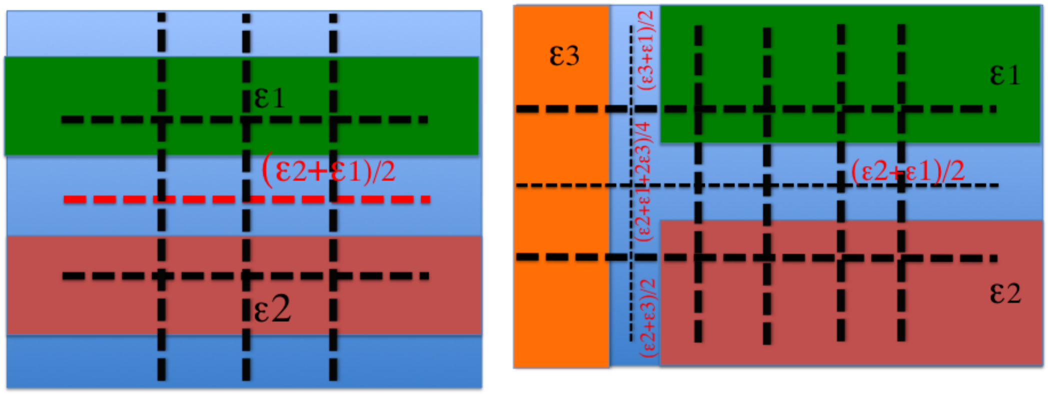

2 materials interface 3 materials interface

Figure 4.8: Interface between two or three different materials. The intermediate nodes are assigned average values of their neighboring nodes.

We implemented the inhomogeneous material boundary by assigning average dielectric constant for the grid points at the interface as shown below.

```
v[0] = -eps2;col[0].i = i; col[0].j = j; col[0].k = k-1;
v[1] = -((eps1+eps2)/2);col[1].i = i; col[1].j = j-1; col[1].k = k;
```

```
v[2] = -((eps1+eps2)/2);col[2].i = i-1; col[2].j = j; col[2].k = k;
v[3] = (eps1+eps2)3;col[3].i = row.i; col[3].j = row.j;
          col[3].k = row.k;
v[4] = -((eps1+eps2)/2);col[4].i = i+1; col[4].j = j; col[4].k = k;
v[5] = -((eps1+eps2)/2);col[5].i = i; col[5].j = j+1; col[5].k = k;
v[6] = -eps1;col[6].i = i; col[6].j = j; col[6].k = k+1;
MatSetValuesStencil(B,1,&row,7,col,v,INSERT_VALUES);
```

Here, eps1 and eps2 are relative the dielectric constants of the two materials that have an interface in the XY plane.

The Neumann or floating boundary condition is implemented by equating the potential at the last two grid points.

```
v[3] = -eps;col[3].i = i-1; col[3].j = j; col[3].k = k;
v[4] = -eps;col[4].i = i; col[4].j = j-1; col[4].k = k;
v[5] = -2*eps;col[5].i = i; col[5].j = j; col[5].k = k-1;
v[2] = 2.0*eps*3;col[2].i = row.i; col[2].j = row.j;
          col[2].k = row.k;
v[0] = -eps2;col[0].i = i+1; col[0].j = j; col[0].k = k;
v[1] = -eps2;col[1].i = i; col[1].j = j+1; col[1].k = k;
 MatSetValuesStencil(B,1,&row,6,col,v,INSERT_VALUES);
```

The dirichlet boundary condition is applied by assigning a value of 1 to the appropriate grid point and initializing the node voltage on the charge vector on the right hand side.

```
 v[0] = -1;col[0].i = i; col[0].j = j; col[0].k = k;
 MatSetValuesStencil(B,1,&row,1,col,v,INSERT_VALUES);
```

Once the stiffness matrix is crated and stored, the right hand side vector is initialized and stored, the system of linear equations is solved by using the multigrid method. Here, we have used the DMMG data structure of PETSC. First a DMMG is created and associated with the existing DA using the following code.

```
 ierr = DMMGCreate(PETSC_COMM_WORLD,1,PETSC_NULL,&dmmg);
 ierr = DMMGSetDM(dmmg,(DM)appctx.da);
```

Once the DMMG is created, KSP solver is created and assigned to the DMMG. The name of the function that contains the formation of the stiffness matrix A and the file that contains the right side vector rho are supplied as arguments.

```
    DMMGSetKSP(dmmg,ComputeRHS,formMatA);
    ksp=DMMGGetKSP(dmmg);
    KSPSetInitialGuessNonzero(ksp,PETSC_TRUE);
```

The third line here notifies PETSC to use the solution of the last iteration as the initial guess for the next step in the case of a temporal evolution calculation. Setting the initial condition to nonzero significantly improves performance.

Once the matrices are formed and the solver object is created, the charge is calculated from the polarization distribution and a DMMG solve is performed to get the potential.

```
calcCharge(u,v,w,appctx.C_u,&appctx);
DMMGSolve(dmmg);CHKERRQ(ierr);
VecCopy(DMMGGetx(dmmg),appctx.potential);
```

Finally, the potential vector from the DMMG data structure is copied to the global potential vector, so that it can be accessed from other parts of the code.

4.5 Finite Element Calculation

The FEM calculation involves 1) calculating the element stiffness matrices, 2) assembling the structure stiffness matrix, 3) applying mechanical boundary conditions, 4) calculating the body forces originating from plastic strain and solve for the total strain. First we briefly review the finite element method and describe the FEM calculation implemented in our code.

For a 2D plane stress-strain problem, the relation between strain and stress is given by

$$\begin{pmatrix} \sigma_x \\ \sigma_y \\ \gamma_{xy} \end{pmatrix} = \frac{E}{(1-\nu^2)} \begin{pmatrix} 1 & \nu & 0 \\ \nu & 1 & 0 \\ 0 & 0 & \frac{1-\nu}{2} \end{pmatrix} \times \begin{pmatrix} \epsilon_x \\ \epsilon_y \\ \epsilon_x y \end{pmatrix} + \begin{pmatrix} \sigma_x^0 \\ \sigma_y^0 \\ \gamma_{xy}^0 \end{pmatrix} \tag{4.11}$$

This equation can be written in a compact form as

$$\sigma = E\epsilon + \sigma^0 \tag{4.12}$$

Here, E is the elastic constant, ν is the poisson ratio and σ^0 is the internal stress due to thermal expansion, gravity etc. In the finite element method, a structure is first divided into smaller elements. A relation between strain and displacement is formulated in order to use the stress-strain relation to find out the spatial deformation of the element. For example, in the figure below, we can define the displacements of the element under stress as a function of x and y coordinates. Thus, the displacements u=u(x,y) and v=v(x,y). For infinitesimal displacement, we can define the strain as

$$\begin{aligned} \epsilon_x &= \frac{\delta u}{\delta x} \\ \epsilon_y &= \frac{\delta v}{\delta y} \\ \gamma_{xy} &= \frac{\delta u}{\delta y} + \frac{\delta v}{\delta x} \end{aligned} \tag{4.13}$$

This equation can be written in matrix form as

$$\begin{pmatrix} \epsilon_x \\ \epsilon_y \\ \epsilon_{xy} \end{pmatrix} = \begin{pmatrix} \frac{\delta}{\delta x} & 0 \\ 0 & \frac{\delta}{\delta y} \\ \frac{\delta}{\delta y} & \frac{\delta}{\delta x} \end{pmatrix} \times \begin{pmatrix} u \\ v \end{pmatrix} \tag{4.14}$$

or

$$\epsilon = \delta u \tag{4.15}$$

Now the displacement in the material points can be discretized by writing the displacement only at the nodal points and using a shape function to find the displacement at any other point in the material. For example, for a 2 node element, the displacement can be written as

$$\begin{pmatrix} u \\ v \end{pmatrix} = \begin{pmatrix} N_1 & 0 & N_2 & 0 \\ 0 & N_1 & 0 & N_2 \end{pmatrix} \times \begin{pmatrix} u_1 \\ v_1 \\ u_2 \\ v_2 \end{pmatrix} \tag{4.16}$$

or

$$\begin{aligned} u &= Nd \\ => \epsilon &= \delta N d = Bd \end{aligned} \tag{4.17}$$

Matrix B is called the strain-displacement matrix. Now, the strain energy per unit volume is given by,

$$\begin{aligned} U = & \tfrac{1}{2} \textstyle\int \epsilon^T E \epsilon dV \\ = & \tfrac{1}{2} d^T \textstyle\int B^T E B d dV \\ = & \tfrac{1}{2} d^T K d \end{aligned} \tag{4.18}$$

Here, K is called the element stiffness matrix. From this definition,

$$K = \int B^T E B dV \tag{4.19}$$

Now the shape functions can be linear or higher order depending on the problem at hand. The problem with this type of element stiffness matrix is that we have to perform an integral over the whole volume of the element. For very large number of elements, this process of element matrix calculation becomes almost impossible. Also the construction of shape functions that satisfy consistency requirements for higher order elements with curved boundaries becomes increasingly complicated. These difficulties can be overcome by implementing an isoparametric element.

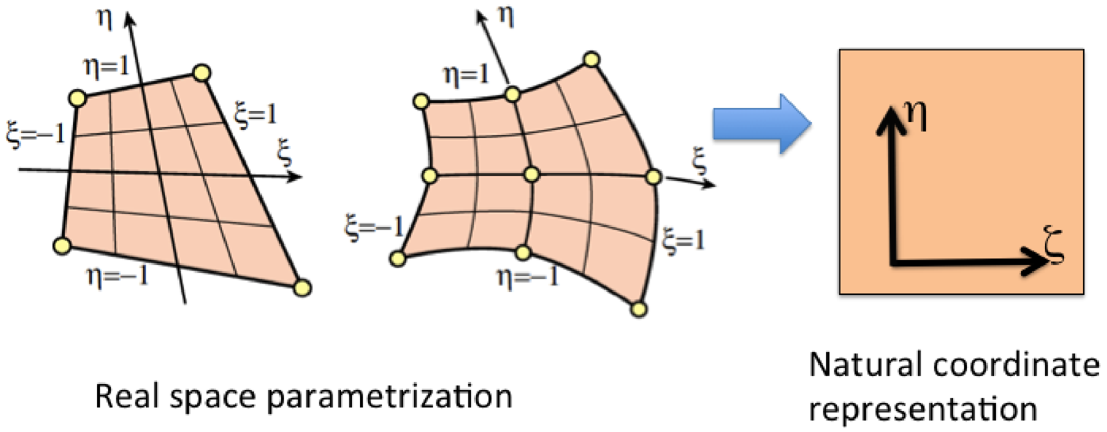

Figure 4.9: The deformed grids are parametrized using the shape function and projected on to the shape function basis (natural grid) where any element appears as a regular element.

Element Stiffness Matrix

Initially, we calculated the elements using the full integration. However, this process turned out to be prohibitive for large degrees of freedom. Then we used an iso-parametric linear brick element for implementing the FEM calculation of the inhomogeneous strain. An iso-parametric implementation of the elements allows for Gaussian Integration during element stiffness calculation and thus facilitates faster assembly. The main idea behind isoparametric elements is that the shape function can be used to define both the geometry and displacement within a material. For example, the geometry for a quadrilateral element can be defined using the equation,

$$\begin{pmatrix} 1 \\ x \\ y \end{pmatrix} = \begin{pmatrix} 1 & 1 & 1 & 1 \\ x_1 & x_2 & x_3 & x_4 \\ y_1 & y_2 & y_3 & y_4 \end{pmatrix} \times \begin{pmatrix} \zeta_1 \\ \zeta_2 \\ \zeta_3 \\ \zeta_4 \end{pmatrix} \tag{4.20}$$

The displacement can also be written in the natural coordinate as

$$\begin{aligned} u &= u_1 N_1^e + u_2 N_2^e + u_3 N_3^e + u_4 N_4^e \\ v = v_1 N_1^e + v_2 N_2^e + v_3 N_3^e + v_4 N_4^e &= v_1 \zeta_1^e + v_2 \zeta_2^e + v_3 \zeta_3^e + v_4 \zeta_4^e \end{aligned} \tag{4.21}$$

Now the shape functions can be written in natural coordinate as

$$\begin{aligned}
N_1^e &= \frac{1}{4}(1-\zeta)(1-\eta) \\
N_2^e &= \frac{1}{4}(1+\zeta)(1-\eta) \\
N_3^e &= \frac{1}{4}(1+\zeta)(1+\eta) \\
N_4^e &= \frac{1}{4}(1-\zeta)(1+\eta) \qquad (4.22)
\end{aligned}$$

Thus the constitutive equations for the isoparametric elements are

$$\begin{aligned}
1 = \sum N_i^e, x &= \sum x_i N_i^e, y = \sum y_i N_i^e \\
u &= \sum u_i N_i^e, v = \sum v_i N_i^e \qquad (4.23)
\end{aligned}$$

Here, we describe the process of calculating the stiffness matrix of a 3D linear brick element using the isoparametric elements. Our goal is to write the equation (4.17) using the shape function defined on the natural coordinate. The iso-parametric element is written in natural coordinates.

$$\begin{aligned}
N_1^e &= \frac{1}{8}(1-\zeta)(1-\beta)(1-\eta) \\
N_2^e &= \frac{1}{8}(1-\zeta)(1-\beta)(1+\eta) \\
N_3^e &= \frac{1}{8}(1-\zeta)(1+\beta)(1+\eta) \\
N_4^e &= \frac{1}{8}(1-\zeta)(1+\beta)(1-\eta) \\
N_5^e &= \frac{1}{8}(1+\zeta)(1-\beta)(1-\eta) \\
N_6^e &= \frac{1}{8}(1+\zeta)(1-\beta)(1+\eta) \\
N_7^e &= \frac{1}{8}(1+\zeta)(1+\beta)(1+\eta) \\
N_8^e &= \frac{1}{8}(1+\zeta)(1+\beta)(1-\eta) \qquad (4.24)
\end{aligned}$$

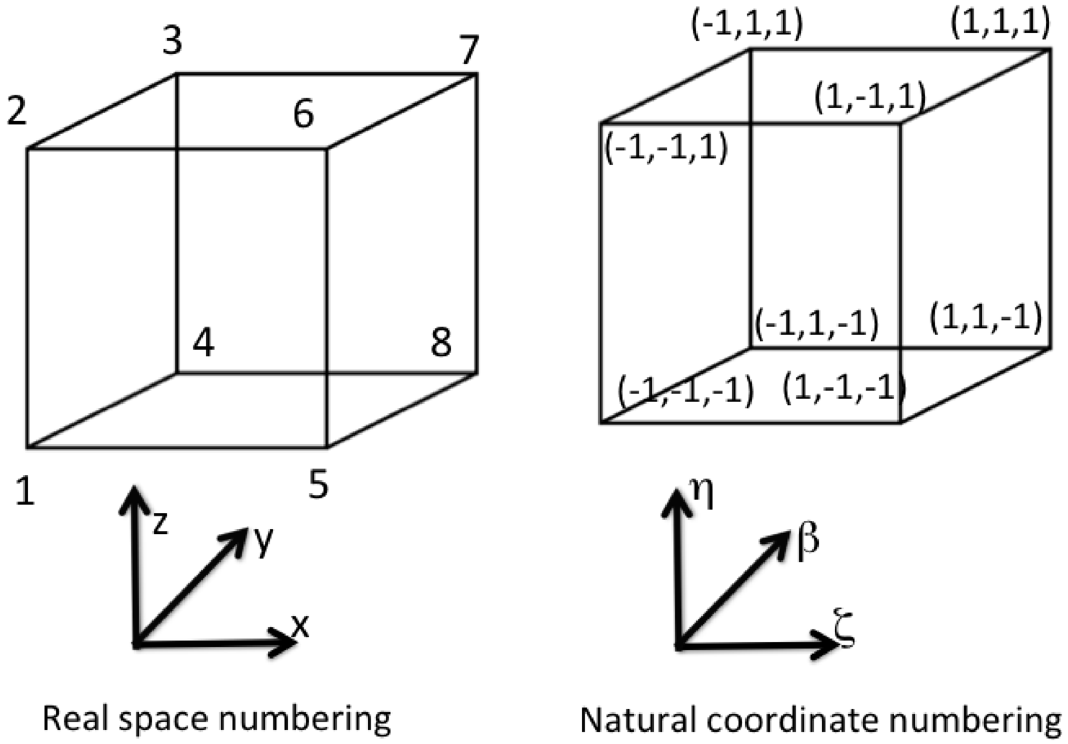

Figure 4.10: The element node numbering used in our calculation for the real space and the natural grid projection.

Then the shape function is calculated in terms of the natural coordinates of the element nodes.

$$\begin{aligned}
\frac{\delta N^I}{\delta \zeta^I}_{8\times3} &= \left[\frac{\delta N^I}{\delta \zeta}\frac{\delta N^I}{\delta \beta}\frac{\delta N^I}{\delta \eta}\right] \\
&= \frac{1}{8}\begin{pmatrix}
-(1-\beta)(1-\eta) & -(1-\zeta)(1-\eta) & -(1-\zeta)(1-\beta) \\
-(1-\beta)(1+\eta) & -(1-\zeta)(1-\eta) & (1-\zeta)(1-\beta) \\
-(1+\beta)(1+\eta) & (1-\zeta)(1-\eta) & (1-\zeta)(1-\beta) \\
-(1+\beta)(1-\eta) & (1-\zeta)(1-\eta) & -(1-\zeta)(1-\beta) \\
(1-\beta)(1-\eta) & -(1-\zeta)(1-\eta) & -(1-\zeta)(1-\beta) \\
(1-\beta)(1+\eta) & -(1-\zeta)(1-\eta) & (1-\zeta)(1-\beta) \\
(1+\beta)(1+\eta) & (1-\zeta)(1-\eta) & (1-\zeta)(1-\beta) \\
(1+\beta)(1-\eta) & (1-\zeta)(1-\eta) & -(1-\zeta)(1-\beta)
\end{pmatrix}
\end{aligned} \tag{4.25}$$

Here, ζ, β and η are the axes in natural coordinates. N^I are the components of the shape function along the natural coordinates.

The real space node locations are given by the matrix,

$$R_{8\times 3} = [X_I Y_I Z_I] \tag{4.26}$$

Here, X_I are the node points of the element in real space coordinates along the grid directions. The Jacobian matrix is calculated as

$$J_{3\times 3} = \left(\frac{\delta N^I}{\delta \zeta^I}\right)^T R \tag{4.27}$$

The space derivatives of the shape function in terms of the natural coordinates are given by,

$$\begin{aligned}
\frac{\delta N^I}{\delta X^I}_{3\times 8} &= J^{-1}\left(\frac{\delta N^I}{\delta \zeta^I}\right)^T \\
&= \begin{pmatrix} \frac{\delta N^I}{\delta X} \\ \frac{\delta N^I}{\delta Y} \\ \frac{\delta N^I}{\delta Z} \end{pmatrix} \qquad (4.28) \\
&= \begin{pmatrix} \frac{\delta N^1}{\delta X} & \frac{\delta N^2}{\delta X} & \frac{\delta N^3}{\delta X} & \frac{\delta N^4}{\delta X} & \frac{\delta N^5}{\delta X} & \frac{\delta N^6}{\delta X} & \frac{\delta N^7}{\delta X} & \frac{\delta N^8}{\delta X} \\ \frac{\delta N^1}{\delta Y} & \frac{\delta N^2}{\delta Y} & \frac{\delta N^3}{\delta Y} & \frac{\delta N^4}{\delta Y} & \frac{\delta N^5}{\delta Y} & \frac{\delta N^6}{\delta Y} & \frac{\delta N^7}{\delta Y} & \frac{\delta N^8}{\delta Y} \\ \frac{\delta N^1}{\delta Z} & \frac{\delta N^2}{\delta Z} & \frac{\delta N^3}{\delta Z} & \frac{\delta N^4}{\delta Z} & \frac{\delta N^5}{\delta Z} & \frac{\delta N^6}{\delta Z} & \frac{\delta N^7}{\delta Z} & \frac{\delta N^8}{\delta Z} \end{pmatrix} \qquad (4.29)
\end{aligned}$$

The strain-displacement matrix is constructed from the shape function as

$$B_{6\times 24} = \begin{pmatrix} \frac{\delta N^I}{\delta X} & 0 & 0 \\ 0 & \frac{\delta N^I}{\delta Y} & 0 \\ 0 & 0 & \frac{\delta N^I}{\delta Z} \\ \frac{\delta N^I}{\delta Y} & \frac{\delta N^I}{\delta X} & 0 \\ 0 & \frac{\delta N^I}{\delta Z} & \frac{\delta N^I}{\delta Y} \\ \frac{\delta N^I}{\delta Z} & 0 & \frac{\delta N^I}{\delta X} \end{pmatrix} \tag{4.30}$$

The anisotropic stiffness coefficient is given by

$$C_{6\times 6} = \frac{E}{(1+\gamma)(1-2*\gamma)}\times$$

$$\begin{pmatrix} 1-\gamma & \gamma & \gamma & & & \\ \gamma & 1-\gamma & \gamma & & & \\ \gamma & \gamma & 1-\gamma & & & \\ & & & \frac{1-2*\gamma}{2} & & \\ & & & & \frac{1-2*\gamma}{2} & \\ & & & & & \frac{1-2*\gamma}{2} \end{pmatrix} \tag{4.31}$$

Here, E is the elastic stiffness coefficient and γ is the Poisson ratio.

The element stiffness matrix is K^e and is calculated by Gaussian integration in the natural coordinates.

$$\begin{aligned} K^e_{24\times 24} &= \int_{-c}^{c}\int_{-b}^{b}\int_{-a}^{a} B(R^I)^T C B(R^I) dX dY dZ \\ &= \int_{-1}^{1}\int_{-1}^{1}\int_{-1}^{1} \mid J \mid B(\zeta^I)^T C B(\zeta^I) d\zeta d\beta d\eta \\ &= \sum_{\zeta=\frac{\pm 1}{\sqrt{3}}}\sum_{\beta=\frac{\pm 1}{\sqrt{3}}}\sum_{\eta=\frac{\pm 1}{\sqrt{3}}} \mid J \mid B(\zeta^I)^T C B(\zeta^I) \end{aligned} \tag{4.32}$$

Here, ±(a,b,c) are the node point coordinates of the linear brick element in real space. Using Isoparametric elements and Gaussian quadrature integration method, improved the element stiffness matrix calculation orders of magnitude faster compared to the standard stiffness matrix calculation process.

Here, we outline the main steps of the numerical implementation of the element matrix calculation. The matrix is calculated by the following function, where the coordinates of the nodal points, poisson ratio and elastic modulus is supplied. The function returns a 576 (24×24) element vector, Ke containing the stiffness matrix elements.

```
formStiffnessMatrix(*Ke,E,NU, x1, y1, z1, x2, y2, z2, x3, y3, z3,
        x4, y4, z4,x5, y5, z5, x6, y6, z6, x7, y7, z7, x8, y8, z8)
```

Since we have to use algebraic operations on small size matrices, it is easier to use the dense matrix data structure of PETSC. The matrices listed above are created with the following data structure:

```
ierr=MatCreateSeqDense(PETSC_COMM_SELF,8,3,PETSC_NULL,&xyzMat);
```

Then we assign values to zeta, beta and eta according to the node numbers (Show in figure)

The dense XYZ matrix is formed taking the value from the 8 corner positions of the brick element for each natural coordinate point. The dNdNat matrix is also formed by calculating the values in the equation (4.25). The following code sequence is used to get the transpose of the dNdNat matrix.

```
MatSetValues(dNdNat,1,&j,3,col,dNdNatArray[j],INSERT_VALUES);
//repeat for all rows
MatAssemblyBegin(dNdNat,MAT_FINAL_ASSEMBLY);
MatAssemblyEnd(dNdNat,MAT_FINAL_ASSEMBLY);
MatTranspose(dNdNat,MAT_INITIAL_MATRIX,&dNdNatTrans);
```

The Jacobian matrix is calculated using the equation (4.27).

```
ierr= MatMatMult(dNdNatTrans,xyzMat,MAT_INITIAL_MATRIX,1.,&J);
```

In order to invert a matrix, we have to first LU factorize it. This is done in a couple of steps. First, an identity matrix is created.

```
  ierr = MatCreateSeqDense(PETSC_COMM_SELF,3,3,PETSC_NULL,&Id);
   ierr = MatSetFromOptions(Id);
   for (i=0; i<3; i++) {
     for (j=0; j<3; j++) {
       if (i==j)
      { dat = 1.0;
        ierr = MatSetValues(Id,1,&i,1,&j,&dat,INSERT_VALUES);}
     }
   }
MatAssemblyBegin(Id,MAT_FINAL_ASSEMBLY);
MatAssemblyEnd(Id,MAT_FINAL_ASSEMBLY);
```

Then the jacobian matrix is LU factored.

```
   ierr = MatGetOrdering(J,MATORDERING_RCM,&perm,&iperm);
   ierr = MatFactorInfoInitialize(&luinfo);
   luinfo.fill = 2.0;
   luinfo.dtcol = 0.0;
   luinfo.zeropivot = 1.e-14;
   luinfo.pivotinblocks = 1.0;
  MatGetFactor(J,MAT_SOLVER_PETSC,MAT_FACTOR_LU,&Jfact);
  MatLUFactorSymbolic(Jfact,J,perm,iperm,&luinfo);
  MatLUFactorNumeric(Jfact,J,&luinfo);
```

Now the identity matrix is used to calculate the inverse of the jacobian matrix. The derivative of the shape functions with respect to the real axis coordinates is obtained as well using the equation (4.28).

```
  MatMatSolve(Jfact,Id,Jinv);
  MatSetUnfactored(Jfact);
MatMatMult(Jinv,dNdNatTrans,MAT_INITIAL_MATRIX,PETSC_DEFAULT,&dNdq);
```

When forming the B matrix, care needs to be taken for efficient extraction of values from the dNdq matrix and setting it in the B matrix. In the following, we extract each entry of dNdq only once and assign those values to the B matrix 3 times. The MatSet/GetValues data structure must be used when performing such operations.

```
for (i=0;i<8;i++)
{
        r=0;
        MatGetValues(dNdq,1,&r,1,&i,&dat);
        r=0;c=i*3;
        MatSetValues(B,1,&r,1,&c,&dat,INSERT_VALUES);
        r=3;c=1+i*3;
        MatSetValues(B,1,&r,1,&c,&dat,INSERT_VALUES);
        r=5;c=2+i*3;
        MatSetValues(B,1,&r,1,&c,&dat,INSERT_VALUES);
//similarly for r=1 and r=2
}
```

Next we form the C matrix using the value of elastic modulus and the poisson ratio. The K^e matrix is calculated using equation (4.31). The values in the K^e are assigned to an 1D array for passing as an argument to the structure stiffness matrix calculation function.

```
 MatMatMult(C,B,MAT_INITIAL_MATRIX,PETSC_DEFAULT,&ki);
 MatTranspose(B,MAT_INITIAL_MATRIX,&Btrans);
 MatMatMult(Btrans,ki,MAT_INITIAL_MATRIX,PETSC_DEFAULT,&ki);
 MatScale(ki,detJ);
MatAXPY(kk,1,ki,SAME_NONZERO_PATTERN);
```

Finally all the dense matrices must be destroyed before the function returns.

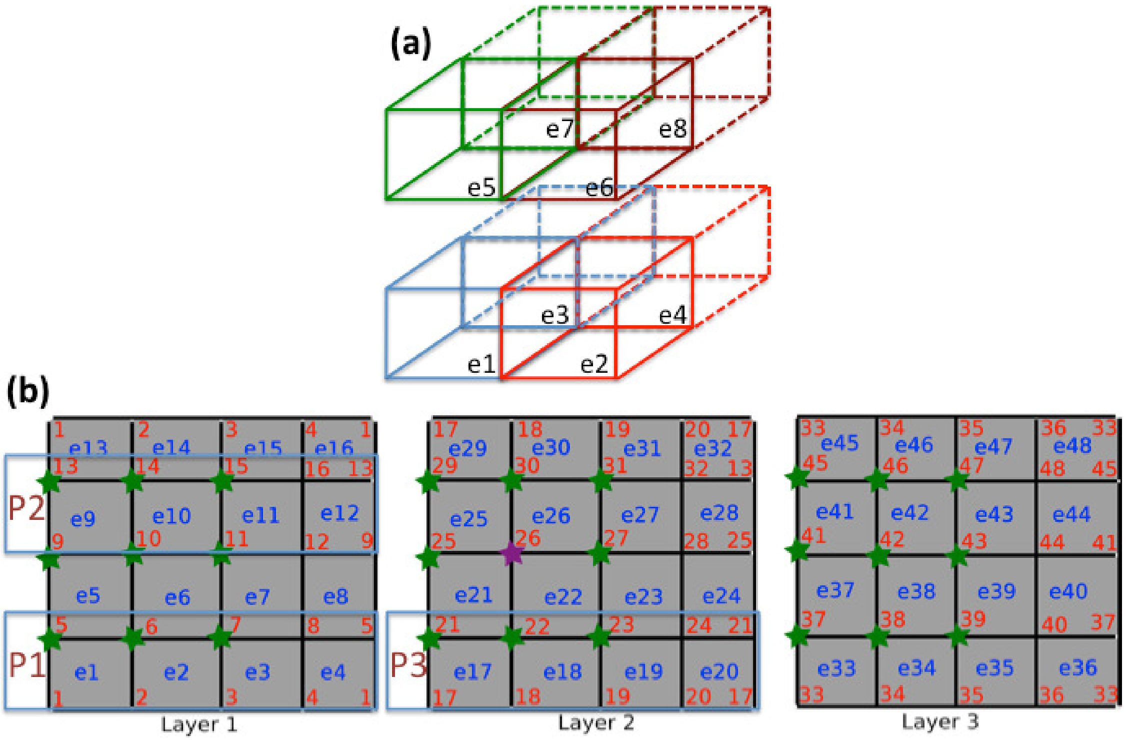

Figure 4.11: (a) FEM structure assembly by element. The newly added element (e8) nodes have matrix element contributions from the 7 elements (e1-7). Note that the contributing elements are only those that precede this element in the natural grid along the three directions. (b) FEM structure matrix assembly by node. The node in consideration is 26 (violet star). Due to the element connectivity the node has interaction with its in-plane surrounding nodes and also the layers above and below this node (green stars). Each node has a total of 26 connected nodes within the body of the structure. The number of connected element and nodes vary at the boundary. These boundary nodes and elements are assembled in a similar procedure with appropriate connectivity.

Assembly

Once the element stiffness matrices are calculated for each of the element, the structure stiffness matrix is constructed by assembling the element stiffness matrices. Assembling the structure stiffness matrix is the main bottleneck in achieving high performance in parallel computation. Initially, we used an element wise assembly process. However, this method turned out to be prohibitive even for a small size of the grid. Then we implemented a node wise assembly algorithm. Still it was difficult to achieve significant performance benefit for large number of processors. This was mainly because of the communication required at the boundary points. Then we calculated the elements at the boundary in order to get rid of any nonlocal assignment. This approach increased the assembly performance significantly and we were able to achieve linear scaling up to thousands of processors.

We used a natural coordinate numbering for the FEM grid (X varying fastest, then Y and then Z). Thus element nodes varying along X direction are nearest neighbor in the global node numbering. In this grid numbering method, the FEM stencil for linear brick elements are widely separated on distributed processors for large number of degrees of freedom (DOF) as shown in Fig4.11. The element connectivity is shown in Fig4.11(a). Here, the added element 8 is connected to other 7 elements that are prior to this element in grid numbering system. Note that the connectivity is only backward, meaning the element stiffness matrix of e8 only depends on the nearest neighbors e1-e7. Elements that are added after e8 to the global grid are not essential for calculating the stiffness matrix of e8. Since each element spans 2 layers, any node has nearest neighbors in the adjacent layers in all the directions. The node connectivity for the FEM stencil is shown in Fig 4.11(b). A specific node under consideration is labeled 26 with a violet star sign. It has 26 connected nodes in 8 elements that contribute to different columns of the row associated with this node. This type of multilayer connectivity of elements makes it very difficult to assemble the structure matrix avoiding non-local assignments. In fact, with our model of element wise assembly process, even a 32×32×3 elements global grid required about 120 seconds to assemble on moderate 4 processors. The poor performance of the element wise assembly originates from the fact that different nodes associated with the nearest neighbor element belong to different processors (Fig 4.11(b)). The communication burden between processors overwhelms the computation benefit even for a small global grid size. Hence, we discarded the element wise assembly process and resorted to a node wise assembly process. The essential idea is to reduce the processor to processor communication as much as possible during global stiffness matrix assembly even at the cost of increased computation within individual processors. We calculate the element matrix elements for eight elements that are connected to a specific node locally. Theoretically this amounts to calculating the matrix element for each element 8 times assuming the worst case scenario where each node of an element belongs to a different processor. However practically, for large global matrices with natural coordinate numbering, the 8 nodes of an element belong to only 2 processors. The 8 nodes are divided into bottom and top layers, each containing 4 nodes and owned by individual processors. This amounts to calculation of the element stiffness matrices only twice instead of eight times. However, even with this double calculation, the node wise assembly process makes the whole element stiffness matrix calculation and assembly local to individual processors. Thus linear scaling performance can be achieved in the global matrix calculation and assembly process for arbitrarily large structures. Note that in comparison, the element wise assembly shows poor scaling performance even for 4 processors for a moderately small grid size. The algorithm for implementing the node wise assembly is as follows:

- Determine the nodes owned by each processor and iterate through them.
- At each iteration, determine the global nodes associated with the 8 nearest neighbor elements of the node and write the global indices of the 27 nearest neighbor nodes in

an (27× 3) array. This array contains the column numbers of the global matrix where the matrix elements will be written.

- At each iteration, determine the global element number of the 8 elements associated with the node and iterate through them
- For each element determine to what node of the element is the node of interest (26) connected
- Iterate through the eight nodes of the element
- Fetch the values from the row of element matrix that corresponds to the node number determined in step iv and add the values.

Thus all the assignments in constructing the global matrix are local. In this manner, we avoid nonlocal assignment of adding values to the structural matrix and achieve more than two orders of magnitude boost in assembly process even for moderate size of the grid(32×32×32×3) compared to direct calculation of element matrices.

A synopsis of the main steps in structure matrix assembly is given here. First we find the grid nodes owned by the current processor.

```
MatGetOwnershipRange(A,&nodeStart,&nodeEnd);
start=((PetscInt)(nodeStart/3));
end=(PetscInt)((nodeEnd-2)/3);
```

Then we find the elements owned by the current processor and for the eight nodes of the element, find the global node number.

```
//For each node find the global FEM stencil
for(kEr=-1;kEr<2;kEr++)
for(jEr=-1;jEr<2;jEr++)
for(iEr=-1;iEr<2;iEr++)
{
//Pos has the global node number of the FEM stencil(3*27 nodes)
//Apply the XY PBC for the four corners
if(r==0 && q==my && jEr==1 && iEr==-1)
{gNode=3*(i+(kEr*(mx+1)*(my+1)-my*(mx+1)+mx));}
//put the right most node as the neighbor of left most node
else if(r==0 && q==0 && jEr==-1 && iEr==-1)
{gNode=3*(i+(kEr*(mx+1)*(my+1)+my*(mx+1)+mx));}
//put the right most node as the neighbor of left most node
else if(r==mx && q==0 && jEr==-1 && iEr==1)
{gNode=3*(i+(kEr*(mx+1)*(my+1)+my*(mx+1)-mx));}
//put the right most node as the neighbor of left most node
else if(r==mx && q==my && jEr==1 && iEr==1)
```

```
{gNode=3*(i+(kEr*(mx+1)*(my+1)-my*(mx+1)-mx));}
//put the right most node as the neighbor of left most node

//Apply the XY PBC for the four lines
else if(r==0 && iEr==-1)
//put the right most node as the neighbor of left most node
{gNode=3*(i+(kEr*(mx+1)*(my+1)+jEr*(mx+1)+mx));}
//put the left most node as the neighbor of right most node
else if(r==mx && iEr==1)
{gNode=3*(i+(kEr*(mx+1)*(my+1)+jEr*(mx+1)-mx));}
//put the rear most node as the neighbor of front most node
else if(q==0 && jEr==-1)
{gNode=3*(i+(kEr*(mx+1)*(my+1)+(my)*(mx+1)+iEr));}
//put the left most node as the neighbor of right most node
else if(q==my && jEr==1)
{gNode=3*(i+(kEr*(mx+1)*(my+1)-my*(mx+1)+iEr));}
else{
gNode=3*(i+(kEr*(mx+1)*(my+1)+jEr*(mx+1)+iEr));
}
//for top and bottom of slab avoid upper or lower layer
if((p==0 && kEr==-1) || (p==mz && kEr==1)) {}
else
{
Pos[3*((kEr+1)*9+(jEr+1)*3+(iEr+1))]=gNode;
Pos[3*((kEr+1)*9+(jEr+1)*3+(iEr+1))+1]=gNode+1;
Pos[3*((kEr+1)*9+(jEr+1)*3+(iEr+1))+2]=gNode+2;
}
}
```

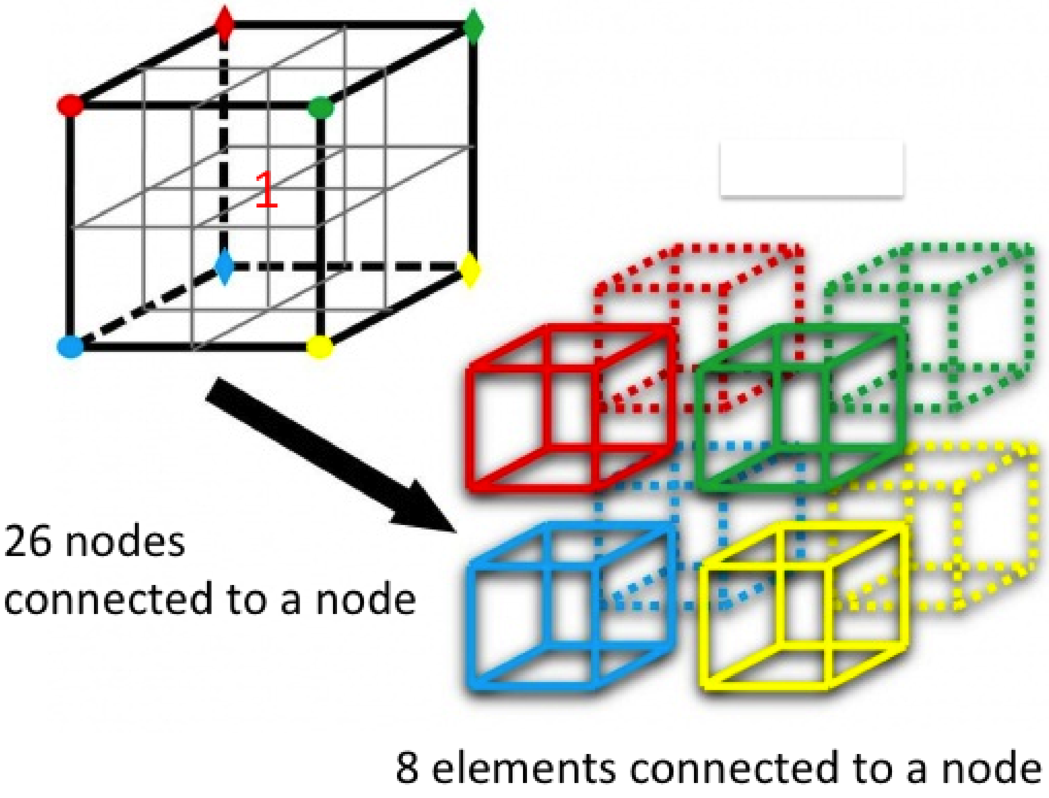

Figure 4.12: Nearest neighbor nodes and elements in a FEM calculation.

For each of the 8 nodes associated with the element, we find out what are the 26 nearest neighbor nodes for each of them and how they are connected. Finding out this nearest neighbor relationship, we want to assign matrix elements calculated for the element to the appropriate nearest neighbor nodes. The difficulty in the process is that matrix elements are calculated for individual elements but the global grid is parallelized according to nodes. The code below performs the mapping between the local and global matrix element assignment.

```
//Iterate through the eight elements associated with the node
for(kEr=0;kEr<2;kEr++)
for(jEr=0;jEr<2;jEr++)
for(iEr=0;iEr<2;iEr++)
{
if((p==0 && kEr==0)|| (p==mz && kEr==1)){}
else{
//determine what element it is
Kerow=(PetscInt)(4*abs(kEr-1)+2*abs(jEr-1)+abs(iEr-1));
//Iterate through the eight nodes of every element
for(kEc=0;kEc<2;kEc++)
```

```
for(jEc=0;jEc<2;jEc++)
for(iEc=0;iEc<2;iEc++)
{
colNum=kEc*4+jEc*2+iEc;
//FEMstenNum is a conversion from element no (0-7)
//to node number in local FEM stencil. It was initialized to
//FEMstenENum[8]={13,12,10,9,4,3,1,0};
posNum=FEMstenENum[Kerow]+kEc*9+jEc*3+iEc;
posVal0[posNum*3]+=Ker[(Kerow*24*3)+3*colNum];
posVal0[posNum*3+1]+=Ker[(Kerow*24*3)+3*colNum+1];
posVal0[posNum*3+2]+=Ker[(Kerow*24*3)+3*colNum+2];
posVal1[posNum*3]+=Ker[(Kerow*3+1)*24+3*colNum];
posVal1[posNum*3+1]+=Ker[(Kerow*3+1)*24+3*colNum+1];
posVal1[posNum*3+2]+=Ker[(Kerow*3+1)*24+3*colNum+2];
posVal2[posNum*3]+=Ker[(Kerow*3+2)*24+3*colNum];
posVal2[posNum*3+1]+=Ker[(Kerow*3+2)*24+3*colNum+1];
posVal2[posNum*3+2]+=Ker[(Kerow*3+2)*24+3*colNum+2];
}
}//end of if for avoiding top and bottom elements
}
```

Now posVal holds the value of the elements at the global grid position Pos. We can store the values in the matrix element for the nodes using the following code.

```
row=i*3;
MatSetValues(A,1,&row,81,Pos,posVal0,ADD_VALUES);
row=i*3+1;
MatSetValues(A,1,&row,81,Pos,posVal1,ADD_VALUES);
row=i*3+2;
MatSetValues(A,1,&row,81,Pos,posVal2,ADD_VALUES);
```

The iteration through the node and assigning values to the global matrix end here. Once all the values have been assigned, we store the matrix for further calculation.

Boundary Conditions

The boundary conditions are applied by making relevant changes to the matrix that contains information for structure stiffness. For example, in the thin film structure, the regularly used boundary condition is periodic along XY, clamped at the bottom and stress free at the top. The periodic boundary condition can be applied during assembly process assuming the elements at the left boundary to be the neighbor for elements on the right boundary as shown above.

The clamped boundary condition is applied by zeroing all the values in the matrix corresponding to the bottom interface leaving the diagonal entries as 1. A specific displacement can be assigned to these nodes by setting these values on the right hand side. The stress free boundary condition is similarly applied by zeroing the forces at the corresponding nodes along the appropriate direction. It is not economical to traverse through a large matrix and assigning values to the nonzero matrix elements. Rather, this operation is performed by finding out the node number in the grid where clamped boundary condition is applied.

```
//Setting the bottom layer x and y component as clamped BC
for(k=0;k<mz+1;k++)
for(j=0;j<my+1;j++)
for(i=0;i<mx+1;i++)
{
ll=k*(mx+1)*(my+1)+j*(mx+1)+i;
if(k==0)
{
rows[count]=3*ll;
count++;
rows[count]=3*ll+1;
count++;
rows[count]=3*ll+2;
count++;}
}
```

Then those rows are zeroed using the command

```
MatZeroRows(A,Ii,rows,1.0);CHKERRQ(ierr);
```

Applying the inhomogeneous boundary condition in finite element is easy since all the matrix elements are calculated for an element. Simply, the change of elastic stiffness and the poisson ratio gives the element matrix for a different material. This element is then added to the global grid in the usual manner. Once these modifications due to the boundary conditions are employed to the matrix and the right hand side vector, the resulting total displacement is calculated by solving the $Kdu = f$ equation. Again we use an iterative Krylov subspace solver for solving the set of linear equations.

Body Force

The polarization causes an eigen strain in the unit cell. The eigen strain is included in the elastic equation as a body force. First, the eigen strain is calculated using the electrostriction coefficients. The body forces due to the eigen strain for each element are calculated and assigned to the element nodes. The eigen strain and the body forces are given by

$$\begin{aligned} \epsilon^0_{ii} &= Q_{11}P_i^2 + Q_{12}(P_j^2 + P_k^2) \\ \epsilon^0_{ij} &= Q_{44}P_iP_j \\ F^0_i &= \int_\Omega [B]^T[C]\epsilon^0_{kl}d\Omega \end{aligned} \tag{4.33}$$

Here, Q_{ij} are the electrostriction coefficients.

Next, the elastic equilibrium is calculated from

$$Kdu_i = F_i^0 \tag{4.34}$$

Here, K is the structure stiffness matrix including the appropriate boundary condition and du_i is the displacement.

In matrix notation, we first calculate eigen stress from the eigen strain.

$$\begin{pmatrix} \sigma_{xx}^0 \\ \sigma_{yy}^0 \\ \sigma_{zz}^0 \\ \sigma_{xy}^0 \\ \sigma_{yz}^0 \\ \sigma_{zx}^0 \\ \\ \end{pmatrix} = \frac{E}{(1+\gamma)(1-2*\gamma)} \times$$

$$\begin{pmatrix} 1-\gamma & \gamma & \gamma & & & \\ \gamma & 1-\gamma & \gamma & & & \\ \gamma & \gamma & 1-\gamma & & & \\ & & & \frac{1-2*\gamma}{2} & & \\ & & & & \frac{1-2*\gamma}{2} & \\ & & & & & \frac{1-2*\gamma}{2} \\ \\ \end{pmatrix} \times \begin{pmatrix} \epsilon_{xx}^0 \\ \epsilon_{yy}^0 \\ \epsilon_{zz}^0 \\ \epsilon_{xy}^0 \\ \epsilon_{yz}^0 \\ \epsilon_{zx}^0 \\ \\ \end{pmatrix} \tag{4.35}$$

Then we calculate the body forces by multiplying with B^T.

$$\begin{pmatrix} F_x^0 \\ F_y^0 \\ F_z^0 \\ \end{pmatrix} = \begin{pmatrix} \frac{\delta N^I}{\delta X} & 0 & 0 & \frac{\delta N^I}{\delta Y} & 0 & \frac{\delta N^I}{\delta Z} \\ 0 & \frac{\delta N^I}{\delta Y} & 0 & \frac{\delta N^I}{\delta X} & \frac{\delta N^I}{\delta Z} & 0 \\ 0 & 0 & \frac{\delta N^I}{\delta Z} & 0 & \frac{\delta N^I}{\delta Y} & \frac{\delta N^I}{\delta X} \\ \\ \end{pmatrix} \times \begin{pmatrix} \sigma_{xx}^0 \\ \sigma_{yy}^0 \\ \sigma_{zz}^0 \\ \sigma_{xy}^0 \\ \sigma_{yz}^0 \\ \sigma_{zx}^0 \\ \\ \end{pmatrix} \tag{4.36}$$

Numerical Implementation of the body force calculation is given below.

```
//Spontaneous strain calculation from the polarization values.
  for (k=zs; k<zs+zm; k++) {
  for (j=ys; j<ys+ym; j++) {
  for (i=xs; i<xs+xm; i++) {
     eps0xx=
```

```
          pow(appctx->Ps,2)*(
          Q11*pow(Px_localptr[k][j][i],2)+
          Q12*pow(Py_localptr[k][j][i],2)+
          Q12*pow(Pz_localptr[k][j][i],2)
          );
//similarly for other components
}}}
```

Spontaneous stress is calculated using the following code.

```
 sig0zz=Estiff*(C12*eps0xx+appctx->C12*eps0yy+appctx->C11*eps0zz);
 sig0xy=Estiff*C44*eps0xy;
//similarly for other components
```

The spontaneous force on the eight nodes can now be calculated from the eigen stress as follows.

```
N1fx_lptr[k][j][i]=B[0][0]*sig0xx+B[1][0]*sig0xy+B[2][0]*sig0zx;
N2fx_lptr[k][j][i]=B[0][1]*sig0xx+B[1][1]*sig0xy+B[2][1]*sig0zx;
N4fx_lptr[k][j][i]=B[0][3]*sig0xx+B[1][3]*sig0xy+B[2][3]*sig0zx;
N5fx_lptr[k][j][i]=B[0][4]*sig0xx+B[1][4]*sig0xy+B[2][4]*sig0zx;
N3fx_lptr[k][j][i]=B[0][2]*sig0xx+B[1][2]*sig0xy+B[2][2]*sig0zx;
N6fx_lptr[k][j][i]=B[0][5]*sig0xx+B[1][5]*sig0xy+B[2][5]*sig0zx;
N7fx_lptr[k][j][i]=B[0][6]*sig0xx+B[1][6]*sig0xy+B[2][6]*sig0zx;
N8fx_lptr[k][j][i]=B[0][7]*sig0xx+B[1][7]*sig0xy+B[2][7]*sig0zx;
//similarly for other components
```

These are nodal force vectors for single element. Now, the total force for each node is obtained by finding the contribution from all the 8 nearest neighbor elements. They have to be added in order to get the total force for a given node. One problem here is that, we have to use the arrays to assign values to other force vector arrays. This process does not work in the PETSC implementation.In order to avoid this problem ,we have to assemble the vector first and then extract the local part again so that they can be used to assign values to the total force vector. We obtain the local array using the following code.

```
DAVecRestoreArray(appctx->da,N7fz,&N7fz_lptr);
DAVecRestoreArray(appctx->da,N8fz,&N8fz_lptr);
//Get Local vectros out of the nodal forces
DAGetLocalVector(appctx->da,&N1fx_local);
DAGlobalToLocalBegin(appctx->da,N1fx,INSERT_VALUES,N1fx_local);
DAGlobalToLocalEnd(appctx->da,N1fx,INSERT_VALUES,N1fx_local);
DAVecGetArray(appctx->da,N1fx_local,&N1fx_local_lptr);
```

We add the element force vectors to obtain the total force. We have to keep track of the boundary conditions and the nearest neighbor here. For example, at the top surface, there are 4 nearest neighbor, so the force assignment goes as,

```
if(k==mz-1 && k!=0 && j!=0 && i!=0)
{
  fx_lptr[k][j][i]+=N2fx_local_lptr[k-1][j][i];
  fx_lptr[k][j][i]+=N3fx_local_lptr[k-1][j-1][i];
  fx_lptr[k][j][i]+=N6fx_local_lptr[k-1][j][i-1];
  fx_lptr[k][j][i]+=N7fx_local_lptr[k-1][j-1][i-1];}
```

In the bulk, there are 8 regular nearest neighbors. Hence, the assignment goes as,

```
if(k!=0 && j!=0 && i!=0)
{   fx_lptr[k][j][i]+=N1fx_local_lptr[k][j][i];
  fx_lptr[k][j][i]+=N2fx_local_lptr[k-1][j][i];
  fx_lptr[k][j][i]+=N4fx_local_lptr[k][j-1][i];
  fx_lptr[k][j][i]+=N5fx_local_lptr[k][j][i-1];
  fx_lptr[k][j][i]+=N3fx_local_lptr[k-1][j-1][i];
  fx_lptr[k][j][i]+=N6fx_local_lptr[k-1][j][i-1];
  fx_lptr[k][j][i]+=N7fx_local_lptr[k-1][j-1][i-1];
  fx_lptr[k][j][i]+=N8fx_local_lptr[k][j-1][i-1];}
  //similarly for other components
```

These force vectors are calculated from the polarizations that were defined on a DA grid. However, the FEM matrix and the subsequent solve is performed on a natural grid. We do the DA to natural grid transformation using the following method. We first create three vectors in natural ordering and then copy the DA vector values to the natural vector values.

```
 VecCreate(PETSC_COMM_WORLD,&dx0);
strain_size=appctx->l*appctx->m*appctx->n;
VecSetSizes(dx0,PETSC_DECIDE,strain_size);
VecSetFromOptions(dx0);
VecDuplicate(dx0,&dy0);
VecDuplicate(dx0,&dz0);
DAGlobalToNaturalBegin(appctx->da,fx_DA,INSERT_VALUES,dx0);
DAGlobalToNaturalEnd(appctx->da,fx_DA,INSERT_VALUES,dx0);
///similarly for other components
```

The number of rows in the strain matrix and vectors is 3(6 with shear) times than that of the electrostatic matrix. So the DA converted vectors need to be added properly in order to get a vector 3 times its size. This is done by the follwoing code.

```
d0[0]=dx0;
d0[1]=dy0;
d0[2]=dz0;
VecStrideScatterAll(d0,appctx->f0,INSERT_VALUES);
```

After the assembly of 3 vectors in the global f0 vector, we apply the boundary conditions. For prescribed displacements on a boundary, we simply assign the displacement value in the vector. Since, the strain stiffness matrix has been constructed in a way so that clamped points have only 1 in the diagonal entry, assigning the prescribed displacement automatically assigns this displacement value to the boundary node. The stress free boundary condition on top is applied by zeroing the z component of the force vector corresponding to the boundary nodes. This is done in the following way

```
//Get local array from the global vector
VecGetOwnershipRange(appctx->f0,&start,&end);
VecGetArray(appctx->f0,&f0_lptr );

for(s=start;s<end;s++)
{
p=(s/3)/(mx*my);
q=((s/3)
r=((s/3)
ll=3*(p*mx*my+q*(mx)+r)-start;
//prescribe clamped on the bottom part
if (p==0){
f0_lptr[ll]=0.0;
f0_lptr[ll+1]=0.0;
f0_lptr[ll+2]=0;
}
//zero fz on the top part
if (p==mz-1)
{f0_lptr[ll+2]=0;}
}
```

Once these modifications due to the boundary conditions are employed to the matrix and the right hand side vector, the resulting total displacement is calculated by solving the $Kdu = f$ equation in the natural grid.

Strain Force Calculation

The strain calculated in the last section is performed on a natural grid. However, the polarization and the electrostatics is defined on a DA grid.Once we have the strain in natural grid, we have to convert it to DA grid for calculating the force due to strain. We start this process by dividing the vector into one third for the same reason we added 3 vectors above. And then we convert the natural vectors to DA vectors. The main functions implementing this operation is shown below.

```
VecSetBlockSize(appctx->uStrain ,3);
//The unit of spontaneous displacement is w.r.to the
//reduced length which itself has length of 1nm
d0[0]=uStrainIH;
```

```
d0[1]=vStrainIH;
d0[2]=wStrainIH;
VecStrideGatherAll(uStrain,d0,INSERT_VALUES);
DANaturalToGlobalBegin(da,uStrainIH,INSERT_VALUES,uStrainDA);
DANaturalToGlobalEnd(da,uStrainIH,INSERT_VALUES,uStrainDA);
```

Now we have the displacement values in DA vectors. We can use them to calculate the strain at each point.

```
//tensile strain
if(i>0)
{e11=appctx->um+a*(ustrIH_lptr[k][j][i]-ustrIH_lptr[k][j][i-1]);}
if(j>0)
{e22=appctx->um+a*(vstrIH_lptr[k][j][i]-vstrIH_lptr[k][j-1][i]);}
if(k>0){
e33=((-1)*appctx->um/appctx->NU)+a*1*
(wstrIH_lptr[k][j][i]-wstrIH_lptr[k-1][j][i]);
}
//shear strain
if (i!=0 && j!=0 && k!=0)
{
e12=((ustrIH_lptr[k][j][i]-ustrIH_lptr[k][j-1][i])
        +(vstrIH_lptr[k][j][i]-vstrIH_lptr[k][j][i-1]));
e23=((wstrIH_lptr[k][j][i]-wstrIH_lptr[k][j-1][i])
        +(vstrIH_lptr[k][j][i]-vstrIH_lptr[k-1][j][i]));
e31=((ustrIH_lptr[k][j][i]-ustrIH_lptr[k-1][j][i])
        +(wstrIH_lptr[k][j][i]-wstrIH_lptr[k][j][i-1]));
```

Once we have the nodal strain, we can calculate the energy due to strain and the resulting force.

$$\begin{aligned} F_{elas} = & \frac{1}{2}C_{11}(e_{11}^2+e_{22}^2+e_{33}^2)+C_{12}(e_{11}e_{12}+e_{22}e_{33}+e_{33}e_{11}) \\ & +2C_{44}(e_{12}^2+e_{23}^2+e_{13}^2) \end{aligned} \tag{4.37}$$

This can be separated into three parts.

$$F_{elas1} = \frac{1}{2}C_{11}(\epsilon_{11}^2+\epsilon_{22}^2+\epsilon_{33}^2)+C_{12}(\epsilon_{11}e_{12}+\epsilon_{22}\epsilon_{33}+\epsilon_{33}\epsilon_{11})+2C_{44}(\epsilon_{12}^2+\epsilon_{23}^2+\epsilon_{13}^2) \tag{4.38}$$

$$F_{elas2} = \beta_{11}(P_x^4+P_y^4+P_z^4)+\beta_{12}(P_x^2P_y^2+P_z^2P_y^2+P_z^2P_y^2) \tag{4.39}$$

$$\begin{aligned} F_{elas3} = & -(q_{11}\epsilon_{11}+q_{12}\epsilon_{22}+q_{12}\epsilon_{33})P_x^2-(q_{11}\epsilon_{22}+q_{12}\epsilon_{11}+q_{12}\epsilon_{33})P_y^2 \\ & -(q_{11}\epsilon_{33}+q_{12}\epsilon_{11}+q_{12}\epsilon_{22})P_z^2-2q_{44}(\epsilon_{12}P_xP_y+\epsilon_{23}P_zP_y+\epsilon_{13}P_xP_z) \end{aligned} \tag{4.40}$$

Here, e is the elastic strain and ϵ is the total strain.

$$\beta_{11} = \frac{1}{2}C_{11}(Q_{11}^2 + 2Q_{12}^2) + C_{12}(Q_{12}(2Q_{11} + Q_{12}) \tag{4.41}$$

$$\beta_{12} = C_{11}Q_{12}(2Q_{11} + Q_{12}) + C_{12}(Q_{11}^2 + 3Q_{12}^2 + 2Q_{11}Q_{12}) + 2C_{44}Q_{44}^2 \tag{4.42}$$

$$q_{11} = C_{11}Q_{11} + 2C_{12}Q_{12} \tag{4.43}$$

$$q_{12} = C_{11}Q_{12} + C_{12}(Q_{11} + Q_{12}) \tag{4.44}$$

$$q_{44} = 2C_{44}Q_{44} \tag{4.45}$$

In the energy expressions, the first term is totally dependent on the strain, hence does not affect the polarization dynamics. The second term modifies the second and fourth order coefficients of the polarization. The last term is the electro-striction term that has both polarization and total strain dependence and hence contribute to the polarization dynamics. This force due to the electro-striction term is calculated as,

```
Esx=((q11*e11+q12*e22+q12*e33)*2*Px_localptr[k][j][i]
+2*q44*(e12*Py_localptr[k][j][i]+e31*Pz_localptr[k][j][i]))
-beta11*pow(Px_localptr[k][j][i],3)-beta12*pow(Px_localptr[k][j][i],1)
*(pow(Py_localptr[k][j][i],2)+pow(Pz_localptr[k][j][i],2));
```

These force components due to the strain is added to the total force at each time step.

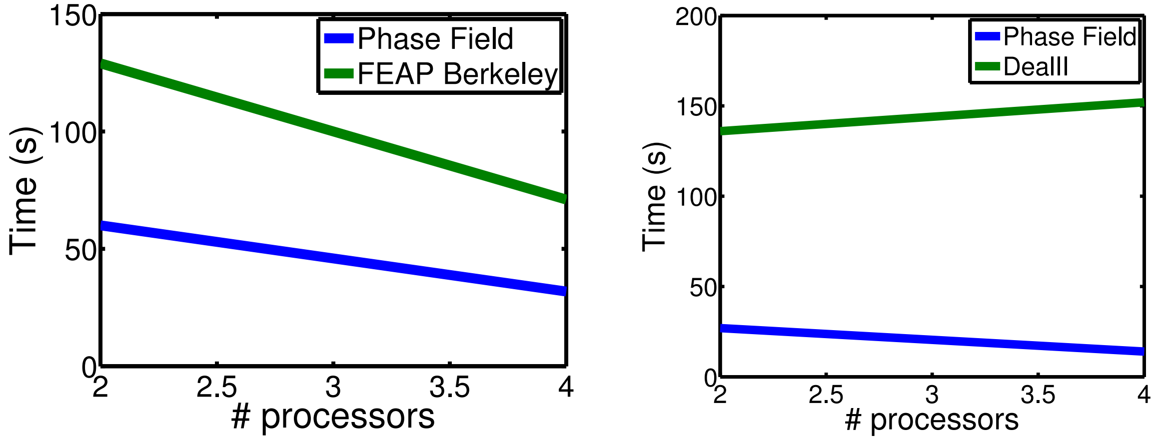

Figure 4.13: Performance comparison of the FEM calculation with FEAP and DealII on single node 4 processors.

We compared the performance of strain calculation with publicly available softwares. The comparison here is only for 2 and 4 processors due to the lack of access to large clusters during the time of this writing. The comparison with FEAP is performed for a 70×70×70 grid size with linear brick element. These quoted numbers are obtained from the parallel FEAP manual. For these structures, we see a factor of 2 improvement in terms of calculation speed. Next we compared the speed with DealII only for assembly since this is the most time consuming part of the calculation. We see that, for 4 processors, the time required for Deal II assembly increases. This is probably because with increase of processors, the number of boundary points are increasing. Since DealII depends on PETSC compress function for nonlocal assignment, the performance could decrease with increasing number of processors for small number of processors. For larger number of processors and large structure size, this anomaly could be removed and linear scaling could be achieved. However, our phase field code scales at smaller number of processors as well and shows a factor of 4 improvement for assembly of a structure of size 70×70×32. These improvements could become more prominent for large number of processors.

Thermal Force

In the TDGL equation, $\zeta_i(\vec{r}$,t) is the random force due to thermal fluctuation that has a zero mean and a gaussian variance. That is, $< \zeta_i(\vec{r},t) >= 0$ and $< \zeta_i(\vec{r},t)\zeta_j(\vec{r}',t') >= 2k_BTL\delta(\vec{r}-\vec{r}')\delta(t-t')$. PETSC generates a uniformly distributed random number within a given interval. The following transformation is applied in order to ensure gaussian distribution,

$$\zeta_i = -2log(R_1)sin(2\pi R_2)cos(2\pi R_2)\frac{\sqrt(\frac{2k_BT}{dt})}{\Delta} \tag{4.46}$$

Here, R_1 and R_2 are two randomly generated numbers, dt and Δ are time and space discretization size respectively and k_B is the Boltzmann constant, T is the temperature. Since, these thermal forces have to be calculated for each point in the spatial grid, we create random vectors to generate these forces in parallel.

```
VecSetRandom(Fu_fut ,appctx->pGRandom);
VecSetRandom(Fv_fut ,appctx->pGRandom);
```

Extract the local part of the vector and arrays.

```
DAGetLocalVector(appctx->da,&Fu_local);
DAGetLocalVector(appctx->da,&Fv_local);

DAGlobalToLocalBegin(appctx->da, Fu_fut ,INSERT_VALUES, Fu_local);
DAGlobalToLocalEnd(appctx->da, Fu_fut ,INSERT_VALUES, Fu_local);
DAGlobalToLocalBegin(appctx->da, Fv_fut ,INSERT_VALUES, Fv_local);
DAGlobalToLocalEnd(appctx->da, Fv_fut ,INSERT_VALUES, Fv_local);

DAVecGetArray(appctx->da, Fu_local,&Fu_lptr);
//similarly for other components
```

Iterate though the local part of the vector to assign Gaussian distributed forces.

```
 for (k=zs; k<zs+zm; k++) {
  for (j=ys; j<ys+ym; j++) {
  for (i=xs; i<xs+xm; i++) {
```

```
Fw_lptr[k][j][i]=-.02*log(Fu_lptr[k][j][i])
                        *sin(2*pi*Fv_lptr[k][j][i])
                        *cos(2*pi*Fv_lptr[k][j][i])
                        *pow(2*kbT*cm/dtt,0.5)/delta;
}}}
```

Save the local and global vectors.

```
DAVecRestoreArray(appctx->da,Fu_local,&Fu_lptr);
DARestoreLocalVector(appctx->da,&Fu_local);
//similarly for other components
```

4.6 Time Integration

We tested both the explicit forward-euler and the velocity verlet algorithm. The forward-euler method is prohibitive for long time dynamics due to the reasons mentioned in the Temporal Requirement section. The velocity verlet algorithm allowed for an order of magnitude longer time steps compared to the direct forward euler method for stiff problems. In order to check the accuracy of the results, we simulated the results presented in Ref. [10]. Both equilibrium and kinetic results were tested. With reduced space discretization length of 1nm and reduced time step size of 0.01, we reproduced the results presented in Ref. [10]. We used the same space and time discritization length for the results reported here. The velocity-verlet integration algorithm implemented is given by the equations.

$$\begin{aligned} P^p_{i+1} &= P^c_i + \frac{\delta P^c_i}{\delta t}\Delta t \\ \frac{\delta P^c_{i+1}}{\delta t} &= \frac{1}{2}\left(\frac{\delta P^c_i}{\delta t} + \frac{\delta P^p_{i+1}}{\delta t}\right) \\ P^p_{i+1} &= P^c_i + \frac{\delta P^c_{i+1}}{\delta t}\Delta t \end{aligned} \tag{4.47}$$

The principal part of the time integration is implemented as follows.

```
//Calculate polarization for the next step
VecWAXPY(Px_fut,appctx->dt,F_u,Px);   //Px_fut=dt*F_u+Px
VecWAXPY(Py_fut,appctx->dt,F_v,Py);   //Py_fut=dt*F_v+Py
VecWAXPY(Pz_fut,appctx->dt,F_w,Pz);   //Pz_fut=dt*F_w+Pz

//calculate strain driven force
calcSpontStrain(Px,Py,Pz,appctx.f0,&appctx);
KSPSolve(kspStrain,appctx.f0,appctx.uStrain);
calcStrainForce(Px,Py,Pz,F_u,F_v,F_w,&appctx);
```

```
//calculate charge and find the electrostatic potential
 calcCharge(Px_fut,Py_fut,Pz_fut,appctx->C_u,appctx);
 DMMGSolve(dmmg);
 VecCopy(DMMGGetx(dmmg),appctx->potential);}

//calculate the total force
calcForce(Px_fut,Py_fut,Pz_fut,Fu_fut,Fv_fut,Fw_fut,appctx);

//calculate the corrected force
VecAXPBY(F_u,0.5,0.5,Fu_fut);  //F_u=.5*Fu_fut+.5*Fu
VecAXPBY(F_v,0.5,0.5,Fv_fut);  //F_v=.5*Fv_fut+.5*Fv
VecAXPBY(F_w,0.5,0.5,Fw_fut);  //F_w=.5*Fw_fut+.5*Fw

//update polarization
VecAXPY(Px,appctx->dt,F_u);    //Px=Px+dt*F_u
//similarly for other components
```

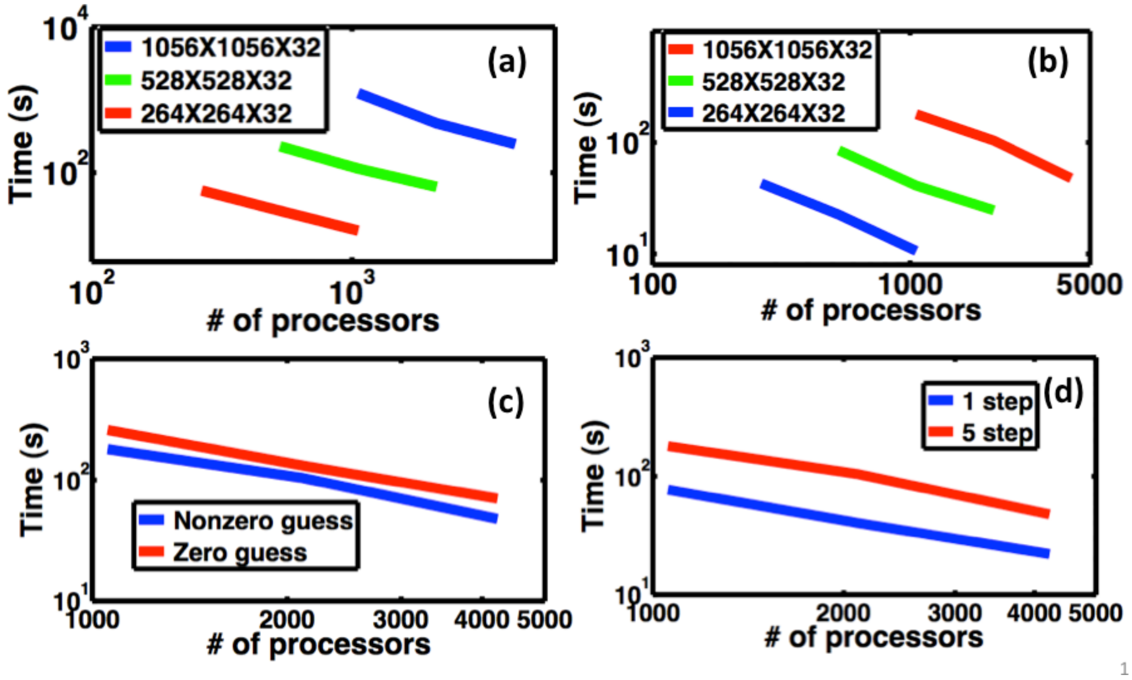

Figure 4.14: (a) The FEM stiffness matrix assembly time as a function of the number of processors used with varying grid size. (b) The total cycle time for 6 iterations including the nonlocal electrostatic and elastic interactions as a function of the number of processors used with varying grid size. (c) Using a non-zero initial guess from the last time step solution, for the linear solver during the electrostatic and elastic interaction calculation improves the overall performance of the by a factor of 2 for all number of processors used. (d) Calculation of the long range interactions every 5 steps compared to every single step, improved the

performance by about 4 times. This does not change the physical results since, the long range interactions usually act at low frequency compared to the short range interaction. For all the three structure sizes, we obtain linear scaling.

4.7 Performance

The parallel performance of the 3D phase-field code was analyzed on Hopper of the NERSC facility. The Hopper machine is equipped with 24 2.1 GHz processors and 32 GB memory per node. It uses Gemini interconnect for inter node communication that has a latency of ~1 μs. In FIG 4.14(a) we show the parallel performance of the FEM assembly algorithm. Three different sizes of the grid are assembled from a micron to a quarter micron square device. The smallest structure is assembled using 264 processors taking 57 seconds. When 1056 processors are used, the assembly time reduces to 16 seconds. Thus we achieve a nearly linear scaling for the assembly process. Similar scaling behavior is also achieved for larger structures (up to micron size) using more number of processors (up to 5k) as shown in FIG 4.14(a). For small deformations of the structures during the switching process, it is sufficient to work with the initial FEM stiffness matrix at subsequent time steps. Hence, we separate the assembly process and cycle time for each iteration of the self-consistent phase-field calculation. Each time step of the phase-field calculation consists of calculating the local bulk energy, domain wall energy and the non-local electrostatic and elastic energy. In FIG 4.14(b), we show the total cycle time of 6 iterations. For the smallest grid (same as FIG 4.14(a)), the average time for a single time step is 7.1 s with 264 processors. The cycle time reduces to 1.7 s when 1056 processors are used. Again, the computation time per cycle scales linearly with increasing number of processors. The larger grid sizes with increasing number of processors show similar scaling behavior. For calculation of non-local interactions during time stepping, if we initialize the linear solver with the result of the last time step, the number of iteration required for the linear solver used in both electrostatic and elastic calculation, decreases significantly. We gain an overall two fold performance benefit for all structure sizes tested across different number of processors as shown in FIG. 4.14(c)). We also found that, when simulating the spatially extended dynamics of a ferro-electric structure, the short range interactions gives rise to stiffness. However, the long range interactions usually have a longer temporal wavelength. Hence, for fixed size of the time step, it is reasonable to sample the long range interactions every few sample of the short range dynamics. Hence, we calculate the long range interaction once after every 5 steps of the short range interaction calculation. We find that this approximation does not change the physical results obtained. However, the overall cycle time reduces by about 4 fold as shown in FIG. 4.14(d). Thus significant improvement in scale can be achieved by a parallel implementation of the phase-field model. Reaching the micron scale could enable direct comparison of simulation results with experimental observation that we discuss next.

4.8 Normalized Coefficients

In all the calculations presented here, the actual coefficients were normalized according to the following equations.

$$
\begin{aligned}
\hat{r} &= \sqrt(\frac{|\alpha|_1}{G_{11} r}) \\
\hat{P} &= \frac{\vec{P}}{\vec{P}_s} \\
\tau &= |\alpha_1| L t \\
{\alpha_1}' &= \frac{\alpha_1}{|\alpha_1|} \\
{\alpha_{11}}' &= \frac{\alpha_{11} \times {P_s}^2}{|\alpha_1|} \\
{\alpha_{111}}' &= \frac{\alpha_{111} \times {P_s}^4}{|\alpha_1|} \\
{\alpha_{112}}' &= \frac{\alpha_{112} \times {P_s}^4}{|\alpha_1|} \\
{\alpha_{123}}' &= \frac{\alpha_{123} \times {P_s}^4}{|\alpha_1|} \\
q'_{11} &= \frac{q_{11}}{|\alpha_1|} \\
q'_{12} &= \frac{q_{12}}{|\alpha_1|} \\
q'_{44} &= \frac{q_{44}}{|\alpha_1|} \\
C'_{11} &= \frac{C_{11}}{|\alpha_1| \times {P_s}^2} \\
C'_{12} &= \frac{C_{12}}{|\alpha_1| \times {P_s}^2} \\
C_4 4' &= \frac{C_{44}}{|\alpha_1| \times {P_s}^2} \\
\Delta x' &= \frac{\Delta x}{l_0} \\
\alpha_0 &= |\alpha_1|_{T=25^0 C} \\
l_0 &= \sqrt(\frac{G_{110}}{\alpha_0}) \\
G'_{11} &= \frac{G_{11}}{G_{110}} \qquad (4.48)
\end{aligned}
$$

Here, α_i are the Landau coefficients. G_{11} is the domain wall energy, $\hat{r}$ is the normalized distance, $\hat{P}$ is the normalized polarization, P_s is the saturation polarization, τ is the reduced time, L is the mobility coefficient, q_{ii} are the electro-striction coefficients, C_{ii} are the Young's modulus of the material.

4.9 Rotation of Axis

Sometimes, we have to rotate the axis of the grid in order to incorporate the boundary conditions. In these cases, it is required to write the bulj energy and the corresponding force in a rotated frame. This is accomplished by the rotation tensors. For example, for the muliferroic material BFO_3, the Landau coefficients are given in the (001) coordinate. We can rotate the polarization to (111) by using the tensor,

$$t_{ij}^{(111)} = \begin{pmatrix} 0 & \frac{1}{\sqrt{2}} & -\frac{1}{\sqrt{2}} \\ -\frac{2}{\sqrt{6}} & \frac{1}{\sqrt{6}} & \frac{1}{\sqrt{6}} \\ \frac{1}{\sqrt{3}} & \frac{1}{\sqrt{3}} & \frac{1}{\sqrt{3}} \end{pmatrix} \tag{4.49}$$

The polarization coefficients in the (111) coordinate are,

$$P_i' = t_{ij} P_i \tag{4.50}$$

From the Landau coefficients on the (001) coordinate, the free energy in the (111) coordinate can be written as

$$\begin{aligned} E_{bulk}^{(111)} = {} & \alpha_1[(t_{i1}P_i')^2 + (t_{i2}P_i')^2 + (t_{i3}P_i')^2] + \alpha_{11}[(t_{i1}P_i')^2 + (t_{i2}P_i')^2 + (t_{i3}P_i')^4] \\ & + \alpha_{12}[(t_{i1}P_i')^2(t_{i2}P_i')^2 + (t_{i1}P_i')^2(t_{i3}P_i')^2 + (t_{i2}P_i')^2(t_{i3}P_i')^4] \end{aligned} \tag{4.51}$$

The corresponding force on each point is calculated by taking the derivative with respect to the polarization. For example, the three components of the force from the above energy profile is

$$\begin{aligned} Fx' = & -\frac{\delta E}{\delta P_1} \\ = & -2\alpha_1[(t_{i1}P_i')t_{11} + (t_{i2}P_i')t_{12} + (t_{i3}P_i')t_{13}] \\ & -4\alpha_{11}[(t_{i1}P_i')^3 t_{11} + (t_{i2}P_i')^3 t_{12} + (t_{i3}P_i')^3 t_{13}] \\ & -2\alpha_{12}[(t_{i1}P_i')t_{11}(t_{i2}P_i')^2 + (t_{i1}P_i')^2 t_{12}(t_{i2}P_i') \\ & +(t_{i1}P_i')t_{11}(t_{i3}P_i')^2 + (t_{i1}P_i')^2 t_{13}(t_{i3}P_i') \\ & +(t_{i2}P_i')t_{12}(t_{i3}P_i')^2 + (t_{i2}P_i')^2 t_{13}(t_{i2}P_i')] \end{aligned} \tag{4.52}$$

$$
\begin{aligned}
Fy' =& -\frac{\delta E}{\delta P_2} \\
=& -2\alpha_1[(t_{i1}P_i')t_{21} + (t_{i2}P_i')t_{22} + (t_{i3}P_i')t_{23}] \\
& -4\alpha_{11}[(t_{i1}P_i')^3 t_{21} + (t_{i2}P_i')^3 t_{22} + (t_{i3}P_i')^3 t_{23}] \\
& -2\alpha_{12}[(t_{i1}P_i')t_{21}(t_{i2}P_i')^2 + (t_{i1}P_i')^2 t_{22}(t_{i2}P_i') \\
& +(t_{i1}P_i')t_{21}(t_{i3}P_i')^2 + (t_{i1}P_i')^2 t_{23}(t_{i3}P_i') \\
& +(t_{i2}P_i')t_{22}(t_{i3}P_i')^2 + (t_{i2}P_i')^2 t_{23}(t_{i2}P_i')]
\end{aligned}
\tag{4.53}
$$

$$
\begin{aligned}
Fz' =& -\frac{\delta E}{\delta P_3} \\
=& -2\alpha_1[(t_{i1}P_i')t_{31} + (t_{i2}P_i')t_{32} + (t_{i3}P_i')t_{23}] \\
& -4\alpha_{11}[(t_{i1}P_i')^3 t_{31} + (t_{i2}P_i')^3 t_{32} + (t_{i3}P_i')^3 t_{33}] \\
& -2\alpha_{12}[(t_{i1}P_i')t_{31}(t_{i2}P_i')^2 + (t_{i1}P_i')^2 t_{32}(t_{i2}P_i') \\
& +(t_{i1}P_i')t_{31}(t_{i3}P_i')^2 + (t_{i1}P_i')^2 t_{33}(t_{i3}P_i') \\
& +(t_{i2}P_i')t_{32}(t_{i3}P_i')^2 + (t_{i2}P_i')^2 t_{33}(t_{i2}P_i')]
\end{aligned}
\tag{4.54}
$$

Thus the forces on a rotated frame can be obtained by making use of the rotation tensor.

4.10 Conclusion

In summary, we have reported a massively parallel time domain phase field model. We have achieved nearly linear scaling for all the steps in the calculation. The near perfect scaling allows us to simulate the switching dynamics of micron scale devices. Especially, the nonlinear response of multi-domain ferroelectric films caused by arbitrary electrostatic and mechanical boundary conditions can be easily studied and direct comparison with the experimental results can be made. We believe that the model will be useful in predicting device operation at the length scale where a lot of current experiments are being performed.

Chapter 5

Multi-domain Ferroelectric Switching

5.1 Introduction

In this chapter, we show the simulation result of lateral switching on various surfaces of the multiferroic material BFO. We make direct comparison with multiple experiments recently reported on various surfaces of BFO. Finally, we propose a method to control domain size during polarization switching that could be crucial for device applications using BFO.

5.2 Domain Formation

First, we show the domain formation process on the (001) surface of BFO. We start from a random distribution of polarization. As the polarizations evolve from zero average values, the domains slowly form and create the stripe domain pattern as observed in experiment. There were no constraints used in the simulation process. The simulator is able to capture the domain formation automatically.

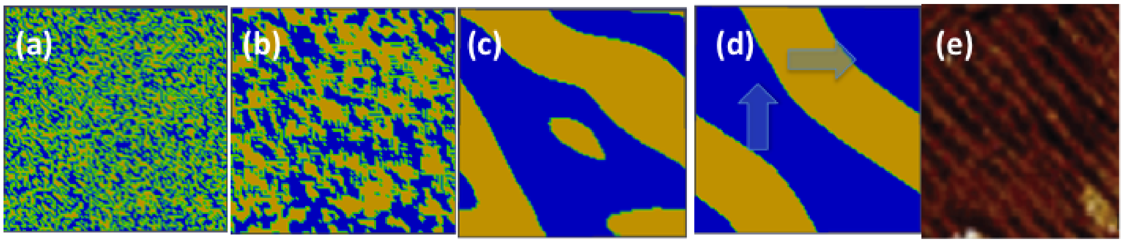

Figure 5.1: Polarization evolution on the (001) surface of BFO starting from a random polarization distribution. The experimental domain pattern is reproduced from the simulation.

5.3 Horizontal Switching

In this section, we show the calculation results of ferroelectric switching and domain pattern evolution on the 001 surface of BFO and emphasize the importance of electrical boundary condition on the observed switching pattern. The presented simulation results have the dimension of 1056nm×1056nm×32nm. The energy was normalized so that dimensionless space-time are obtained following Ref. [20]. The spatial grid size is 1 nm and time step size is 0.005. We also performed benchmark calculation with grid size of 0.5nm. The domain switching mechanism described here did not change when a smaller discretization length is used. The thermodynamic parameters for BFO were obtained from Ref. [50]. A generic device structure incorporating the multiferroic material is shown in FIG. 4.5(a). The device shows the ferroic material is coherently strained by the substrate. An in-plane electric field is applied using the two in-plane electrodes. The electrostatic boundary condition of the film surface is controlled by placing a metal or dielectric or simply leaving it open. This representative device structure is a prototype of many recent experimentally reported ferroelectric devices.

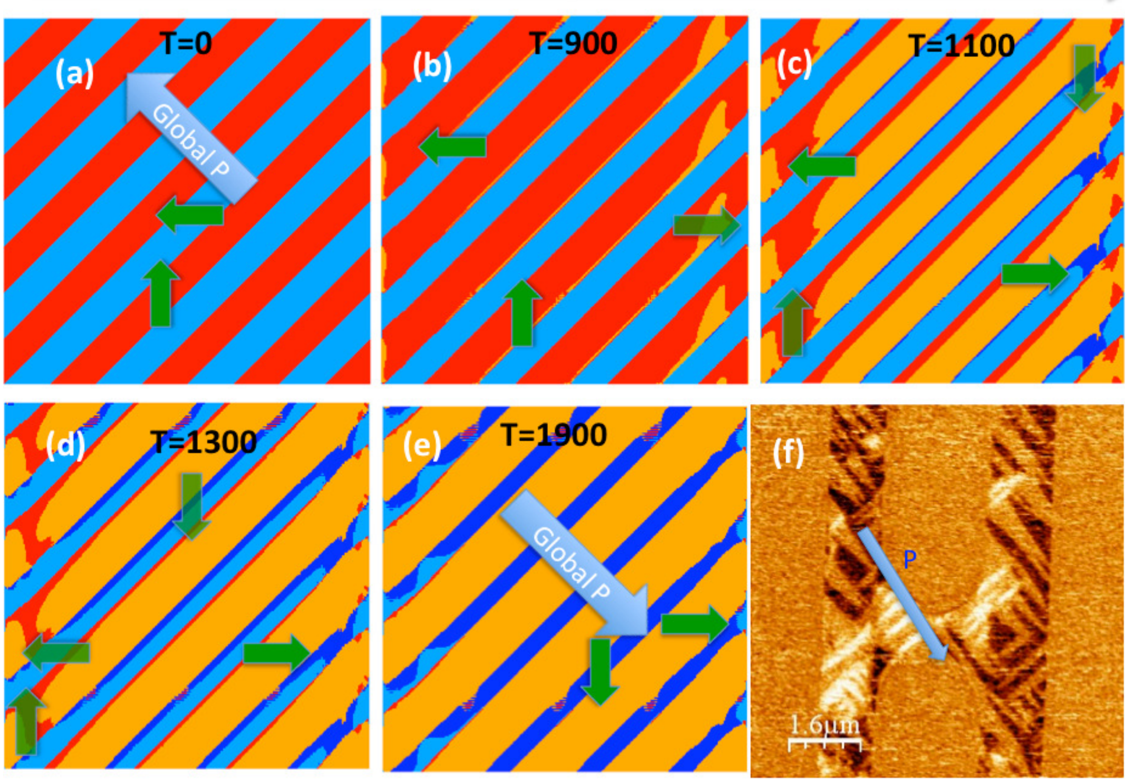

Figure 5.2: Evolution of the polarization on the (001) surface under short circuit boundary condition. (a) The initial domain pattern with left (light blue) and up(red) polarization domains. (b) Nucleation of right polarization domain (yellow) through 71° switching of up domains. (c) 71° switched domain (yellow) grows. (d,e) A new domain grows towards south

(deep blue) and eventually switches the whole domain. The global polarization switches by 180° in the process. (f) Experimental observation of 180° switch of the domains under a short circuit boundary condition (Reprinted with permission from Phys. Rev. Lett. 107, 217202 (2011). Copyright 2011 American Physical Society)

.

In this particular case, a metallic boundary condition was applied on the top (001) surface. We assumed that the thin film is coherently strained by the substrate. A low electric field was applied along the [110] direction that is just above the coercive field of the 71° switch. The evolution of the thin film BFO as a function of time is shown in FIG. 5.2. The application of an in-plane voltage on a BFO thin film with striped domain structure can only generate in-plane 71° and 109° switching events. BFO's thermodynamic potential profile is such that $\mathrm{E}_c(71^\circ) < \mathrm{E}_c(109^\circ)$. The calculated coercive field of the 71° switch is 420 kV/cm and for the 109° switch it is 490 kV/cm. Considering the as grown 71° striped BFO configuration represented in FIG. 5.2, the high saturation polarization (90 μC/cm^2) of BFO causes all of the domains to arrange in-plane in a head-to-tail configuration so that the dipole-dipole energy is minimized. Now, for an applied electric field of strength $\mathrm{E}_c(109^\circ) < \mathrm{E}_{applied} < \mathrm{E}_c(71^\circ)$ and directed from left to right (here along [110] BFO), our calculation demonstrates that the ferroelectric domains with an in-plane polarization oriented perpendicular to the applied electric field align first towards the direction of this external field (from $[\bar{1}1\bar{1}]$ BFO to $[11\bar{1}]$ BFO)(Fig. 5.2(c)). This corresponds to a 71° switching event due to the applied field (in-plane switching of the ferroelectric domain oriented antiparallel to the electric field would correspond to a 109° switching event, from $[\bar{1}\bar{1}\bar{1}]$ BFO to $[11\bar{1}]$ BFO). The ferroelectric switching begins at the domain wall. Although, the simulation was started from a uniform polarization distribution within the domains, some domain regions(yellow) switch earlier than the rest of the domains. This specific pattern formation during the switching process is a result of the long range electrostatic interaction. Non-uniform charge originates in the domain during switching which causes this electrostatic field. Thus some region of the domain are under a higher effective electric field compared to the other regions. Eventually the whole domain switches along the applied field direction. The switched domain (yellow) generates an energetically unfavorable head-to-head configuration at the wall. The theoretical maximum limit of the dipole-dipole fields at these domain walls can reach up to 10^4 kV/cm due to the induced charge. Domains originally oriented antiparallel to the electric field (along $[\bar{1}\bar{1}\bar{1}]$BFO) then switch in-plane by 90° (corresponding to a second 71° switching event to the direction $[1\bar{1}\bar{1}]$ BFO) under this dipole-dipole field to recover the preferred head-to-tail configuration of the polarizations (dark blue region). Note that the actual electric field in the film does not reach even close to the maximum possible theoretical limit since during switching dynamics none of the domains are fully saturated. Also, in an experimental condition mobile charges may compensate some fraction of the domain wall charge and thus reduce the applied field. However, the anisotropic growth of the domains indicate that the domain walls are never fully compensated in these samples.The growth of a new domain also exhibits a pattern due to electrostatic interaction. Note that, this long range electrostatic interaction is in-plane due to the metallic boundary condition applied on the top surface. We have described a second order switching that occurs in this configuration and compared to experiment in ref. [19].

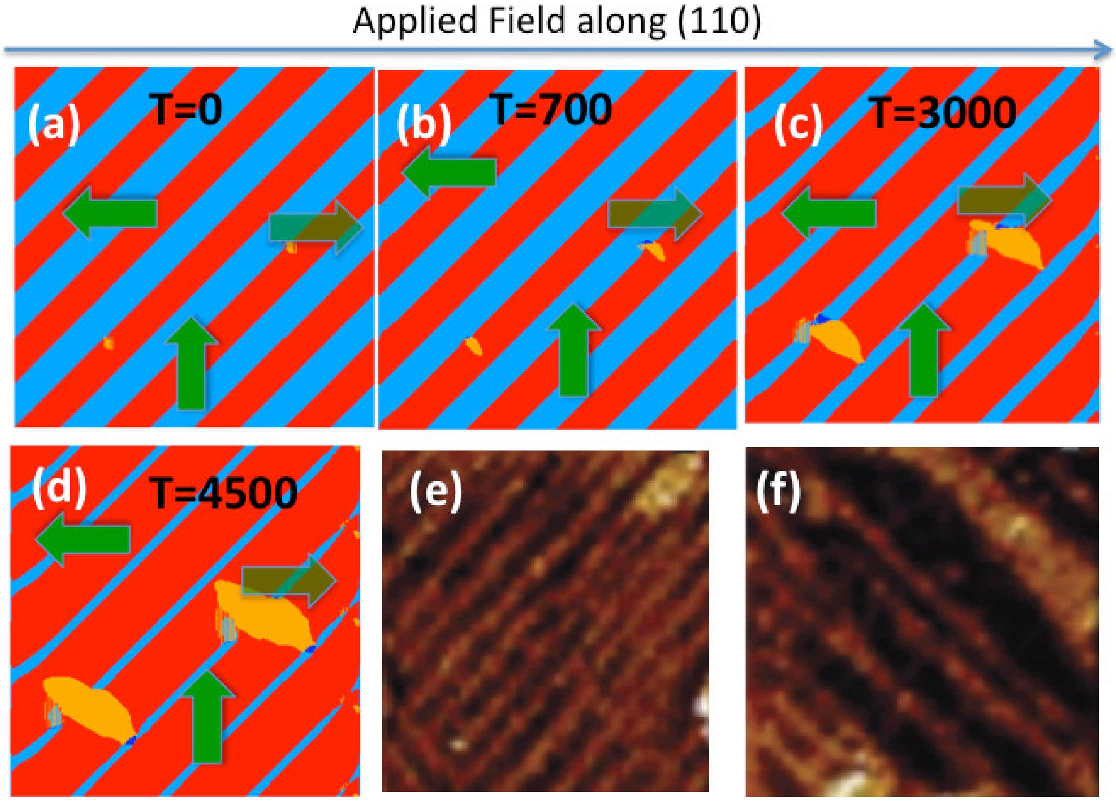

Figure 5.3: Evolution of the polarization on the (001) surface with an open boundary condition. (a) The initial domain pattern with left (light blue) and up(red) oriented polarization domains. (b) Anisotropic growth of right oriented domain(yellow) through a 71° switch of the up(red) oriented polarization to right oriented domain(yellow). (c) The up(red) oriented domain grows simultaneously through domain wall switching of the left (light blue) domain. (d) Emergence of domain patterns (between red and yellow domains) aligned at 90° to the initial domain pattern. (e,f) PFM image showing the 90° switch of domain pattern under open circuit boundary condition (Reprinted with permission from Nat. Mater. 7, 478 (2008). Copyright 2008 Nature Publishing Group.)

In order to emphasize the important role that electrical boundary conditions play for the domain pattern reorganization during lateral electrical switching, we simulated the same device structure with open boundary condition. A Neumann boundary condition was applied on the top surface with the top 5 layers as air. Due to the difference in dielectric constant between BFO (ϵ=100) and air (ϵ=1), most of the electric field go through air. The 3D electrostatic interaction makes the growth of the domains anisotropic. When an open circuit boundary condition is applied, a completely different result in terms of the domain pattern is obtained as shown in FIG. 5.3. We introduced two nucleation centers in the initial domain in order to study how these nucleated domains grow when an electric field is applied. These switched regions (yellow) cause a charged domain walls with the initial domain (red). The charges at the domain wall is reduced by growth of the switched domain(yellow) perpendicular to the initial domain wall as shown in FIG. 5.3(b). When the growing domain (yellow) enters the left oriented (light blue) region (FIG. 5.3(c)), the polarizations in the two domains (light blue and yellow) are head to head. In this region, the yellow domain grow perpendicular to the electrodes rather than perpendicular to the initial domains. However, due to domain wall switching, most of the region is up directed (red). Hence, the growth of the newly formed domain(yellow) is mostly perpendicular to the initial domain wall. Overall, we observe a new domain pattern consisting of red and yellow regions that is at 90° to the initial domain pattern as shown in FIG. 5.3(d). Experimentally this type of switching has been observed in planar switching of BFO with open circuit boundary condition [13]. Note that the domain walls have reconstructed and the width of the domains with polarization along the applied field is higher. This 90° reorientation of the domain pattern with an applied field is solely due to the anisotropic growth of domains that occur at the domain walls.

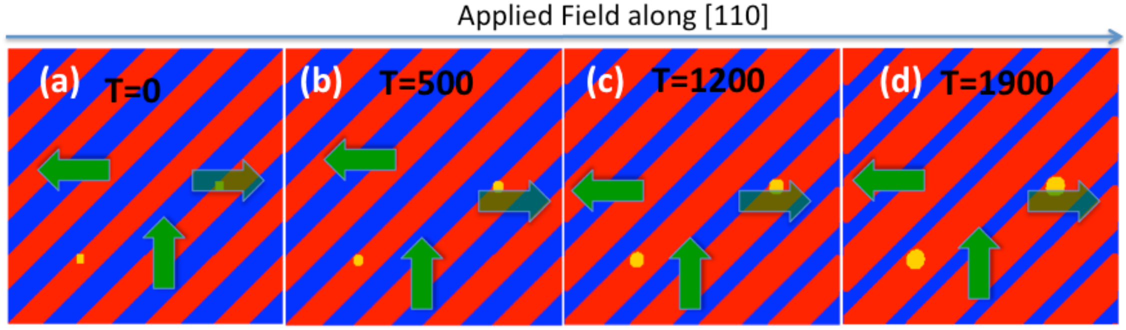

Figure 5.4: Evolution of the polarization on the (001) surface with an open boundary condition without considering the domain wall charge. (a) The initial domain pattern. (b) Isotropic growth of right oriented polarization domain (yellow) through an 71° switch of the up polarization (red). (c,d) Gradual isotropic growth of the switched domain (yellow) due to the applied field. The emergent domains that do not have a specific stripe like pattern since the effect of charge was ignored.

If we ignore the charges at the domain walls, then the individual domains grow isotropically as shown in Fig 5.4. Due to the isotropic growth, the reconstructed pattern do not show any specific topography also the domain wall speed is significantly slow. This result is unphysical, since the presence of electrical charge should make the pattern stripe like.

Applied Field Along (100) Direction

Study of temporal evolution of ferroelectric domain switching is facilitated by recent advent of in-plane capacitor geometry and PFM analysis. There are a number of recent experimental report on the temporal evolution of the ferroelectric domain under a lateral applied electric field [49, 4]. Here, we show the simulation result of ferroelectric domain switching on the (001) plane of BFO when the applied field is along the [100] direction, as shown in Fig 5.5. An open circuit boundary condition was applied in the same manner as described in the previous section. The device geometry corresponds to that of [49]. Similar switching mechanism applies to that reported in [4]. The simulated device dimension is 1056nm×264nm×32nm.

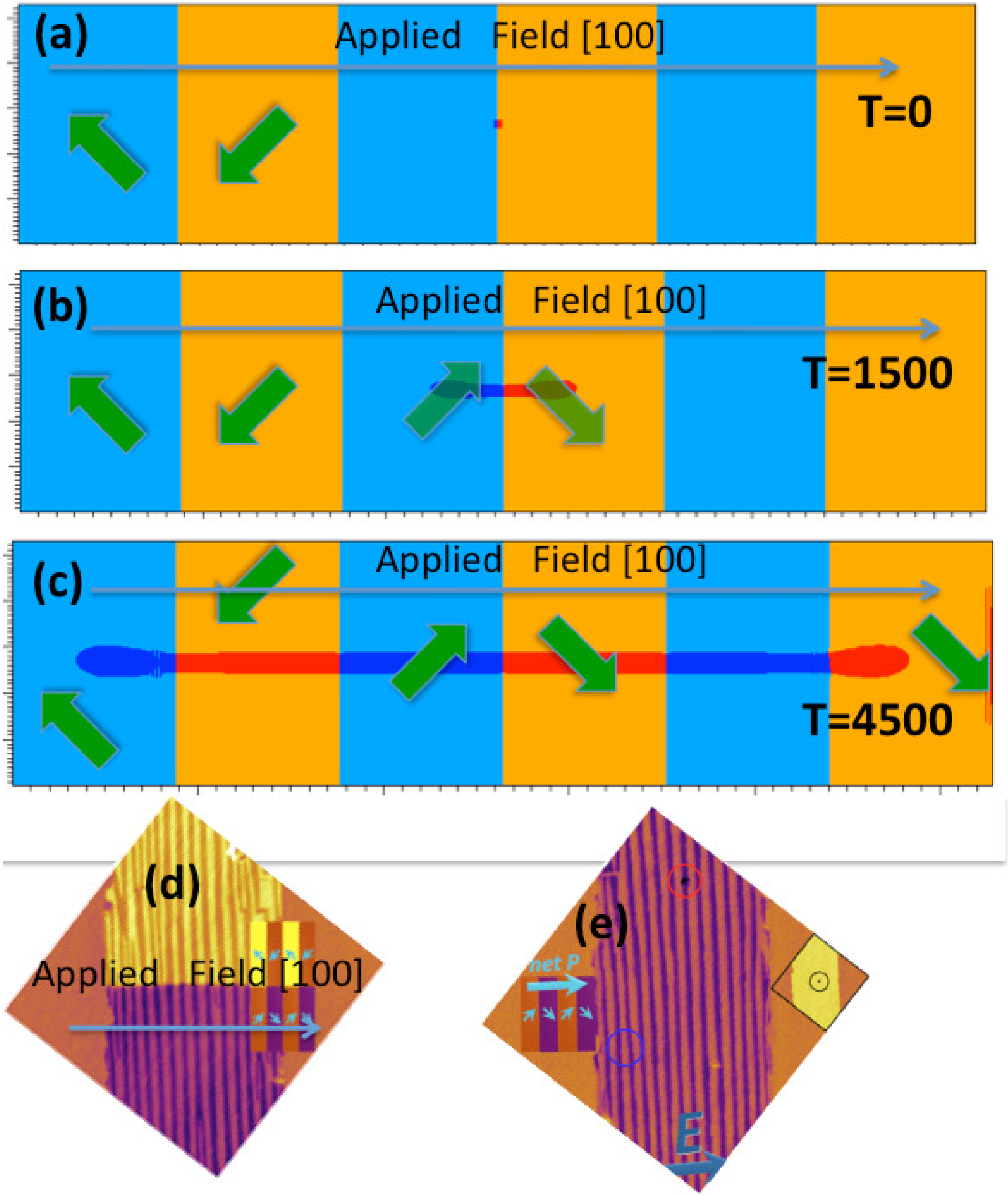

Figure 5.5: Evolution of the polarization on the (001) surface with an open boundary condition when a field is applied along the [100] direction. (a) The initial domain pattern with a defect introduced where the switching starts(dark blue and red dot). (b) Anisotropic growth of right oriented polarization domain (dark blue and red) through an 71° switch of the left polarization (light blue and yellow) along the applied field direction. (c) The anisotropic growth continues and switches regions close to the electrode. Slow growth perpendicular to the applied field and retention of the domain size matches very well with the experimental observation. (d,e) Experimental data showing the intermediate stage between switching (Reprinted with permission from Appl. Phys. Lett. 97, 062910 (2010). Copyright 2010 American Institute of Physics).

There are two initial domain variants on the (001) surface. The $[\bar{1}1\bar{1}]$ (light blue) and $[\bar{1}\bar{1}\bar{1}]$ (yellow). A single nucleation site was introduced as a nucleation point in the $[\bar{1}1\bar{1}]$ domain where the nucleated polarization is oriented along the $[11\bar{1}]$ direction. A voltage of -75 V was applied on the right electrode while the left electrode was grounded. In this case, the switching initially occurs at the nucleation center due to strained walls where the $[\bar{1}1\bar{1}]$ (light blue) polarizations switch along the $[11\bar{1}]$ (dark blue) direction and $[\bar{1}\bar{1}\bar{1}]$ (yellow) domains switch along $[1\bar{1}\bar{1}]$ (red). The initial switching is isotropic as shown in Fig. 5.5(a). However, as the switching domain grow, the walls that are parallel to the electrodes are charged (due to head to head polarization configuration). On the other hand, the walls perpendicular to the electrodes are uncharged but strained. In subsequent switching steps, the charged domain wall grows significantly faster than the sidewise strained wall. The incorporation of inhomogeneous electric field in the model capture this physical process that occur due to the creation of charged domain walls. The inhomogeneous electric fields due to the domain wall charges terminate at the electrode. The sign of the charges are such that they aid the applied field along the applied field direction. Hence the polarizations are under a higher effective field along the applied field direction in the regions where striped domain region is formed. Anisotropic domain growth occurs due to this effective electric field as shown in Fig. 5.5(b). Once a narrow stripe has been created due to forward domain growth, the domain walls perpendicular to the electrodes are charge compensated. The wall growth velocity is significantly slower in the sidewise direction than in the forward direction. At this stage, domains grow only perpendicular to the electrodes(5.5(c)).

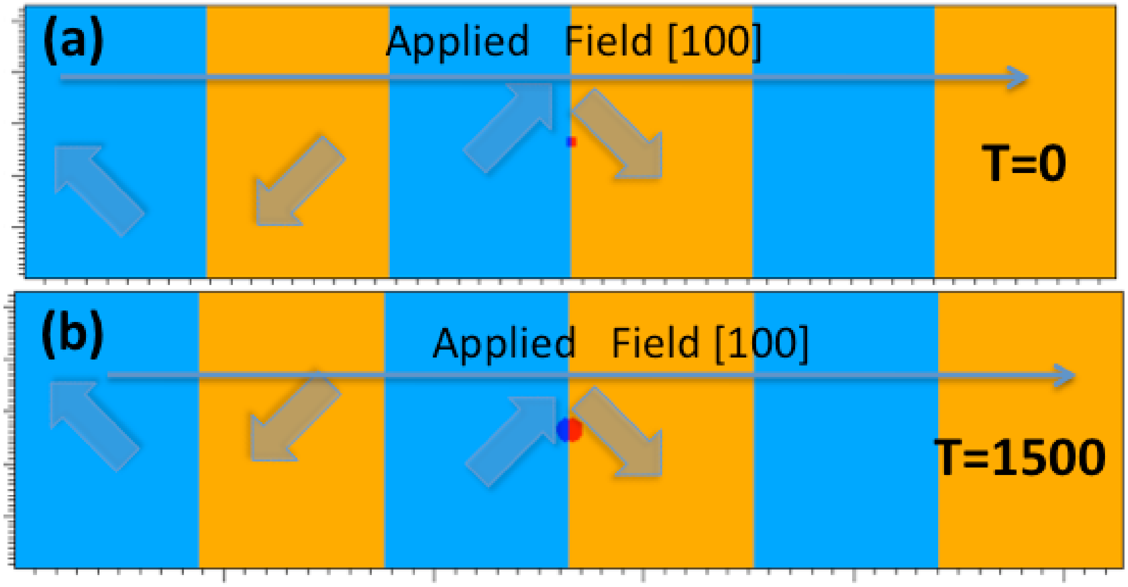

Figure 5.6: Evolution of the polarization on the (001) surface with an open boundary condition when a field is applied along the [100] direction without considering the domain wall charge. (a) The initial domain pattern with a defect introduced where the switching starts. (b) Isotropic growth of right oriented polarization domain (dark blue) through a 71° switch of the left polarization (light blue) along the applied field direction.

The anisotropic growth of the domain wall occurs due to the creation of charge at the switched domain wall. If we do not consider the domain wall charge, then the domain growth is isotropic and a circular domain is created due to the isotropic domain wall energy. The domain growth in this case is shown in Fig. 5.6. In a previous study, it was shown that the space charge and defect could compensate the domain wall charge [**xiao˙PRL05**]. At room temperature, it is expected that the defect diffusion rate is significantly slower compared to the domain wall velocity. Also, from the anisotropic growth of the domains, it is evident that the propagating walls are charged. Thus in these experiments, the domain walls are not fully compensated.

Domain Reconstruction

One interesting aspect of the anisotropic switching process is that in this case no domain wall reconstruction takes place. The coercive field for switching at the domain wall is in fact same as that for the strained sidewise domain switching. However, the nature of the domain wall switch is that at the domain wall, polarization from one domain switches towards the polarization in the other domain. For an applied field that is perfectly symmetric with respect to the two polarization domains, there occurs a frustrated condition for switching from initial to the final polarization direction as the probability of switching in either directions are the same. Thus we find that for an applied field that is orthogonal to the domain walls cannot move the walls during switching and no domain size reconstruction takes place. On the contrary, when the applied field is not perpendicular to the domain wall, the applied field is not symmetric with respect to the polarizations in the adjacent domains. One direction of the DW switching becomes preferable compared to the other. The DW propagates deterministically in a specific direction and the domain size reconstructs. This type of DW switching and domain size reconstruction is shown in Fig. 5.2. It is important to note that the suppression of DW switching occurs due to the same coercive field of the two domain variants at the wall. So if the saturation polarization in the two domains are different, for example due to anisotropic strain, then the coercive field for DW switching will also be different for the two adjacent domains. In this case, an applied field perpendicular to the domain wall will also cause DW switching and consequently DW movement. However, depending on the relative magnitude of the coercive fields for the two processes, it is possible to find an angle with respect to the domain wall where the coercive field for the two processes are the same. In brief, it is possible to find a direction for the applied field such that during the switching process, the DW switching is locked and no domain size reconstruction takes place irrespective of the anisotropic strain introduced by the substrate. For real applications, domain size control could be an important design parameter.

5.4 Conclusion

In summary, we have shown the results of lateral electric field switching incorporating the multiferroic material BFO and compared the obtained results with multiple experimental results. We have particularly emphasized the importance of charge driven domain growth mechanism that explains the temporal evolution of ferroelectric domains observed in experiments. We have also elucidated the role of electrostatic boundary condition on the lateral multi-domain ferroelectric switching. Finally, we predict a method of domain size control during ferroelectric switching which could find important applications in device design using these materials.

Chapter 6

Switching Speed and Energy

6.1 Introduction

In this chapter, we analyze the energy dissipation and switching speed of a magnetoelectric device using our experimentally benchmarked model. We show that (i) incorporation of inhomogeneous strain in a multi-domain switching process predicts the correct experimental coercive field of thin film BiFeO3 and (ii) an inhomogeneous electric field distribution due to an AFM tip qualitatively describes the experimental domain wall velocity for a range of applied fields. (iii) We show that in scaled nanoscale islands, the coercive voltage scales almost linearly and (iv) finally, for the first time, that the estimated per unit area energy dissipation in these devices can be up to one order of magnitude lower compared to the alternative magnetic switching routes like the spin transfer torque devices.

6.2 Device Structure

A typical magnetoelectric device is shown in Fig. 6.1. A magnetic nanodot is placed on top of the BFO thin film. Electric field is applied on the magnetic dot that switches the polarization in BFO that in turn switches the magnet. The polarization directions in a BFO unit cell are shown in Fig. 6.2. Three different surfaces of BFO are studied in this work. They are (001), (110), and (111). The magnetic energy scale is orders of magnitude lower than the ferroelectric energy scale. The switching energy and dynamics are practically determined by the polarization dynamics in these systems. Hence, in this work, we will only focus on the switching dynamics and energy dissipation in the ferroelectric material.

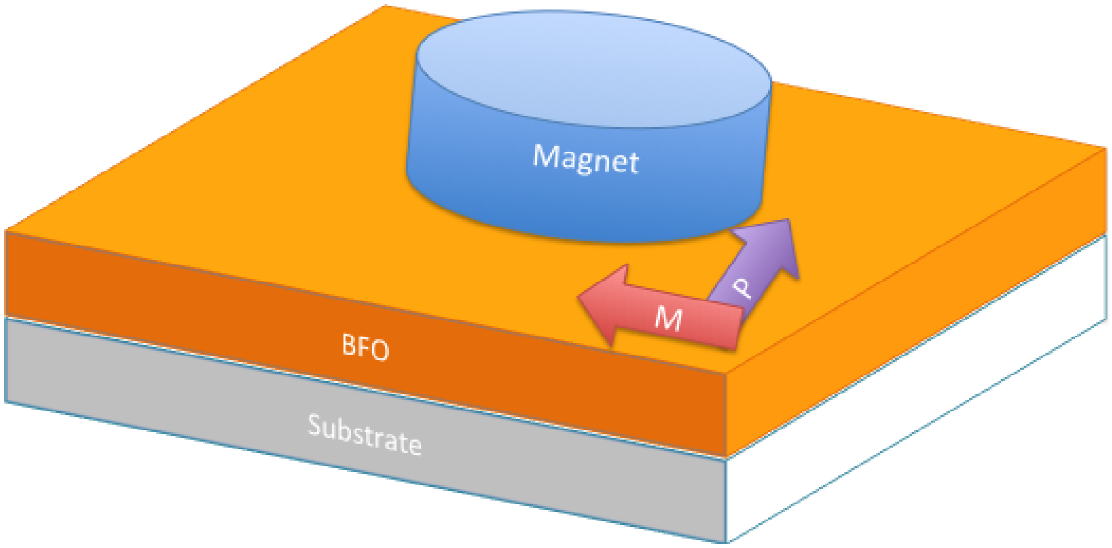

Figure 6.1: A schematic of the device structure. A thin film of BFO is grown on a substrate. A CoFeB magnet is patterned on BFO and used as a top electrode. When a voltage pulse is applied on the electrode, the polarization in the multi-ferroic material switches, and with it, the magnetic moment in the ferromagnet switches.

The BFO unit cell is rhombohedral with eight possible polarization orientations. When a vertical electric field is applied, the polarization switches by the reversal of one, two, and three components of the polarization on the (001), (110), and (111) surfaces respectively.

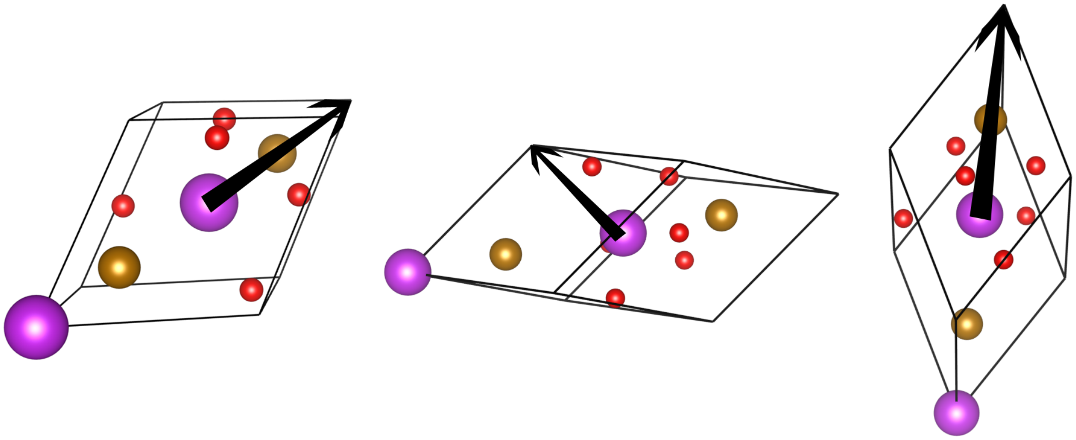

Figure 6.2: The relative orientations of the polarization on the (a) (001), (b) (110), and (c) (111) surfaces of BFO.

The ferroelectric device is studied using a phase field model. A phase field model describes the thermodynamic free energy of a system in terms of a continuous field variable. For our ferroelectric system, the contributing factors to the system energy were chemical energy, electrostatic energy, elastic energy, domain wall energy and thermal energy. Once all of these energies are taken into account, the temporal evolution of the system is then calculated with the time-dependent Ginzberg-Landau equation. The details can be found in ref. [3].

6.3 Multidomain Hysteresis

A monodomain calculation of the BFO thin film overestimates the coercive field by an order of magnitude. This is because in real ferroelectrics, switching is thermally activated at the domain wall boundary. Inclusion of domain walls in the film reduces the coercive field at the wall. When an electric field is applied, switching begins at the nucleation center located randomly on a domain wall. The domain then grows under the applied field. A multidomain calculation including strain and electrostatic energy shows excellent agreement with the shape and coercive field of the hysteresis loop. Agreement between the calculated and experimental coercive fields indicates that the BFO thin film is multidomain. The almost square hysteresis loops of BFO in a multidomain configuration is an indication that the domain switching speed in BFO is significantly high compared to the voltage ramp rate. Also the coercive field increases gradually from (001) to (110) to the (111) surface.

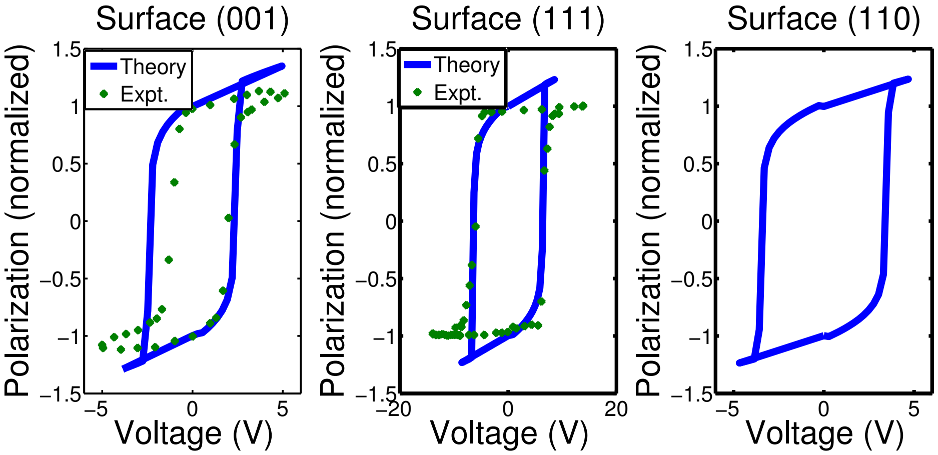

Figure 6.3: Coercive Field: Multi-domain phase field simulation of the polarization vs. voltage loop of BFO on (a) (001), (b) (110), and (c) (111) surfaces. Experimental data on the (001) and (111) surfaces are shown for comparison. Multi-domain calculation shows excellent agreement with the experimental coercive field.

6.4 AFM induced switching

Domain growth velocity under an electric field is difficult to characterize since in a multidomain film, the initial distribution of the domains and their coupled dynamics is a complex process. A popular method of estimating the domain wall velocity is to apply a local voltage using an AFM tip. The radius of the single switched domains after varying length of the voltage pulse can be measured to obtain an estimation of the domain wall velocity under the applied voltage. A simulation of an AFM switched domain is shown with the PFM image of an experimentally switched domain. The circular growth of the simulated domain is due to the hemispherical potential profile induced by the AFM tip that is used to switch the domain. Initially a cylindrical vertical domain is nucleated under the AFM that switches all the way to the bottom electrode. Subsequently, the domain grows radially outward. The switching speed is mainly determined by the speed of this radial growth of the domain.

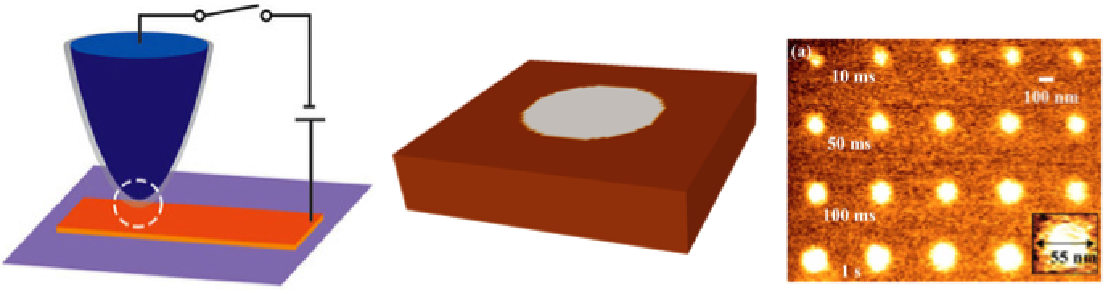

Figure 6.4: Switching of the ferroelectric domains in (a) simulation and (b) experiment. The voltage is applied using an AFM tip.

.

6.5 Domain velocity and activation field

Experimentally observed domain evolution shows a highly nonlinear behavior as shown in Fig. 6.5. We calculated the domain diameter as a function of time at different applied voltages. On the (001), (110) and (111) surfaces, the polarizaion has to switch one, two and three components respectively. The speed of the domain wall increases from (001) to (110) to (111). The switching speed is calculated in arbitrary time scale. The phase field model describes the domain dynamics at a diffusive limit. The exact switching speed depends on the dimensionality, material parameters and boundary conditions. Thus it is not possible to calculate the switching speed in an ab-initio method. However, the speed can be extracted from the experimental data. The experimental data shown in Fig. 6.5 is in the millisecond regime. Here, the switching is performed at an adiabatic limit. The intrinsic switching in ferroelectrics can be significantly faster. Picosecond switching has been reported in other ferroelectric materials [6]. The polarization dynamics and magneto-electric coupling at this time scale remain to be understood.

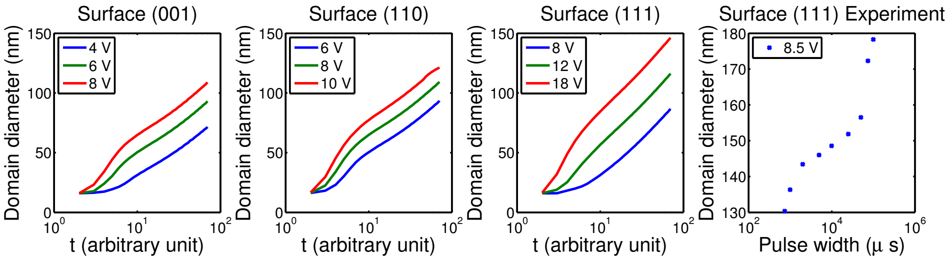

Figure 6.5: Domain Wall Velocity: The simulated domain wall velocity as a function of electric field is calculated on the (a) (001), (b) (110), and (c) (111) surfaces of BFO. (d) The experimental domain diameter as a function of the pulse width is also shown. The voltage was applied using an AFM tip. As expected, the domain wall velocity increases with increasing applied field on all the surfaces. The functional behavior of the experimental curve on the (111) surface shows resemblance to the high voltage growth in (c).

Domain wall switching in multi-domain ferroelectrics is an activated process that is qualitatively described by Merzs law. Here, we have used an atomistic description of the domain wall velocity as shown in Fig. 6.6. For these plots, the electric field for each time step was calculated as the vertical field from the AFM tip at the moving domain wall boundary position. The activation energy for domain propagation is a maximum on the (111) surface shown in Fig. 6.6(c). Experimental data on the (111) surface from Ref. [5] is also shown for comparison and shows qualitative agreement with the simulated domain growth. The domain wall velocity increases exponentially with the increase of the applied field. Also at the same applied field, the domain wall velocity is higher for higher applied voltage. This result is not directly evident from Merzs law. This trend is seen in the experimental data as well. Our multi-scale model is able to capture this effect since the inhomogeneous electric field is included in the calculation. With increasing applied voltage, the lateral component of the electric field increases and thus the domain wall velocity is higher for higher applied voltages.

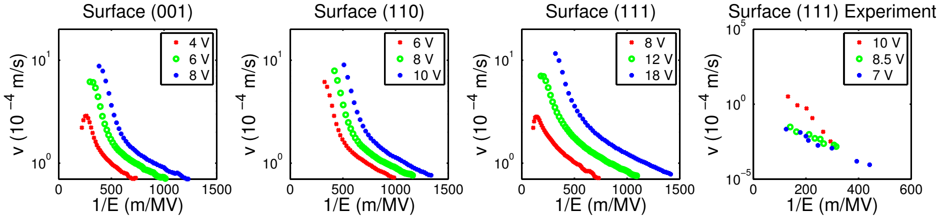

Figure 6.6: Activation Barrier: The domain wall velocity as a function of electric field is calculated for the (a) (001), (b) (110), and (c) (111) surfaces of BFO. (d) The experimental domain wall velocity versus the applied electric field is also shown for comparison. Although, the experimental velocity changes by almost five orders of magnitude, the general trend of the velocity scaling with applied field is captured in the simulation results.

6.6 Coercive Field and Switching Energy

We calculated the coercive voltage of a 40nmX40nm island with varying thickness. We find that the voltage scaling shows almost linear trend as a function of island thickness. The coercive voltage of (111) surface is higher than the (001) surface for all the thickness ranges. The switching field for the mono-domain sample is higher than any multi-domain sample. Note that the slope of the voltage versus thickness curve increases with increasing coercive voltage. The slight nonlinearity of the voltage scaling arises from the inhomogeneous electric field present in the device during switching. The almost linear scaling of coercive voltage with thickness is an indication that at the nanoscale, BFO retains its polarization. This is due to the significantly lower strain to polarization coupling in BFO compared to other ferroelectrics like PbZrxTi1-x03. The coercive voltage shown in Fig. 6.7(a) is at the adiabatic limit. Fig. 6.7(b) shows the switching time versus the applied voltage for the multi-domain (001) BFO at 25nm thickness. For a voltage change of 10 times from 1V to 12 V, the switching time decreases by 30 times from 320 to 10 in arbitrary units. Although this is more than an order of magnitude reduction in switching time, still comparison to experiment would predict a switching time in the microsecond regime. Notably, picosecond switching has been demonstrated in ferroelectric materials [6]. Our calculations show that dynamics at these short time scales cannot be fully domain wall mediated and it is a question that remains to be explored. Finally, we show the switching energy versus thickness for the 40nmX40nm island as shown in Fig 6.7(c). At the adiabatic limit, the switching energy is 0.6 J/m2 for the (001) multi-domain device at 25nm thickness. When a monodomain (111) device is used, the switching energy increases to 5 J/m2. This is to be compared with the most optimized result in spin transfer torque device where magnetic switching with areal energy density of 30 J/m2 has been demonstrated [7]. Note that the two curves in Fig. 6.7(c) provide two limiting cases in terms of switching speed. For the green curve, the switching energy is very small but the speed is also very slow. On the other hand, for the blue plot, the switching could be very fast (¡100 ps [6]), but it comes at the cost of increased energy. Nonetheless, even at this increased energy, high speed limit, the dissipation is almost an order of magnitude smaller than a highly optimized STT device [7]. Further optimization of energy-delay metric could be possible by appropriately doping BFO that reduces its coercive field while retaining the magnetic moment.

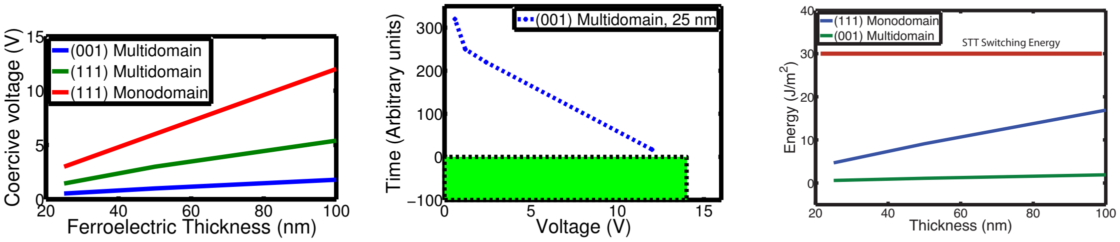

Figure 6.7: Coercive voltage scaling and energy dissipation in a nanoisland: (a) The scaling of coercive voltage as a function of film thickness. Coercive voltage shows almost linear

scaling with film thickness. (b) Decrease of switching with increasing applied voltage. Within the range of simulation time, the voltage increases by more than 10 times for speed increase of 20 times. (c) Switching energy versus thickness for (001) multidomain and (111) monodomain BFO. Only 0.6 J/m2 is dissipated for adiabatic switching on (001) surface 25nm thick device. The switching energy increases to about 5 J/m2 for fast switching in (111) monodomain sample at 25 nm thickness.

6.7 Conclusion

In conclusion, we have shown that a phase field calculation of multidomain switching process predicts the correct experimental coercive field of thin film BiFeO3. Also a lateral electric field distribution due to an AFM tip qualitatively describes the experimental domain wall velocity for a range of applied fields. We show that in scaled nanoscale islands, the coercive voltage is reduced significantly and the polarization in the film is retained due to the low strain-polarization coupling in BFO. Finally, for the first time, that the estimated per unit area energy dissipation in these devices can be more than one order of magnitude lower compared to the alternative magnetic switching routes like the spin transfer torque devices at the adiabatic limit. Further understanding of switching at high fields is necessary and is currently under investigation.

Chapter 7

Domain Dislocation Interaction

7.1 Introduction

Domain wall mobility and morphology are directly impacted by their surrounding environment (i.e., local microstructure and chemistry) [25]. In ferroelectric materials in particular, dislocations have been linked to local changes in polarization stability, acted as pinning sites for domain wall motion [2, 26, 21, 16, 22], and have also impacted nucleation events for polarization reversal [46]. Because real devices inevitably contain various defects, as well as complicated domain patterns, deviations from theoretical switching behavior can occur due to the influence of 0- and 1-dimensional defects, and their resulting strain. In this chapter, phase field model of domain dynamics under a lateral electric field and its interaction is studied. The results are compared with dynamic TEM measurements. This combinatory approach to study BFO domain evolution in electric field is the first direct, quantitative measurement of the role of localized strain components (tensile and compressive) in domain relaxation behavior. The work presented in this chapter provides insight into dynamics of real device systems (horizontal device structures), and reveals kinetic data on the interaction of domains with structural defects during the intermediate stages of switching, which dictate how a material will behave when operated in a device.

7.2 Theory of dislocation in phase field

Phase field modeling was performed to study the domain dynamics in BFO thin films in the presence of misfit dislocations. The method of phase field calculation incorporating long range electrostatics and elastic interactions is detailed in Ref. [1]. In this work, misfit dislocation is introduced in the inhomogeneous strain calculation using the eigen strain method. The eigen strain method is suitable for describing any space dependent dislocation distribution. For example, the eigen strain for a slip plane (n_1,n_2,n_3) and a dislocation with a Burgers vector (b_1,b_2,b_3) can be calculated as

$$\epsilon_{ij},^{0,s} = \frac{1}{2d_0}(b_i n_j + b_j n_i)\delta(x - x_0) \tag{7.1}$$

where d_0 is the interplanar distance of the slip plane. Here, x_0 lies on the slip plane. The total eigen strain due to the misfit dislocation and the polarization induced spontaneous strain can be calculated as

$$\epsilon_{ij},^{0,T} = \epsilon_{ij},^{0,P} + \epsilon_{ij},^{0,s} \tag{7.2}$$

Here, $\epsilon_{ij},^{0,P}$ is the eigen strain due to the polarization. The total strain is calculated as a body force and fed into the finite element solver to find the total displacement due to the body forces with appropriate boundary conditions. In this work, the slip planes, n= (1,0,0) or (0,1,0) and the Burgers vectors (-1,0,0), (0,-1,0) are considered respectively. The boundary conditions are those used in ref. [1].

7.3 Strain and polarization distribution around misfit dislocation

We simulated a 64nmX64nmX32nm film and studied the strain distribution around the MD. The impact of the MD on the polarization values and consequently domain wall velocity was simulated self-consistently. We introduce a misfit dislocation along the [100] direction. A compressive MD was introduced as an eigen strain resulting due to the absence of a single atomic layer on the BFO film. After relaxation of the eigen strain, tensile strain is observed to be present around the compressively strained region. The pseudocolor plot and cross cut perpendicular to the misfit dislocation in Fig. 7.1 shows the tensile strain e_{xx} distribution. Similar distributions have been observed for other longitudinal and shear strains. The maximum strain induced by the MD is 3e-3. The tensile strain induced by the compressive MD vanishes in about 5nm (10 grid points) from the MD (Fig. 7.1(b)).

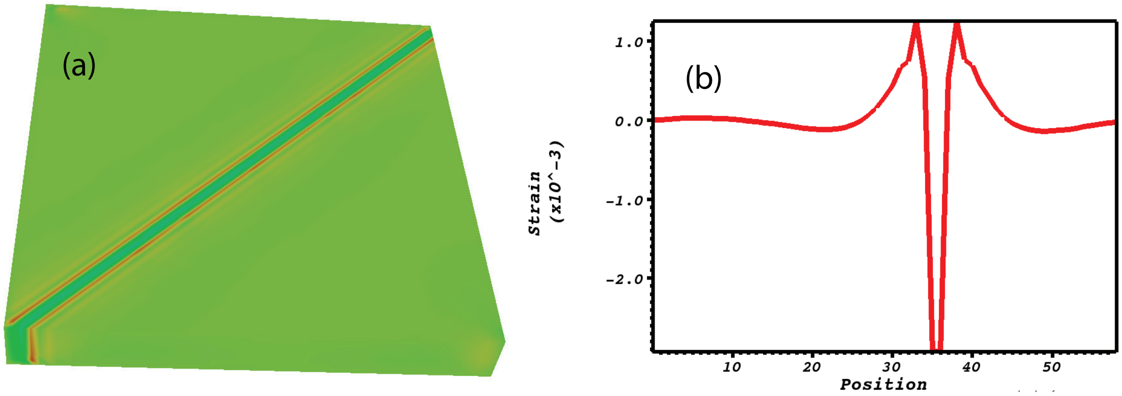

Figure 7.1: Phase field simulations of strain distribution in the BFO film due to misfit dislocation along the [100] direction. (a) The pseudocolor plot of longitudinal strain (e_{xx})

show the change in strain distribution around the misfit dislocation. (b) A cross-cut along the x direction shows the strain as a function of position. At the dislocation, there is a compressive strain. However, in the surrounding regions, the compressive misfit dislocation causes a tensile strained region.

The change in strain around the misfit dislocation causes a consequent spatial variation in the polarization. The in-plane component of the polarization (P_x here) distribution is shown in the pseudocolor in Fig. 7.2 below. Initially, when the domains start to grow from the nucleation center (the red region), the polarization variation on the MD line is clearly visible. As the nucleated domain grows under the applied field, the polarization variation around the MD gets continually washed away. This means that the applied field induced polarization along the X direction is larger than the polarization gradient caused by the MD. Turning off the electric field after 1000 time steps causes the domains to relax towards their equilibrium values. As domain relaxation occurs, the polarization variation around the MD reappears on the color plots. We take a cross cut along the Y direction to quantify the variation of the polarization due to the presence of the MD. We find that the magnitude of the variation in polarization is only $20e^{-2}$ C/m^2 as seen around position index 50 where the polarization crosses the MD Fig. 7.2(d). The in-plane polarization decreases at the compressive strain and increases at the tensile strained regions compared to the regions that are far away from the MD. We attribute this small variation to the relatively low strain polarization coupling in BFO.

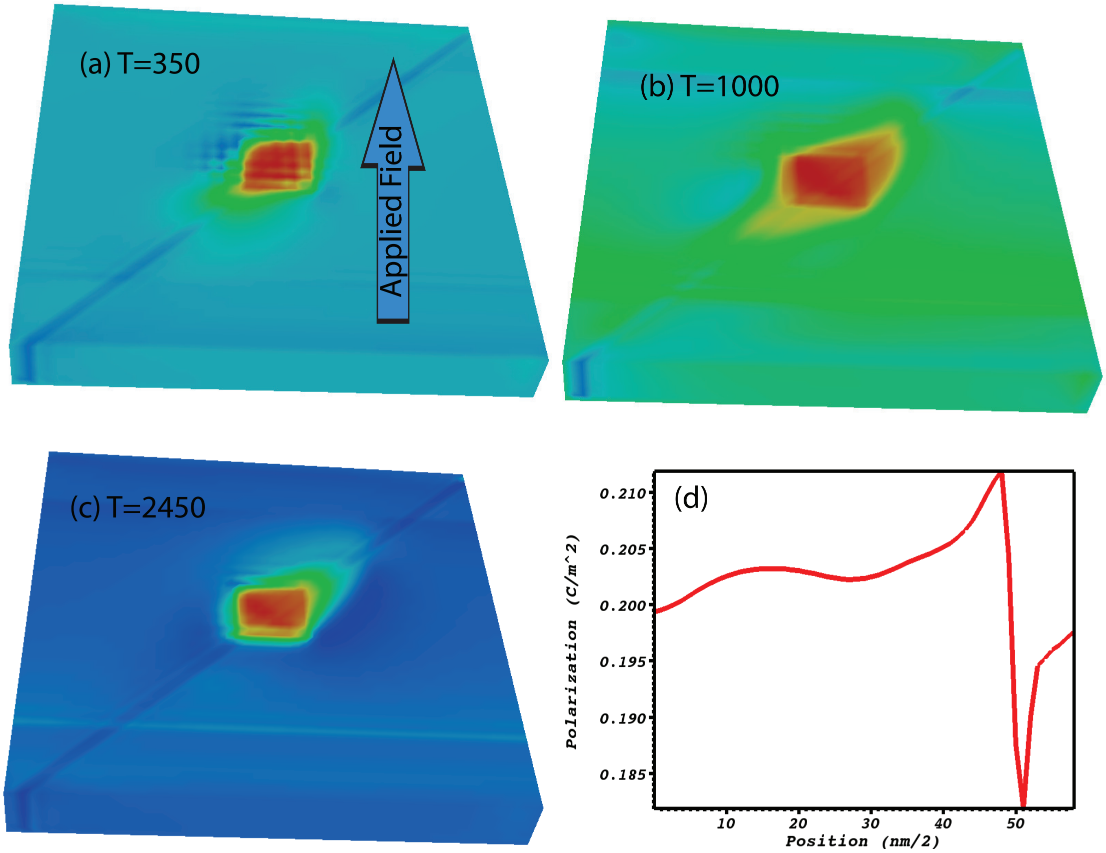

Figure 7.2: Phase field simulations of in-plane polarization (P_x) distribution in the BFO film. (a,b,c) The pseudocolor plots of (P_x) show the change in polarization distribution around the misfit dislocation at different stages of switching. The red region is the nucleated domain that is growing under the applied field. The variation of polarization around the MD is mostly visible in the early stages of application of the electric field. As the domains grow under the applied field, the polarization variation due to MD gets washed away. After the electric field is turned off, the polarization variation around the MD emerges again as the domains relax to their stable positions. Similar textures are observed for other components of the polarization. (d) The quantitative value of the polarization variation around the MD when a crosscut along the Y axis is taken. The variation in polarization around the MD is of the order of 20^{-2} C/m^2. BFO has a relatively low strain-polarization coupling that is responsible for relatively low modulation of polarization values around the MD.

7.4 Effect on domain dynamics

It is interesting to ask if domain wall propagation and relaxation velocities are affected by the presence of the misfit dislocations. Experimentally, real-time imaging of the ferroelectric device under bias (plan view) enables the construction of nucleation maps covering large areas that reveal the exact location of newly formed domains, the density and sites of domain nucleation, and to isolate test cases for quantifying how domain wall propagation and relaxation velocities are affected by the presence of the dislocations in the as-grown device assembly. By comparing a set of images extracted from in situ video, before, during, and after a few hundred milliseconds after the initiation of a voltage pulse, the changes in the domain structures due to nucleation and propagation can be isolated. These nucleation maps permit visualization of the global domain nucleation behavior at a glance, as shown in Fig. **??**. The pre-bias domain configuration and area analyzed are depicted in Fig. 7.3 (1A), and the nucleation map is shown in Fig. 7.3(1B). Nucleation events are observed predominantly at the existing domain walls. The domains nucleate along existing walls which run along both the [100] and [010] direction. The nucleated domains, however, are driven primarily along the [010] direction under the applied electric field.

Before studying the effect of MD on the domain dynamics of thin film BFO with the phase field model, we identify the type of domains present in a thin film. Also which domain propagate under an applied field and which domains remain static. We apply a lateral electric field along the [110] direction of BFO crystal. We find that the domain growth is anisotropic and uniaxial under the applied field. The growth angle is 45^0 with respect to the applied field direction. The anisotropic growth of the domains occur due to the open circuit boundary condition in the film. Switched domains along the applied field causes charged domain walls. Inhomogeneous electric field is induced at these charged domain walls. The 45^0 growth of the domain is due to the crystal symmetry of BFO. The spatial arrangement of in-plane components of the domains minimizes domain wall charge when the domain grows 45^0 with respect to the applied field. We consider four possible domain configurations between background and nucleated domains shown in Fig. 7.3.

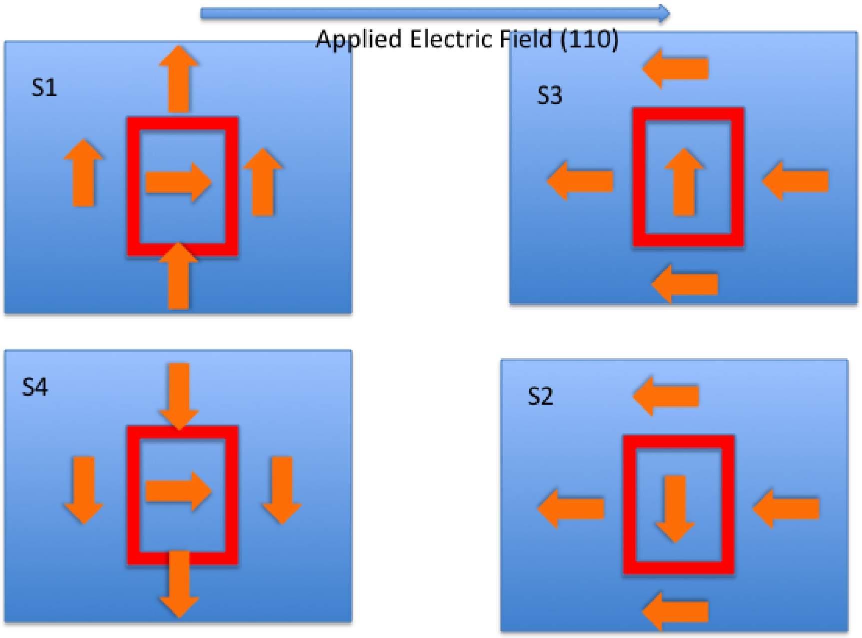

Figure 7.3: Four possible configurations of nucleated and background domain directions.

In only two combinations, the domain growth is 45^0 counter clockwise with respect to the applied field direction that is observed experimentally. Thus we are left with only two possible domain configurations as shown in Fig. 7.4. The experimental data suggests that the domain growth is 45^0 with respect to the applied field direction, however, it appears to be unidirectional rather than uniaxial. In order to rule out the effect of mobile charges injected at the negative electrode, we simulated the same system with a 5nm layer of negatively charged region. Inclusion of negative charges didnt change the observed result.

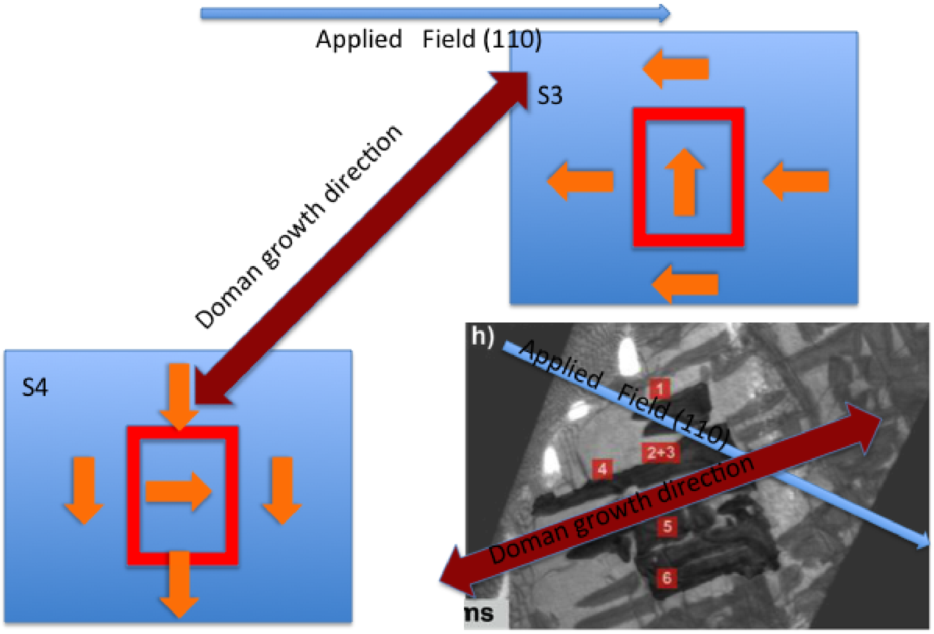

Figure 7.4: Application of an electric field along the [110] crystal direction of BFO causes the domains to grow at 135^0 with respect to the applied field direction. Only the configurations S3 and S4 shows growth along the 135^0 of the electric field. The other two configurations show domain growth at 45^0 with respect to the field. Thus we conclude that only domain configurations of S3 and S4 are present in the film.

In order to investigate the interaction of domain propagation with the misfit dislocation, we placed a single layer compressively strained misfit dislocation running along the [010] direction. The method of calculating inhomogeneous strain due to misfit dislocation is given in the supplementary information. To initiate domain nucleation and propagation, a lateral electric field was applied along the [110] direction. The magnitude of the electric field was 200 kV/cm. Fig. 7.5(3a) depicts the initial conditions of the phase field simulations before application of the electric field. The electric field is applied for 1600 time steps (Fig. 7.5(3b)). The existing domain is observed propagating due to the influence of the electric field. Additionally, a new domain is nucleated at the compressive MD. Presence of compressive misfit dislocation on the BFO film reduces the domain wall switching energy. It becomes favorable for the domains to nucleate at the misfit dislocation. The propagation velocity of the existing domain increases closer to the MD. After an additional 700 time steps (Fig. 7.5(3c)), the two domains coalesce into a single domain when the existing domain propagates into the MD. Phase field simulations of a system without any misfit dislocations but with otherwise identical conditions do not exhibit the nucleation event which occurs at the MD in Fig. 7.5(3b). In order to study the domain relaxation, the applied field is turned off after 1600 time steps. We find that the relaxation velocity of domains is increased in the vicinity of the MD as was the case with the domain growth velocity. Because the time scale is arbitrary in the phase field simulations, only qualitative observations of domain velocities are possible. Domain velocities are qualitatively slower in the vicinity of tensile MDs, opposite the case of compressively strained MDs. Additionally, no new domains nucleate at tensile MDs under the same applied field as those in the compressive MD studies. It is only when the existing domain propagates into the tensile MD that a new domain is nucleated under the thermodynamic pressure of the incoming domain.

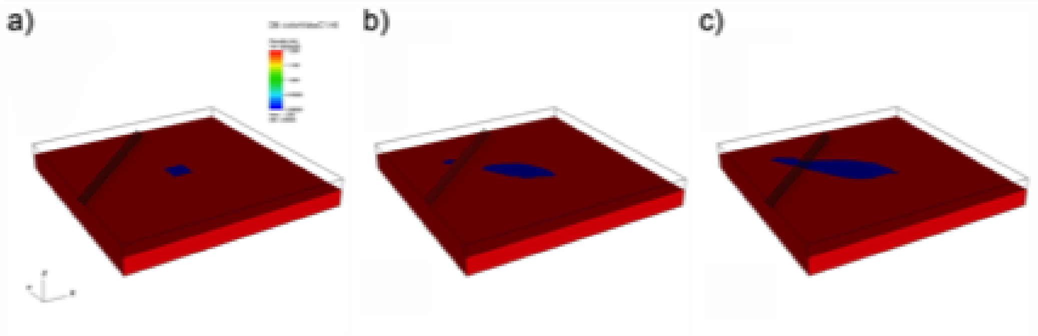

Figure 7.5: Phase field simulations indicate that compressive misfit dislocations (add to figure later) encourage newly forming ferroelectric domains to nucleate at the MD, ahead of any propagating domains which are already contained within the film.

In order to investigate domain propagation along the MD, we simulate the domain wall propagation in the same configuration as described above, introducing a MD along the [100] direction rather than the [010] direction as shown in Fig. 7.6(a-d). The direction of the applied field and the configuration of the nucleated domains is such that the domain grows along the MD. The qualitative pattern of the growth is the same as for the MD along the [010] direction. However, the domain wall velocity close to the MD is qualitatively different for the two cases. In the case of [010] MD, new domains nucleated at the MD. When the propagating domain nears the nucleated domain, the proximity of two growing domains increases the domain wall velocity close to the MD. On the other hand, for [100] MD, no new domain is nucleated. The initially nucleated domain grows along the MD. Our simulation results show that the domain wall growth and subsequent relaxation is slower for films in which MD is present compared to defect free films. The trend in the reduction of domain wall velocity with MD is further proved by the introduction of an artificial 5 atomic layer MD shown in 7.6(e). We find that the domain wall velocity systematically reduces in the presence of increasing compressively strained MD. As we have shown above, the presence of compressively strained MD causes tensile strained regions around the MD. Tensile strain increases the domain switching field when the polarization is switching in-plane from $+\mathrm{P}_x$ to P_x through a 71^0 switch of the polarization. Consequently the domain wall speed is reduced on the MD, when the growth of the domain is along the MD.

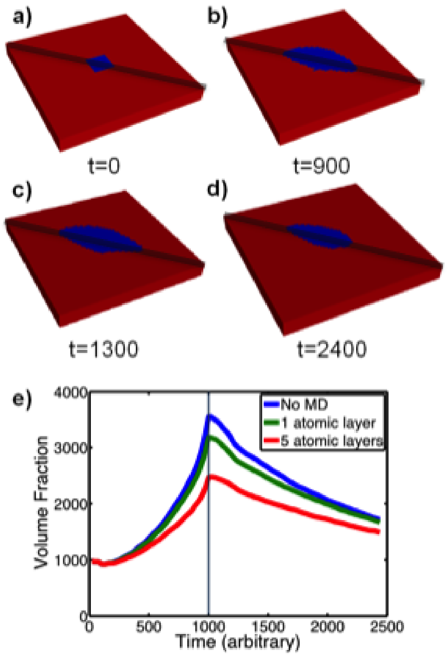

Figure 7.6: The dynamic behavior of the domains as a function of strain due to misfit dislocation. An electric field was applied from 100 to 1000 time steps. (a-d) Color plot of a nucleated domain on the single atomic layer misfit dislocation. The domain initially grows along the misfit dislocation (up to 1000 time steps) and then relaxes as the applied field is removed (up to 2450 time steps here). (B) Both the domain growth rate under the applied field and domain relaxation are slower as single atomic layer misfit dislocation is introduced. Introduction of an artificial 5 layer misfit dislocation reduces the domain wall velocity further confirming the trend that increased compressive misfit dislocation reduces the domain growth and relaxation when the domain is growing along the misfit dislocation.

7.5 Conclusion

Phase filed model of domain propagation under lateral electric field shows qualitatively different behavior for tensile and compressive MD. For a compressive MD, coercive field decreases close to the MD, when the domain is propagating perpendicular to the MD. Thus enhanced nucleation is observed close to these defect types. However, the domain propagation velocity decreases when the domain is propagating along the compressive MD due to the presence of tensile strain around a compressive MD. Opposite behavior is observed for tensile MD. These simulation results are further corroborated by experimental results.

Chapter 8

Conclusion and Future Work

8.1 Introduction

In this chapter, we summarize our results presented in various chapters of this thesis. Then we make relevant suggestions for future work both in terms of physical modeling and numerical efficiency. We also identify some experiments that needs to be performed in order to benchmark and verify these models. We also mention some bottlenecks in understanding these physical phenomena.

8.2 Summary of the Results Presented

In summary, we have studied various aspects of ferroelectric domain switching and magnetic energy scales using the multi-ferroic material bismuth ferrite as a prototype material. In this pursuit, we have developed a massively parallel phase field code that can take arbitrary electrical and mechanical boundary conditions into account. The results presented in this thesis is summarized here:

1. We have proposed a novel method of determining the anti-ferromagnetic surface magnetic moment in an AFM-FM interface. The calculation of angular coercive field of the coupled system and a hysteresis measurement at a critical angle provides a way to estimate the surface magnetic moment density that could be elusive from easy axis hysteresis measurement alone. In the case of BFO, we found the surface magnetic energy to be strong enough to cause FM reversal in the case of reversal of AFM order parameter. Also, we predicted a very high surface magnetic moment present at the BFO-CoFeB interface, that has been observed experimentally.
2. We elucidated the 180^0 switch of the domain pattern of BFO underneath a magnet. Our model showed that, electrostatic interaction between polarization domains cause high repulsion at the domain wall. Application of an electric field cause a 71^0 switch of one variant of the domain. Head to head polarization configuration cause highly

unstable domain walls. Driven by this instability, the polarizations go through a second switching process. Thus although the polarization in individual domain switch by 90^0, the overall domain pattern switch by 180^0.

3. Application of a localized vertical electric field cause a 180^0 switch of the domain pattern. The switching of the first polarization cause highly strain mismatched domains at the edge of the switching region. The symmetry of BFO is such that 180^0 in-plane switch of the polarization cause the switched domains to become strain compatible with the surrounding domains. Thus application of a vertical electric field cause the vertically switched domains to go through a second in-plane switch.

4. Domain reconstruction during polarization reversal is a significant problem for achieving reliable switching. However, it has been difficult to control domain pattern during switching. The problem arises from the anisotropic strain applied on the substrate that causes the coercive voltage to be different for the two domains. In order to suppress domain reconstruction, the field has to be applied in a way so that the lateral applied field is smaller for the domain that has lower coercive field. For an applied field that is perfectly symmetric with respect to the two polarization domains, there occurs a frustrated condition for switching from initial to the final polarization direction as the probability of switching in either directions are the same. Thus we find that for an applied field that is orthogonal to the domain walls cannot move the walls during switching and no domain size reconstruction takes place in strain less thin films. For a strained film, the appropriate angle for applied field can be calculated using the principle mentioned here.

5. BFO is a candidate material for electric field induced switching of magnets. We predicted the switching energy of a scaled BFO island including all the relevant physical interactions. We found that at a reasonable scaled device, BFO can switch at an order of magnitude lower energy compared to the state of the art STT device at the adiabatic limit.

6. The quantitative calculation of domain switching speed has been difficult because of the difficulty with including the thermal effects. In this work, we have simulated real device structures to predict the electric field versus domain wall velocity curve. We have elucidated the importance of the boundary conditions in determining the shapes of these curves.

7. Misfit dislocations present in ferroelectric samples cause the domain wall propagation velocity to vary from their usual values. We showed that compressive MDs act as nucleation site whereas tensile strain prohibit domain nucleation during switching when the domain is propagating perpendicular to the MD. A different physical effect is observed for domains propagating along the MD. The tensile strain caused by the compressive MD, reduce the domain wall velocity. These predictions have been confirmed experimentally later.

8.3 Future Work

There are a number of directions where the present work needs to be extended. Understanding the microscopic mechanism of domain switching and being able to make quantitative predictions at the device level is the crux of the problem that we believe will occupy the research efforts in the future. We enumerate some related work that needs to be performed in route to achieving this goal.

1. The primary advantage of the phase field model is that it incorporates the domain dynamics naturally, thus provides a simple implementation of moving wall without having to apply a moving grid. The model is best suited for the study of domain dynamics in ferroelectric and ferromagnetic systems. Currently, the thermodynamic parameters of the materials are mostly measured experimentally. Since these parameters are mostly equilibrium measurements, they could also be calculated from first principle. The introduction of first principle calculation will allow the model to be much more predictive and also it can be used for the design of new devices incorporating materials for which the experimental data is not available yet. Another possible extension is to incorporate the mobile charge and band structure effects. First principle or tight binding methods could be used to implement these components of the simulator. Once these extensions have been made, a transport simulator could be added to understand semiclassical and tunneling transport in these systems.

2. Couple with a magnetization dynamics simulator.

3. Numerical: In the current model, we have used a uniform grid for domain dynamics. However, most of the interesting dynamics takes place at the domain wall. Hence this type of problems are naturally suited for adaptive grids. A high density of grid points at the domain wall and coarser grid within the domain will make the simulation run significantly faster.

4. BFO experiment: At this moment, there is lack of experimental data on the switching speed of BFO. More experimental studies of domain velocity as a function of electric field on various surfaces needs to be performed.

5. Multi-scale model of switching dynamics with boundary condition:
   The domain switching kinetics in ferroelectrics have been an unsolved issue till this day. The early theory for domain wall dynamics as a function of the applied field was proposed by W. Merz who viewed the switching process as a thermally activated process. Later, Miller and Weinreich proposed a model of domain nucleation and movement governed by creation of a triangular area at the wall. Although the model explained many qualitative features of the experimental observation, the quantitative value of the activation energy calculated from the Miller-Weinreich theory was two orders of magnitude higher than that observed in experiment. In order to understand this discrepancy,

Y. Shin et al., performed multiscale modeling of domain dynamics in small ferroelectric system. There study started from calculating the energetics from first principle, deriving a reduced representation using valence-bond method and then applying Monte Carlo simulation to calculate the thermal effects. They studied the domain dynamics at high field and projected it to the range where experiments are performed and found excellent agreement with the experiments. However, no information about the effect of boundary conditions were reported. Experimentally, it has been observed that in thin film ferroelectrics, the switching is dependent on the thickness of the film. Usually, thermal excitation is believed to be the cause for the variation of the domain wall velocity. However, using our phase field model, we found that the boundary condition at the electrode could also change the switching speed significantly as shown in Fig. 8.1. The incorporation of inhomogeneous charge that arise in a ferroelectric during switching increases the domain wall velocity significantly.

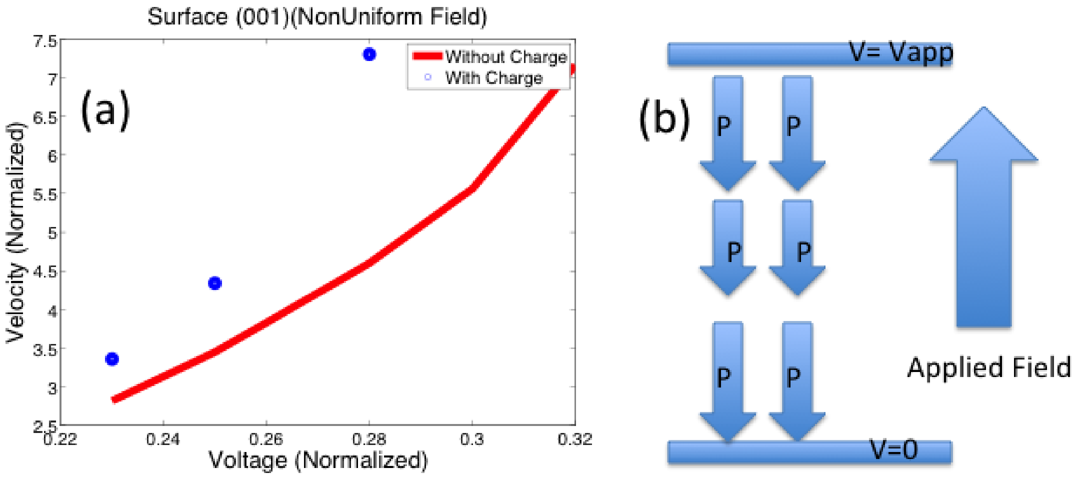

Figure 8.1: Evolution of the polarization on the (001) surface with an open boundary condition when a field is applied along the [100] direction without considering the domain wall charge. (a) The initial domain pattern with a defect introduced where the switching starts. (b) Isotropic growth of right oriented polarization domain (dark blue) through a 71° switch of the left polarization (light blue) along the applied field direction.

Similar variation of domain wall velocity with film thickness has been observed in AFM tip induced switching as well. Our modeling shows that the variation could be due to the change in lateral component of the electric field as the thickness of the film is varied.

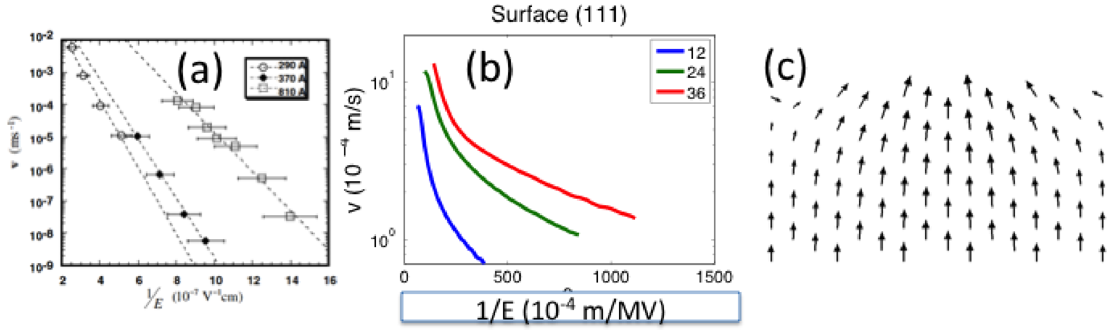

Figure 8.2: Evolution of the polarization on the (001) surface with an open boundary condition when a field is applied along the [100] direction without considering the domain wall charge. (a) The initial domain pattern with a defect introduced where the switching starts. (b) Isotropic growth of right oriented polarization domain (dark blue) through a 71° switch of the left polarization (light blue) along the applied field direction.

In conclusion, preliminary studies show that the boundary conditions and inhomogeneous charge significantly effect the domain wall velocity and thickness dependent variation. More systematic studies of these effects will be a subject for future study.

Bibliography

[1] Rajeev Ahluwalia et al. “Domain-size dependence of piezoelectric properties of ferroelectrics”. In: *Phys. Rev. B* 72 (1 2005), p. 014112. DOI: `10.1103/PhysRevB.72.014112`. URL: `http://link.aps.org/doi/10.1103/PhysRevB.72.014112`.

[2] S. P. Alpay et al. “Can interface dislocations degrade ferroelectric properties?” In: *Appl. Phys. Lett.* 85 (2004), p. 2044.

[3] Satish Balay et al. “PETSc Web page”. In: (2011). http://www.mcs.anl.gov/petsc.

[4] Nina Balke et al. “Direct Observation of Capacitor Switching Using Planar Electrodes”. In: *Adv. Func. Mater.* 20.20 (2010), pp. 3466–3475. ISSN: 1616-3028. DOI: `10.1002/adfm.201000475`. URL: `http://dx.doi.org/10.1002/adfm.201000475`.

[5] H. Béa et al. “Mechanisms of Exchange Bias with Multiferroic $BiFeO_3$ Epitaxial Thin Films”. In: *Phys. Rev. Lett.* 100.1 (2008), p. 017204. DOI: `10.1103/PhysRevLett.100.017204`.

[6] H. Béa et al. “Tunnel magnetoresistance and robust room temperature exchange bias with multiferroic BiFeO[sub 3] epitaxial thin films”. In: *Applied Physics Letters* 89.24, 242114 (2006), p. 242114. DOI: `10.1063/1.2402204`. URL: `http://link.aip.org/link/?APL/89/242114/1`.

[7] C. Binek. “Exchange bias in generalized Meiklejohn-Bean approach”. In: *J. Magn. Magn. Mater.* 234 (2001), p. 353.

[8] Julio Camarero et al. “Origin of the Asymmetric Magnetization Reversal Behavior in Exchange-Biased Systems: Competing Anisotropies”. In: *Phys. Rev. Lett.* 95.5 (2005), p. 057204. DOI: `10.1103/PhysRevLett.95.057204`.

[9] Long-Qing Chen. “Phase-Field Method of Phase Transitions/Domain Structures in Ferroelectric Thin Films: A Review”. In: *J. Am. Ceram. Soc.* 91.6 (2008), pp. 1835–1844. ISSN: 1551-2916. DOI: `10.1111/j.1551-2916.2008.02413.x`. URL: `http://dx.doi.org/10.1111/j.1551-2916.2008.02413.x`.

[10] L.Q. Chen and Jie Shen. “Applications of semi-implicit Fourier-spectral method to phase field equations”. In: *Comp. Phys. Commun.* 108.2-3 (1998), pp. 147 –158. ISSN: 0010-4655. DOI: `10.1016/S0010-4655(97)00115-X`. URL: `http://www.sciencedirect.com/science/article/pii/S001046559700115X`.

[11] S. Choudhury, L. Q. Chen, and Y. L. Li. "Correlation between number of ferroelectric variants and coercive field of lead ziconate titanate single crystals". In: *Appl. Phys. Lett.* 91.3 (2007), p. 032902. ISSN: 0003-6951. DOI: `{10.1063/1.2759274}`.

[12] Samrat Choudhury, Yulan Li, and Long-Qing Chen. "A Phase Diagram for Epitaxial PbZr1xTixO3 Thin Films at the Bulk Morphotropic Boundary Composition". In: *J. Am. Ceram. Soc.* 88.6 (2005), pp. 1669–1672. ISSN: 1551-2916. DOI: `10.1111/j.1551-2916.2005.00319.x`. URL: `http://dx.doi.org/10.1111/j.1551-2916.2005.00319.x`.

[13] Ying-Hao Chu et al. "Electric-field control of local ferromagnetism using a magnetoelectric multiferroic". In: *Nat. Mater.* 7 (2008), p. 478. DOI: `10.1038/nmat2184`. URL: `http://dx.doi.org/10.1038/nmat2184`.

[14] Shuai Dong et al. "Exchange Bias Driven by the Dzyaloshinskii-Moriya Interaction and Ferroelectric Polarization at *G*-Type Antiferromagnetic Perovskite Interfaces". In: *Phys. Rev. Lett.* 103.12 (2009), p. 127201. DOI: `10.1103/PhysRevLett.103.127201`.

[15] Claude Ederer and Nicola A. Spaldin. "Weak ferromagnetism and magnetoelectric coupling in bismuth ferrite". In: *Phys. Rev. B* 71.6 (2005), p. 060401. DOI: `10.1103/PhysRevB.71.060401`.

[16] P. Gao and et al. "Revealing the role of defects in ferroelectric switching with atomic resolution". In: *Nat. Commun.* 2 (2011), p. 591.

[17] J. Geshev, L. G. Pereira, and J. E. Schmidt. "Angular dependence of the exchange bias obtained from magnetization and ferromagnetic measurements in exchange-coupled bilayers". In: *Phys. Rev. B* 64 (2001), p. 184411.

[18] J. T. Heron. "Electric field control of ferromagnetism and magnetic devices using multiferroics". In: *PhD. Thesis* (2013). DOI: `http://escholarship.org/uc/item/2gq451g7`.

[19] J. T. Heron et al. "Electric-field-induced magnetization reversal in a ferromagnet-multiferroic heterostructure". In: *Phys. Rev. Lett.* 107 (2011), p. 217202.

[20] Hong-Liang Hu and Long-Qing Chen. "Computer simulation of 90 ferroelectric domain formation in two-dimensions". In: *Mater. Sci. Engg. A* 238.1 (1997), pp. 182 –191. ISSN: 0921-5093. DOI: `10.1016/S0921-5093(97)00453-X`. URL: `http://www.sciencedirect.com/science/article/pii/S092150939700453X`.

[21] S. Y. Hu, Y. L. Li, and L. Q. Chen. "Effect of interfacial dislocations on ferroelectric phase stability and domain morphology in a thin filma phase-field model". In: *J Appl Phys* 94 (2003), p. 2542.

[22] S. V. Kalinin and et al. "Defect-mediated polarization switching in ferroelectrics and related materials: from mesoscopic mechanisms to atomistic control". In: *Adv Mater* 22 (2010), p. 314.

[23] D. Lebeugle et al. "Exchange coupling with the multiferroic compound $BiFeO_3$ in antiferromagnetic multidomain films and single-domain crystals". In: *Phys. Rev. B* 81.13 (2010), p. 134411. DOI: `10.1103/PhysRevB.81.134411`.

[24] J.-H. Lee et al. "Multiferroic properties of epitaxially stabilized hexagonal DyMnO[sub 3] thin films". In: *Applied Physics Letters* 90.1, 012903 (2007), p. 012903. URL: `http://link.aip.org/link/?APL/90/012903/1`.

[25] K. Lee and S Baik. "Ferroelastic Domain Structure and Switching In Epitaxial Ferroelectric Thin Films". In: *Ann Rev Mater Res* 36 (2006), pp. 81–116.

[26] Y. L. Li and et al. "Influence of interfacial dislocations on hysteresis loops of ferroelectric films". In: *J Appl Phys* 104 (2008), p. 104110.

[27] Y. L. Li and L. Q. Chen. "Temperature-strain phase diagram for $BaTiO_3$ thin films". In: *Appl. Phys. Lett.* 88.7, 072905 (Feb. 2006), p. 072905. DOI: `10.1063/1.2172744`.

[28] Y. L. Li, S. Y. Hu, and L. Q. Chen. "Ferroelectric domain morphologies of (001) $PbZr1\text{-}xTixO_3$ epitaxial thin films". In: *J. Appl. Phys.* 97.3 (Feb. 2005), p. 034112. DOI: `10.1063/1.1849820`.

[29] Y. L. Li et al. "Phase-field model of domain structures in ferroelectric thin films". In: *Appl. Phys. Lett.* 78, 3878 (June 2001), p. 3878. DOI: `10.1063/1.1377855`.

[30] Y. L. Li et al. "Phase transitions and domain structures in strained pseudocubic (100) $SrTiO_3$ thin films". In: *Phys. Rev. B* 73 (18 2006), p. 184112. DOI: `10.1103/PhysRevB.73.184112`. URL: `http://link.aps.org/doi/10.1103/PhysRevB.73.184112`.

[31] Y.L. Li et al. "Effect of substrate constraint on the stability and evolution of ferroelectric domain structures in thin films". In: *Acta Materialia* 50.2 (2002), pp. 395 – 411. ISSN: 1359-6454. DOI: `10.1016/S1359-6454(01)00360-3`. URL: `http://www.sciencedirect.com/science/article/pii/S1359645401003603`.

[32] Axel Lubk, S. Gemming, and N. A. Spaldin. "First-principles study of ferroelectric domain walls in multiferroic bismuth ferrite". In: *Phys. Rev. B* 80.10 (2009), p. 104110. DOI: `10.1103/PhysRevB.80.104110`.

[33] A. P. Malozemoff. "Random-field model of exchange anisotropy at rough ferromagnetic-antiferromagnetic interfaces". In: *Phys. Rev. B* 35.7 (1987), pp. 3679–3682. DOI: `10.1103/PhysRevB.35.3679`.

[34] Lane W. Martin et al. "Nanoscale Control of Exchange Bias with BiFeO3 Thin Films". In: *Nano Letters* 8.7 (2008). PMID: 18547121, pp. 2050–2055. DOI: `10.1021/nl801391m`. eprint: `http://pubs.acs.org/doi/pdf/10.1021/nl801391m`. URL: `http://pubs.acs.org/doi/abs/10.1021/nl801391m`.

[35] C. W. Nan et al. "Multiferroic magnetoelectric composites: Historical perspectives, status and future works." In: *J. of Appl. Phys.* 103.3 (2008).

[36] Florin Radu and Hartmut Zabel. "Exchange Bias Effect of Ferro-/Antiferromagnetic Heterostructures". In: Springer Tracts in Modern Physics 227 (2008). Ed. by Hartmut Zabel and Samuel Bader, pp. 97–184. DOI: `10.1007/978-3-540-73462-8_3`. URL: `http://dx.doi.org/10.1007/978-3-540-73462-8_3`.

[37] W.-F. Rao and Y. U. Wang. "Bridging domain mechanism for phase coexistence in morphotropic phase boundary ferroelectrics". In: *Appl. Phys. Lett.* 90.18, 182906 (Apr. 2007), p. 182906. DOI: `10.1063/1.2736276`.

[38] S. Semenovskaya and A. G. Khachaturyan. "Development of ferroelectric mixed states in a random field of static defects". In: *J. App. Phys.* 83 (1998), pp. 5125–5136. DOI: `10.1063/1.367330`.

[39] S Semenovskaya and AG Khachaturyan. "Ferroelectric transition in a random field: Possible relation to relaxor ferroelectrics". In: *Ferroelectrics* 206.1-4 (1998), pp. 157–180. DOI: `10.1080/00150199808009157`.

[40] Y. Shiota et al. "Induction of coherent magnetization switching in a few atomic layers of FeCo using voltage pulses." In: *Nat. Mater.* 11.1 (2012), pp. 39–42.

[41] A. K. Soh, Y. C. Song, and Y. Ni. "Phase Field Simulations of Hysteresis and Butterfly Loops in Ferroelectrics Subjected to Electro-Mechanical Coupled Loading". In: *J. Am. Ceram. Soc.* 89.2 (2006), pp. 652–661. ISSN: 1551-2916. DOI: `10.1111/j.1551-2916.2005.00724.x`. URL: `http://dx.doi.org/10.1111/j.1551-2916.2005.00724.x`.

[42] D. A. Tenne et al. "Absence of low-temperature phase transitions in epitaxial $BaTiO_3$ thin films". In: *Phys. Rev. B* 69 (17 2004), p. 174101. DOI: `10.1103/PhysRevB.69.174101`. URL: `http://link.aps.org/doi/10.1103/PhysRevB.69.174101`.

[43] D. A. Tenne et al. "Probing Nanoscale Ferroelectricity by Ultraviolet Raman Spectroscopy". In: *Science* 313 (Sept. 2006), pp. 1614–1616. DOI: `10.1126/science.1130306`.

[44] Z. M. Tian et al. "Spin-glasslike behavior and exchange bias in multiferroic Bi[sub 1/3]Sr[sub 2/3]FeO[sub 3] ceramics". In: *Applied Physics Letters* 96.14, 142516 (2010), p. 142516. DOI: `10.1063/1.3383227`. URL: `http://link.aip.org/link/?APL/96/142516/1`.

[45] V. Vaithyanathan et al. "c-axis oriented epitaxial $BaTiO_3$ films on (001) Si". In: *J. Appl. Phys.* 100.2 (July 2006), p. 024108. DOI: `10.1063/1.2203208`.

[46] I. Vrejoiu and et al. "Threading dislocations in epitaxial ferroelectric PbZr 0.2 Ti 0.8 O 3 films and their effect on polarization backswitching". In: *Philos. Mag.* 86 (2006), p. 4477.

[47] Jie Wang et al. "Phase-field simulations of ferroelectric/ferroelastic polarization switching". In: *Acta Materialia* 52.3 (2004), pp. 749 –764. ISSN: 1359-6454. DOI: `10.1016/j.actamat.2003.10.011`. URL: `http://www.sciencedirect.com/science/article/pii/S135964540300627X`.

[48] W. G. Wang et al. "Electric-Field assisted switching in magnetic tunnel junctions." In: *Nat. Mater.* 11.1 (2012), pp. 64–68.

[49] Lu You et al. "Polarization switching in quasiplanar BiFeO3 capacitors". In: *Appl. Phys. Lett.* 97.6 (2010), p. 062910. ISSN: 00036951. DOI: `DOI:10.1063/1.3479911`. URL: `http://dx.doi.org/10.1063/1.3479911`.

[50] J. X. Zhang et al. "Effect of substrate-induced strains on the spontaneous polarization of epitaxial BiFeO[sub 3] thin films". In: *J. App. Phys.* 101.11, 114105 (2007), p. 114105. DOI: `10.1063/1.2743733`. URL: `http://link.aip.org/link/?JAP/101/114105/1`.

[51] W Zhang and K Bhattacharya. "A computational model of ferroelectric domains. Part I: model formulation and domain switching". In: *Acta Materialia* 53.1 (2005), pp. 185–198. DOI: `10.1016/j.actamat.2004.09.016`.